Phase Center Stabilization of a Horn Antenna and its Application in a Luneburg Lens Feed Array

by

Brian H. Simakauskas

B.S., University of Massachusetts, 2010

A thesis submitted to the

Faculty of the Graduate School of the

University of Colorado in partial fulfilment

of the requirement for the degree of

Master of Science

Department of Electrical, Computer, and Energy Engineering

2015

This thesis entitled:
Phase Center Stabilization of a Horn Antenna and its Application in a Luneburg Lens Feed Array
written by Brian H. Simakauskas
has been approved for the Department of Electrical, Computer, and Energy Engineering

_____
Dejan S. Filipović

_____
Maxim Ignatenko

Date _____

The final copy of this thesis has been examined by the signatories, and we
find that both the content and the form meet acceptable presentation standards
of scholarly work in the above mentioned discipline.

Simakauskas, Brian H. (M.Sc., Electrical, Computer, and Energy Engineering)

Phase Center Stabilization of a Horn Antenna and its Application in a Luneburg Lens Feed Array

Thesis directed by Professor Dejan S. Filipović

With any reflecting or refracting structure, such as a parabolic reflector or lens antenna, the knowledge of the focal point is critical in the design as it determines the point at which a feeding signal should originate for proper operation. Spherically symmetrical lenses have a distinct advantage over other structure types in that there exists an infinite number of focal points surrounding the lens. Due to this feature, a spherical lens can remain in a fixed position while a beam can be steered to any direction by movement of the feed only. Unlike phased arrays that beam-steer electronically, a spherical lens exhibits no beam deterioration at wide angles. The lens that accomplishes this is in practice called the Luneburg lens which has been studied since the 1940s.

Due to the electromechanical properties of the horn antenna, it is often used to feed the above mentioned configurations. In the focusing of any feed antenna, its phase center is an approximate point in space that should be coincident with a reflector or lens's focal point to minimize phase error over the radiating aperture. Although this is often easily accomplished over a narrow bandwidth, over wide bandwidths some antennas have phase centers that vary significantly, making their focusing a challenge.

This thesis seeks to explain the problem with focusing a Luneburg lens with a canonical horn antenna and offers a modified horn design that remains nearly focused over a frequency band of 18 – 45 GHz. In addition to simulating the feed / lens configurations, the lens and feed horn will be fabricated and mounted for far field measurements to be taken in an anechoic antenna range. A final feed design will be implemented in an array configuration with the Luneburg lens, capable of transmitting and receiving multiple beams without requiring any moving parts or complex electronic beam-forming networks. As a tradeoff, a separate receiver or switching network is required to accommodate each feed antenna. This aspect of the system, however, is outside the scope of research for this thesis.

Acknowledgements

To the US Navy's Office of Naval Research, I am extremely thankful for their support of this research and for my position with the Antenna Research Group. I know that I have taken a lot away from this experience and I hope my work will contribute to the long-term goals of the CIA project.

I owe my advisor, Professor Dejan Filipović, a great deal of thanks for giving me the opportunity to work with the Antenna Research Group. During my tenure here, I not only gained invaluable experience and knowledge related to antennas and EM concepts, but through working with Filip and my peers I am privileged to have participated in an active research environment with such great people.

Thanks to those who served on my thesis committee: Filip, Dr. Maxim Ignatenko, Dr. Neill Kefauver, and Dr. James Mead all who have provided much appreciated and useful feedback. Maxim's guidance was extremely valuable throughout this entire project. I owe Dr. Nathan Jastram many thanks for his help with the antenna range in getting the measurements necessary for this thesis. I am also thankful to Jim, Ivan, and Andy of ProSensing. My experiences while working there are what motivated me to continue my education over three years ago.

I owe my lovely fiancée Luella an enormous gratitude for her constant support throughout my graduate school career. From day one, she has not only tolerated my busy workload but has remained supportive and kept me motivated to see this through to the best of my abilities. I truly could not have asked for anyone better to share this experience with.

Lastly, a thank you to my parents, brother, and sister for their unconditional support over all the years.

Contents

Figures

Tables

Chapter 1

Introduction

1.1 Background

The need for highly directive antennas exists in many applications, most notably in radio astronomy, communications, radar, and remote sensing where, in a perfect world, an antenna's radiation would be confined to the shape of a pencil beam. Reflector antennas are a common means of transmitting and receiving directive radiation patterns, generally operating with some type of feed antenna. Similarly, lenses can also collimate a feed antenna's radiation into a highly directive beam, which for some applications may be more compatible than a reflector-type design. While lenses require edge mounting and the use of dielectrics which may lead to higher losses and undesired reflections, at microwave frequencies lenses can have better wide-angle scanning performance [1]. The application driving the writing of this thesis involves a wideband (18-45 GHz) military decoy system that must be capable of receiving and transmitting a high power directive beam at any angle in a 2π steradian, or a half-space, field of view. Accomplishing this with a reflector is impractical as it would involve extremely fast mechanical steering. In contrast, a spherically symmetrical lens allows for the placement of numerous feeds in its bottom half space for propagation from its upper half-space, resulting in the desired field of view without requiring any mechanical movement or any blockage to the radiating aperture. This type of lens is known as a Luneburg lens.

1.2 Luneburg Lens

Described by Carl Luneburg in 1944 [2], the standard Luneburg Lens (LL) was designed such that a focal point, located on the surface of the spherical lens, is focused to infinity on the opposite side of the lens. Due to the spherical symmetry of the LL, a high-gain antenna can be realized at any angle by changing only the feed position to coincide with the focal point for that given direction. Unlike other focusing structures, e.g. parabolic reflectors or non-spherical lenses, the lens itself can remain stationary while having its beam steered by only its feed antenna.

The LL has a useful application in the area of radar calibration, where an object of known radar cross section (RCS) at a given angle is desired. To create a radar calibration target, a portion (e.g. half) of the spherical lens's surface is fit with a highly conducting material. Every point on the conductor is then a focal point for a plane wave incident on the opposite side of the lens. The lens not only increases the RCS of the conductor, but it also creates a target that is insensitive to alignment angle relative to other types of calibration targets [3].

In communications, the LL can provide large angular coverage with broad bandwidth, low cross polarization, and high gain to increase data capacity. For example, in one implementation, a twelve-feed LL was implemented into a 120° sector cellular base station and was found to increase the data capacity by almost a factor of twelve as compared to the standard antenna configuration [4]. The LL is also of great interest for on-the-move communication platforms that must maintain limited antenna profiles. High speed trains, aircraft, and maritime applications are examples where a steerable highly directive antenna is required for a two-way communication link with a satellite, for example. To limit its profile size, a single hemisphere of the LL can be used in conjunction with a ground plane with the use of image theory [5].

A LL is constructed such that the index of refraction varies as a function of the radius r, where $r = 0$ is at the center of the sphere and $r = a$ is at the outer surface. The index of refraction n is given as [6]

$$n(r) = \frac{1}{f}\sqrt{1 + f^2 - \frac{r^2}{a^2}} \tag{1.1}$$

For a *standard LL* $f = 1$, however this value can be changed to move the focal point either inside or outside the LL which commonly deems it a *modified LL*. Practical applications may desire the focal point to be located at a point distant from the lens surface, in which case f is chosen such that

$$f = \frac{f_p}{a} \tag{1.2}$$

where f_p is the focal point relative to the center of the lens. A two-dimensional depiction of a LL with $f > 1$ is shown in Figure 1.1.

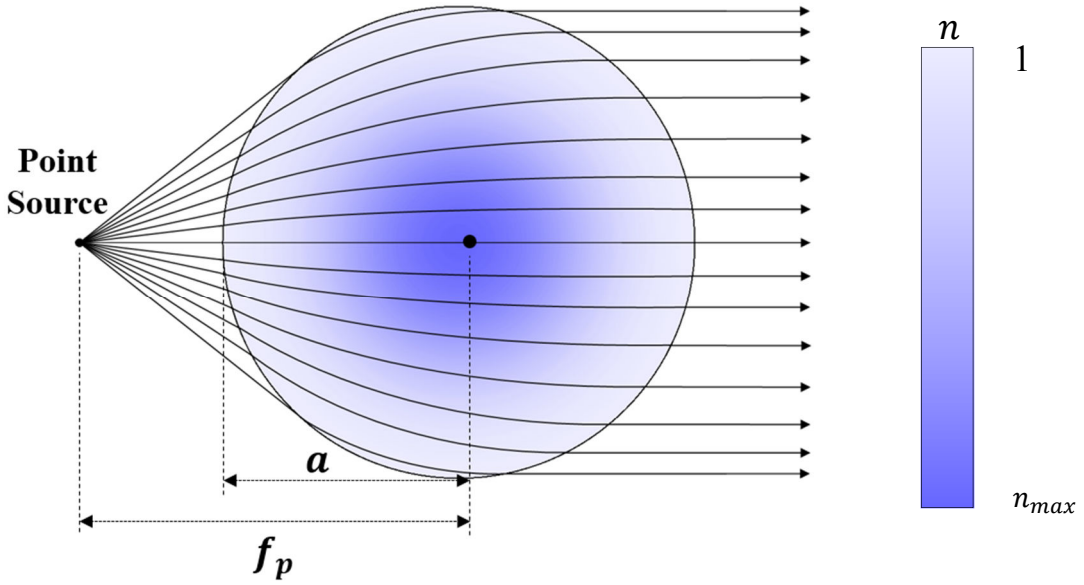

Figure 1.1. Concept of the Luneburg lens using ray tracing. In this example, the focal point is located a distance outside the lens surface ($f > 1$).

An ideal implementation assumes a continuously varying n within the lens, but in practice its profile is typically discretized into m shells to allow for practical fabrication techniques. For example,

LL designs may include $m = 2$, 5, 10, or more shells of different refractive indices n_i, with the innermost section comprising the core of the sphere. The variation of n can be realized by use of different materials for each layer or by dielectric mixing techniques. Dielectric mixing is often accomplished using pockets of air as described in [7] [8]. This method can pose challenges in the precise control of dielectric constants and maintaining lens uniformity and low loss. For ease in fabrication, it is often desired to choose existing low-loss dielectric materials to comprise each shell layer, with careful selection of each shell thickness as demonstrated in [9] with the development of a two-shell LL. A method for implementing a genetic algorithm to determine both the layer thicknesses and the n_i is given in [10], where the values of n_i can be limited to correspond with readily available materials. Because the n_i differ from the values obtained in (1.1), lenses designed in this manner are referred to as *nonuniform LLs*.

Common feed antennas to the LL include open-ended waveguide (OE-WG) [8] [11], horn antennas [5], and patch antennas [12] [13]. For the application discussed herein, the horn antenna is most appropriate due to the wide bandwidth required.

1.3 Horn Antennas

The electromagnetic horn as it applies to microwaves has been studied and experimented extensively with since the late 1930s, driven by developing technology during the World War II era [14]. High performance feed horns have a large presence in satellite communication antennas, radar antennas, and radio-astronomy antennas. The most basic types of feed horns are the E-plane sectoral horn, H-plane sectoral horn, pyramidal horn, square horn, and conical horn. The cross section of a conical horn is circularly symmetric and the other three horns have rectangular or square cross sections. The pyramidal and sectoral horns are characterized by which plane of the horn is *flared*, meaning that the dimension in that plane increases along the axis that runs from the throat of the horn to its aperture. The E/H planes of horn antennas are specified as the planes parallel to the fundamental mode's E/H fields, respectively.

Early thorough analyses of the canonical electromagnetic horn were given in the 1930s by Barrow and Chu [15] and Southworth [16]. The relationship between horn geometry and performance parameters such as the gain then became well understood thanks to the many studies that followed [17] [18] [19]. Since then, numerous features have been developed to improve performance aspects such as transmission of wider bandwidths, reduced cross polarization, and increased beam symmetry, to name a few. Such features directly applicable to the design goals herein will be discussed in chapter 4.

1.4 Application

The LL to be studied has a radius $a = 36$ mm with a focal point ideally located 5 mm from the lens surface. From (1.1) and (1.2), $f = 1.139$ for such a lens and $n = \sqrt{\epsilon_r}$ varies between 1 and 1.33, where ϵ_r is the relative permittivity and n is the index of refraction. A two-layer lens is analyzed in this research, whose inner core consists of a greater n than that of the outer layer [9].

The feeding horn antenna is to operate in a single polarization over the 18-45 GHz range, employing a square aperture to allow for a dual polarized version in a future design iteration. Several feed / lens mounting configurations will be examined in order of increasing complexity, from a single feed mount to a manifold consisting of an array of feeds equally spaced below the lower half space of the lens. With an array of feeds, a directive beam can be transmitted or received in multiple directions (Figure 1.2) without mechanical scanning or complex electrical beam steering.

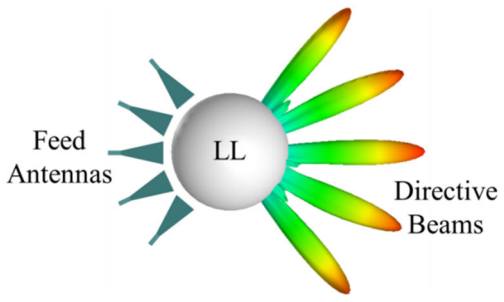

Figure 1.2. A Luneburg lens operating with five feeds in a single plane.

If it were practical to feed the LL with a point source, such as a small dipole antenna, focusing such a feed antenna would be straightforward and its center would be positioned at the focal point of the lens. Positioning a practical horn antenna, however, is more difficult since its radiation pattern is not an ideal spherical wave with a well-defined center point. In the next section, the antenna phase center will be discussed, which is a metric that approximates such a point in which radiation seems to emanate from an antenna.

Although not practically realizable, the Hertzian dipole is a convenient method for simulating a point source using CEM (computational electromagnetics) software. To demonstrate the LL's dependence on its feed's position, an excited 45 GHz Hertzian dipole was swept in distance relative to the LL's surface and simulated using the finite element method (FEM) solver HFSS [20]. The effect on LL directivity is shown in Figure 1.3, where it is clear that its focal point is located 5 mm from its surface.

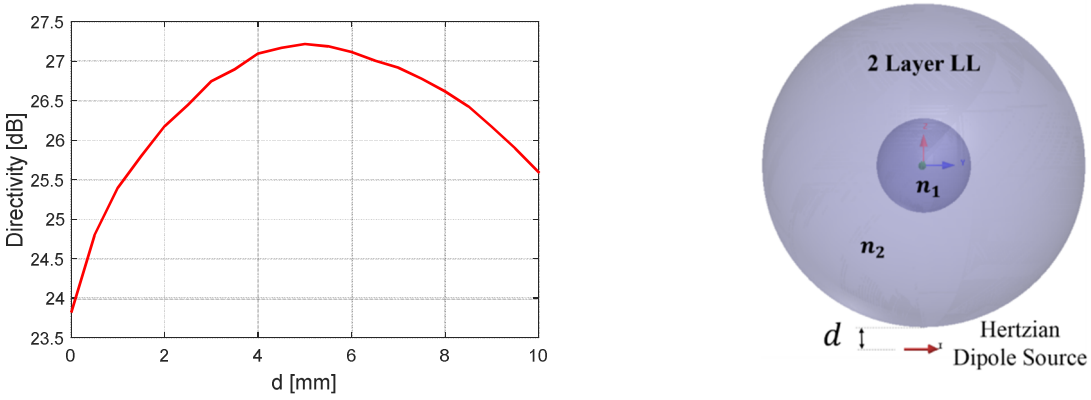

(a) (b)

Figure 1.3. (a) Directivity of a LL vs the positioning of a Hertzian dipole simulated at 45 GHz in HFSS and (b) the model showing the spacing of the Hertzian dipole.

1.5 Phase Center Definition

The phase center (PC) of an antenna is generally not understood as well as the more traditional measurements like directivity, beamwidth, axial ratio, etc. In many cases, knowledge of the PC is simply not of interest in an antenna design and for some antenna types the term is not even applicable. Others,

however, require its full consideration but care must be taken to define the PC appropriately when used since its definition has subjective qualities. Given by IEEE, its definition is [21]:

> Phase center: The location of a point associated with an antenna such that if it is taken as the center of a sphere the radius of which extends into the far field, the phase of a given field component over the surface of the radiation sphere is essentially constant, at least over that portion of the surface where the radiation is significant.

More briefly, the PC defines a point in space at which an antenna's radiation seems to originate and is found at the radial center of a surface consisting of constant phase in the far field. For a point source radiating a spherical wave, the PC is simply at the exact location of the source regardless of frequency. However, a true spherical phase front is not realizable for a physical antenna and can only be approximated over a certain viewing angle, resulting in the qualitative nature of IEEE's definition.

The knowledge or design of an antenna's PC is important in many different applications. Antenna designs often require a feeding antenna to be used in conjunction with a reflector or a lens. For example, the parabolic reflector antenna shown in Figure 1.4 shows transmission of a plane wave due to correct positioning of the feed horn.

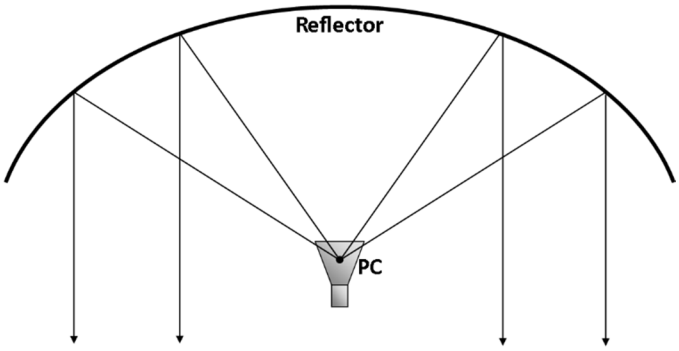

Figure 1.4. Reflector antenna, with the PC of the feeding antenna located at its focal point.

It is well known from a geometrical optics standpoint that maximum antenna directivity is achieved when a spherical wave originates from the focal point of the reflecting structure. Analogously, a plane wave incident on a reflector will converge at its focal point [14]. For this reason, positioning the PC of the feed is an essential component in the design and construction of a reflector antenna since the PC is the point that best approximates the origin of a spherical wave. In narrowband applications, it may be possible to simply tune the feed position mechanically, affixing it at the point that results in maximum directivity of the system. In a wideband system, however, the PC of the feeding antenna tends to vary as a function of frequency [22] and a more careful approach must be considered to avoid defocusing at some frequencies.

Not only does the PC tend to vary with frequency, but it may also vary as a function of angle [23]. The knowledge of PC versus angle is imperative to time-based correlation receivers such as those used in the Global Positioning System (GPS), where a receiver antenna receives signals from at least four different transmitting antennas whose signals are likely arriving from different elevation angles [24]. Using a simple lookup-table, PC corrections can be made for the different signals based on their angle of arrival such that all distance computations are made relative to a single reference point on the antenna. The same process may be used to correct for PC variation of the transmitting antennas as well.

The PC, as it is discussed in this introduction, is most easily applied to linearly polarized antennas radiating a major lobe in one direction. For many antennas, however, defining the PC is not straightforward even with further clarification. For example, mobile phone or laptop antennas do not have an obvious direction or main lobe in which to find the center of curvature with respect to phase. A more general term “radiation center” has been defined using angular momentum of the far field [25]. This research, however, will primarily concern horn antennas and the traditional definition of PC will be suitable with proper clarification.

Other definitions of PC have been developed for specific applications. Kildal, for example, defined the PC as the point in a feed antenna which, when placed at the focal point of a parabolic

reflector, maximizes its aperture efficiency [26]. Although this objective may seem obvious, arbitrary definitions of PC (using the 3 dB or 10 dB beamwidth, e.g.) may not lead to maximum aperture efficiency and thus having a mathematical expression to determine this location is convenient for applications involving single or multi-reflector antenna systems. These types of antennas require constant phase across the reflector's surface to achieve maximum aperture efficiency and minimize cross polarization. This relation can be used to compute PC for practical designs because reflectors only involve one significant degree of freedom in their construction: the reflecting surface. Defining a feed's PC specific for operation with a LL, however, is a much more difficult task as there are up to four degrees of freedom in their construction that will affect performance such as the index of refraction n, inner and outer surface characteristics, and surface reflection losses [1]. For this reason, experimentally determining the PC for a LL is most appropriate for the purposes of this research.

Chapter 2

Extraction of Phase Center Position

2.1 Coordinate System / Geometry

For an antenna in which the definition of phase center (PC) is applicable, the PC can be derived directly from the shape of the radiated far field phase pattern $\psi(\theta)$ which does not depend on the 2π modulus of the phase. Most commonly, the PC is considered within a single plane, e.g. the yz plane in Figure 2.1, where a known far field exists at a distance r from a reference origin.

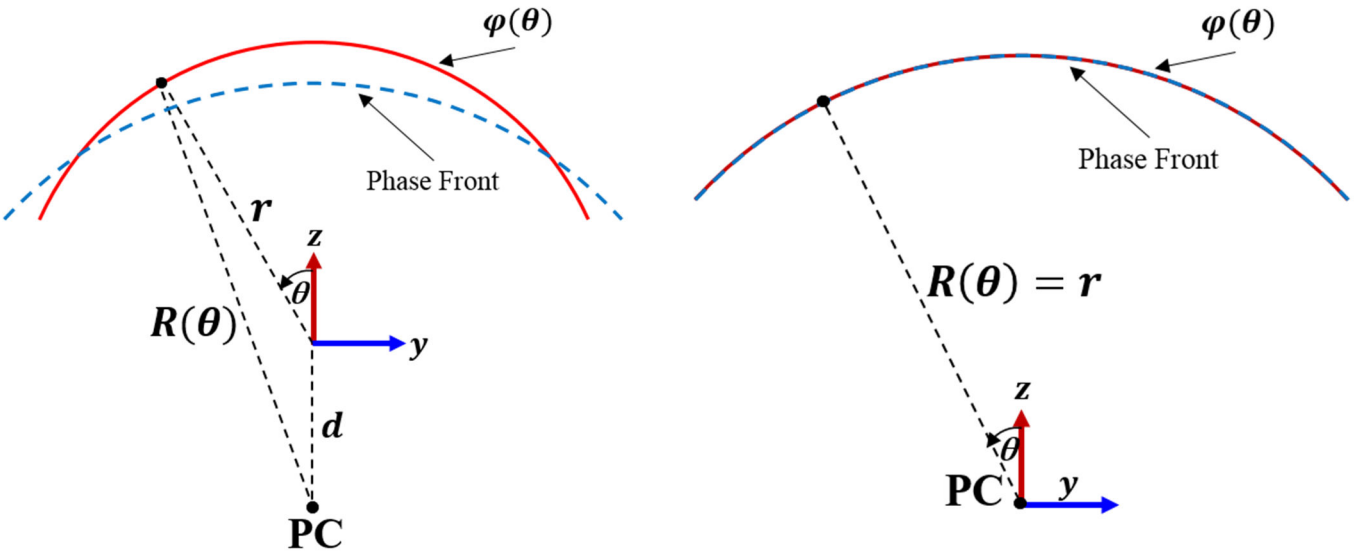

(a) (b)

Figure 2.1. (a) Geometry considered when using far field data (red solid line) at a distance r to determine d, the distance to the PC on the z-axis of the yz plane. The PC is defined as the center of radii of the phase front (dashed blue line). (b) The far field phase coincides with the phase front when the origin is placed at the PC.

Before discussing different methods for computing the PC, it is worthwhile to recognize that if the reference origin is displaced from the PC, then the far field phase function $\varphi(\theta)$ will vary as a function of angle at any far field distance r [Figure 2.1(a)]. In contrast, a sampled $\varphi(\theta)$ that is constant over θ corresponds to the phase front and indicates that the origin coincides with the PC of the radiating source [Figure 2.1(b)].

The phase front in Figure 2.1 is defined as having a nearly constant phase at some arbitrary distance in the far field whose corresponding PC is located at its center of radii. The generalized far field for an antenna can be written as

$$E = |E(\theta,\phi)|\frac{e^{j\varphi(\theta,\phi)}}{r} = |E(\theta,\phi)|\frac{e^{j[\psi(\theta,\phi)-kr]}}{r} \tag{2.1}$$

where $k = 2\pi/\lambda$ is the wavenumber and $\psi(\theta,\phi)$ is the portion of the phase function φ that is dependent on the θ and ϕ spherical coordinates and will contain information leading to the PC location, as the shape of this function will vary depending on the choice of coordinate system origin with respect to the PC.

In general, the PC (and thus d) is a function of ϕ as it will vary depending on the plane in which the far field is measured. Throughout this thesis, the PC will be computed in the two principal planes: the $\phi = 0°$ and $\phi = 90°$ planes which correspond to a horn antenna's H and E-planes, respectively. When using terms such as PC, d, or $\psi(\theta)$, the plane being considered will be explicitly stated. As described in [27], the PC can be defined for an arbitrary plane $\phi = \phi_0$ once it has been measured in the two principle planes, i.e.

$$d(\phi = \phi_0) = \cos^2(\phi_0)\ d(\phi = 0°) + \sin^2(\phi_0)\, d(\phi = 90°). \tag{2.2}$$

Referring to the geometry in Figure 2.1(a), the distance R changes with θ and can be written using the law of cosines:

$$R(\theta) = \sqrt{d^2 + r^2 + 2rdcos(\theta)}. \tag{2.3}$$

This distance is important, as it represents the measured far field relative to the antenna's radiation point of origin rather than to the arbitrary reference origin. For far field amplitude calculations, this distance is often approximated equal to r which is sufficient when the far-field criteria of $r \geq 2D^2/\lambda$ is met, where D is the largest dimension of the antenna aperture. Because the phase is periodic, however, this approximation cannot be used when the reference origin and PC do not coincide ($d \neq 0$). A more accurate approximation for $R(\theta)$ can be derived using Taylor's first order approximation:

$$R(\theta) \cong r + d\,cos(\theta) \tag{2.4}$$

which is valid for $d \ll r$.

2.2 Slope Method

A simple, closed form method for computing the PC was published by Hu in 1961 who was concerned about the positioning of a horn antenna feed for a parabolic reflector [28]. When referenced to the PC, the same field given at some distance r relative to the origin in Figure 2.1 can be expressed as

$$E = |E(\theta,\phi)|\frac{e^{-jkR(\theta)}}{r} = |E(\theta,\phi)|\frac{e^{-jk[r+dcos(\theta)]}}{r} \tag{2.5}$$

which assumes the portion of the field being considered is within the main radiation lobe such that an approximate spherical phase front exists. Equating the phase terms in (2.1) and (2.5), Hu showed that

$$\frac{\psi(\theta)}{\cos(\theta)} = k\,d = \frac{2\pi}{\lambda}d. \tag{2.6}$$

In other words, by plotting the far field phase pattern versus $cos(\theta)$ and measuring the slope of the resulting line, the PC location can be obtained from an arbitrarily placed origin with respect to the wavelength. It should be noted that this method assumes symmetry in two of the planes, such that the PC is known to vary in only one dimension (e.g. the axial dimension of a horn antenna). The inclusion of a

phase time dependency or offset by the phase's kr term will have no effect on the measured slope and thus only knowledge of the phase pattern shape $\psi(\theta)$ is required.

Using HFSS, a 30 GHz half-wavelength dipole, whose PC is known to be at its center due to symmetry in all three planes, was placed at (0,0,1) cm in Cartesian coordinate space as shown in Figure 2.2.

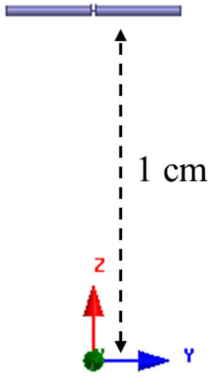

Figure 2.2. Half-wavelength dipole ($f = 30$ GHz) placed 1 cm above the origin in HFSS.

The phase pattern of the $\phi = 0$ plane is plotted in Figure 2.3(a). The same phase profile, when plotted versus $\cos(\theta)$, becomes linear and is shown in Figure 2.3(b).

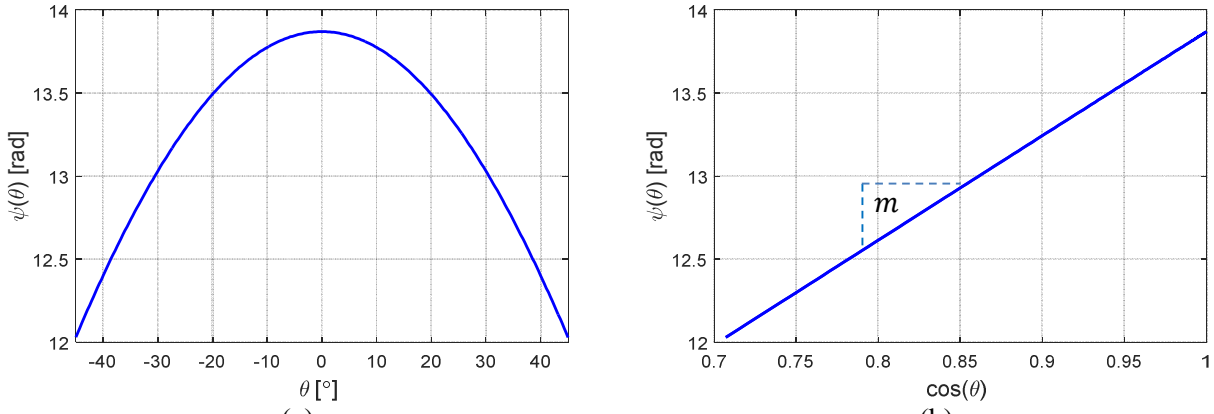

Figure 2.3. (a) Far field phase profile of a 30 GHz $\lambda/2$ dipole placed 1 cm above the origin. (b) The phase pattern plotted versus $\cos(\theta)$.

The slope m in Figure 2.3(b) is found to be $m = 6.28$. With $m = \frac{\psi(\theta)}{\cos(\theta)}$ and k substituted into (2.6), the PC location is found at $d = 0.999$ cm, which is within 10μm ($1 \times 10^{-3}\ \lambda$) of the dipole center.

This method has been dubbed the *two-point method* [29] because Hu calculated the slope using two points, only defining the PC when a straight line could be plotted. With today's abundance of line-fitting algorithms, a linear fit can be applied to simulated or measured data which allows for the computation of the "best fit" PC even when plotting $\psi(\theta)$ vs $\cos(\theta)$ does not result in a perfectly straight line.

2.3 Least Mean Squares Solution

A least mean squares (LMS) solution for PC was described by Rusch and Potter [30] and later simplified specifically for an antenna range setting [31]. Unlike the previous method, this solution decomposes the PC offset distance d into two components (d_Y and d_Z – referring to Figure 2.4). In the $\phi = 90°$ (yz) plane,

$$d(\phi = 90°) = d_Z \cos(\theta) + d_Y \sin(\theta)\ . \tag{2.7}$$

Similarly, if d were being computed in the $\phi = 0°$ (xz) plane,

$$d(\phi = 0°) = d_Z \cos(\theta) + d_X \sin(\theta) \tag{2.8}$$

although for the remainder of this chapter the yz plane will be assumed and all ϕ dependency will continue to be neglected. For any antenna mounted such that $d_Y \neq 0$, a linear slope will be induced into $\psi(\theta)$ which will compromise the accuracy of the slope method, therefore compensation in both directions is desired for a measurement setup which will inevitably contain some offset in the x or y direction due to imperfect alignment of two antennas on the z-axis.

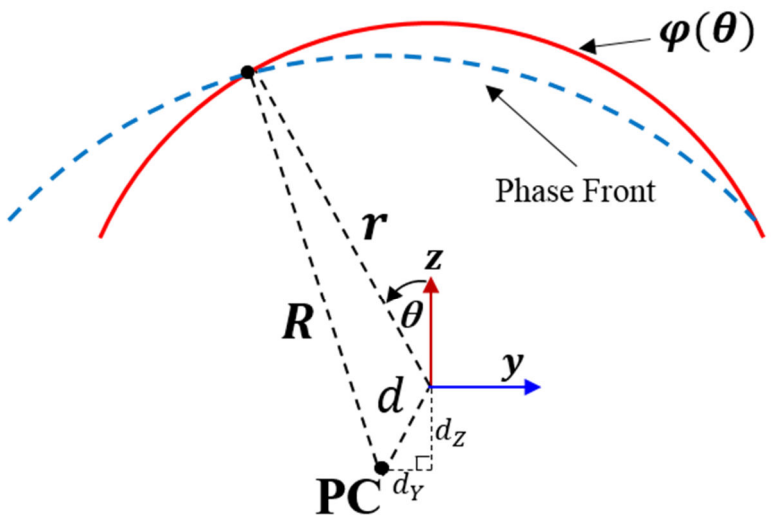

Figure 2.4. Geometry considered when using far field data (red solid line) to determine phase center that is offset in the y and z dimensions. The PC is defined as the center of radii of the phase front (dashed blue line).

Given a set of discretely measured far field phase samples ψ_i within the main lobe, a sum of squares difference (SSD) model can be defined as:

$$SSD = \sum_i [\psi_i - (\psi_0 + k(d_z \cos(\theta_i) + d_Y \sin(\theta_i)))]^2 \tag{2.9}$$

where $\psi_0 = kr$ is the unwrapped phase at $\theta = 0$ and k is the wavenumber. While the phase values ψ_i $(i = 1 \ldots n)$ must be unwrapped, any modulo of 2π is acceptable which is useful when the exact phase is unknown. Equation (2.9) uses the approximation given in (2.4) with d composed into its y and z components. Setting the derivatives of (2.9) with respect to the unknowns (d_Y, d_Z, and ψ_0) to zero, a system can be assembled in matrix form for straightforward solution in an environment such as MATLAB. The resulting system is [31]

$$\begin{bmatrix} -k\sum_i w_i \sin^2\theta_i & k\sum_i w_i \sin(\theta_i)\cos(\theta_i) & -\sum_i w_i \sin(\theta_i) \\ -k\sum_i w_i \sin(\theta_i)\cos(\theta_i) & k\sum_i w_i \cos^2\theta_i & -\sum_i w_i \cos(\theta_i) \\ -k\sum_i w_i \sin(\theta_i) & k\sum_i w_i \cos(\theta_i) & -\sum_i w_i \end{bmatrix} \begin{bmatrix} d_Y \\ d_Z \\ \psi_0 \end{bmatrix} = \begin{bmatrix} -\sum_i w_i \psi_i \sin(\theta_i) \\ -\sum_i w_i \psi_i \cos(\theta_i) \\ -\sum_i w_i \psi_i \end{bmatrix} \tag{2.10}$$

where the w_i terms correspond to an optional weighting function $\boldsymbol{w}$ that can be used to assign "importance" to portions of the phase pattern as it applies to the PC computation. Traditional weighting functions (Gaussian, e.g.) will be maximum at boresight and taper toward the edges of the beam similar to the behavior of the antenna's amplitude pattern. Since the reason for weighting is based on the tapering of radiation intensity at off-boresight angles, it is logical to simply use the antenna's amplitude pattern as the weighting function. This will be referred to as *amplitude weighting* throughout this thesis. For a planar E-field pattern, the amplitude weighting function is defined as

$$w_{a_i} = \frac{\left|E_i^2\right|}{\sum_{i=1}^{n}\left|E_i^2\right|}. \tag{2.11}$$

where the E_i are the far field electric field samples corresponding with the θ_i and ψ_i used in (2.10).

2.4 Exact Solution Using an Iterative Approach

As discussed in the previous two sections, an approximation (2.4) was made in order to allow for the differentiation of field components and for mathematical convenience. In certain situations, however, this approximation can lead to significant phase errors, particularly if the ratio d/r is not small enough. This error is discussed in more detail in Appendix A and a method for solving for PC while avoiding this error is shown below. The far field approximation relative to the PC can be written using the exact solution for $R(\theta)$ which was given in (2.3):

$$E = |E(\theta)|\frac{e^{-jkR(\theta)}}{r} = |E(\theta)|\frac{e^{-jkr\sqrt{1+\frac{(d_Y^2+d_Z^2)}{r^2}+\frac{2(d_Y sin\theta+d_Z cos\theta)}{r}}}}{r} \tag{2.12}$$

where (2.7) was used to decompose d into its y and z components. It should be emphasized that the phase expression in (2.12) is valid within the antenna main lobe and it is assumed that values of θ have been limited to within the first pattern null. For $d \ll r$, (2.12) reduces to (2.5) with the use of a first order Taylor series expansion.

Unlike the previous PC solution methods, the phase term in (2.12) does not allow for a closed-form solution for d_Y and d_Z, suggesting an iterative approach. As described in [30], the PC can be found by minimization of the phase pattern variance computed with respect to an origin adjusted by d_Y and d_Z. The measured phase pattern φ_{meas} (with 2π modulus adjusted to $-kr$ at boresight) whose origin is adjusted by d_Y and d_Z will be referred to as φ_{corr} and is given by

$$\varphi_{corr}(d_Y, d_Z, \theta) = \varphi_{meas}(\theta) - kr\left[1 - \sqrt{1 + \frac{(d_Y^2 + d_Z^2)}{r^2} + \frac{2(d_Y sin\theta + d_Z cos\theta)}{r}}\right]. \quad (2.13)$$

As opposed to the previous methods, the knowledge of r is required in (2.13) and must be used to ensure the 2π modulus of $\varphi_{meas}(\theta)$ is accurate. In an antenna range, r corresponds to the distance between the probe antenna's PC and center of rotation (Appendix A). For simulations which typically project the far field to $r = \infty$, simply using a large value of r will suffice.

A quasi-Newton method was implemented in MATLAB to find the minimum variance of (2.13) for a given phase pattern measurement, i.e. to find d_Y and d_Z that results in the "flattest" phase pattern. To minimize the variation of φ_{corr} over all θ of interest, a cost function $g(\boldsymbol{d})$ is defined as

$$g(\boldsymbol{d}) = \frac{1}{n}\sum_{i=1}^{n} w_i |\varphi_{corr}(\boldsymbol{d}, \theta_i) - \langle \varphi_{corr}(\boldsymbol{d}) \rangle|^2 \quad (2.14)$$

where $\boldsymbol{d} = \begin{bmatrix} d_Y \\ d_Z \end{bmatrix}$. Equation (2.14) is similar to the variance σ^2 of the phase pattern but includes an optional weighting vector $\boldsymbol{w}$ as described in the last section. The brackets in the term $\langle \varphi_{corr}(\boldsymbol{d}) \rangle$ indicate

the mean value of φ_{corr} over all θ_i being considered. If the weighting function is used, then a weighted arithmetic mean should also be used, i.e.

$$\langle \varphi_{corr}(\boldsymbol{d}) \rangle = \frac{\sum_{i=1}^{n} w_i \varphi_{corr}(\boldsymbol{d}, \theta_i)}{\sum_{i=1}^{n} w_i}. \tag{2.15}$$

The cost function $g(\boldsymbol{d})$ can be minimized by iteratively solving

$$\boldsymbol{d_{n+1}} = \boldsymbol{d_n} - [\boldsymbol{H}(\boldsymbol{d_n})]^{-1} \boldsymbol{\nabla g}(\boldsymbol{d_n}) \tag{2.16}$$

until $\boldsymbol{d}$ converges [32]. $\boldsymbol{H}$ is the Hessian matrix and is equal to

$$\boldsymbol{H} = \begin{bmatrix} \frac{\partial^2 g}{\partial d_Y^2} & \frac{\partial^2 g}{\partial_Y \partial_Z} \\ \frac{\partial^2 g}{\partial_Y \partial_Z} & \frac{\partial^2 g}{\partial d_Z^2} \end{bmatrix} \tag{2.17}$$

and the gradient vector $\boldsymbol{\nabla g}(\boldsymbol{d_n})$ is equal to

$$\boldsymbol{\nabla g}(\boldsymbol{d_n}) = \begin{bmatrix} \frac{\partial g}{\partial d_Y} \\ \frac{\partial g}{\partial d_Z} \end{bmatrix}. \tag{2.18}$$

When applied to simulated data, a $g(\boldsymbol{d})$ of nearly zero is easily obtainable upon finding the PC. Due to uncertainties rising from a finite signal to noise ratio, range measurements will tend to converge with a greater value of $g(\boldsymbol{d})$.

2.5 Summary

For most simulations and measurements conducted in this research, the LMS method will suffice to provide an accurate PC location. In cases where an antenna under test (AUT) incurs a large rotational scanning error as discussed in Appendix A, the iterative approach should be used and careful measurements should be taken between the AUT, probe antenna, and scanning center of rotation. In all cases, amplitude weighting will be applied to the field of view being considered in the PC computation.

Because any nonzero d_X or d_Y will be attributed to mounting misalignments since the antennas in this research are symmetric around the z-axis, reported values of d in future chapters are simply equal to d_Z as discussed in this chapter.

Chapter 3

Phase Center of Horn Antennas

3.1 Introduction

The phase center of a canonical horn antenna is dependent on horn dimensions such as flare angle ψ_e and ψ_h, aperture size $a_1 \times b_1$, and length L (Figure 3.1). Generally, for a smaller flare angle the PC tends toward the aperture of the horn. In contrast, the PC in horns having wide flare angles is located more toward the throat, or apex, of the horn [14]. The reason for this behavior is inherent to the geometry of the horn and is illustrated in Figure 3.1(b), where the difference between ρ_e and ρ_1 leads to a phase error δ_e in the E-plane of the aperture. As the flare angle ψ_e tends to zero, $\rho_e = \rho_1$ and $\delta_e = 0$ as in an open-ended waveguide [33]. The same is true in the H-plane, whose phase error δ_h is shown in Figure 3.1(c). The tangential fields in the pyramidal horn's aperture plane are given by the approximation [14]

$$E_{y'}(x', y') = E_0 \cos\left(\frac{\pi}{a_1} x'\right) e^{-j\left[k\left(\frac{x'^2}{\rho_2} + \frac{y'^2}{\rho_1}\right)/2\right]}, \tag{3.1}$$

where the prime symbol indicates a coordinate system centered in the aperture plane of the horn. The phase in a horn aperture has a quadratic distribution in both the x' and y' directions which describes mathematically δ_e and δ_h shown in Figure 3.1. Note that as frequency increases (λ decreases), $k = 2\pi/\lambda$ becomes larger and enhances the phase term in (3.1). One may expect similar PC behavior in both E and H planes due to the similar quadratic phase dependence of x and y in (3.1), however because the aperture amplitude tapers in the x direction (H-plane), the extent to which δ_h influences the H-plane PC is less than that of δ_e in the uniformly illuminated E-plane.

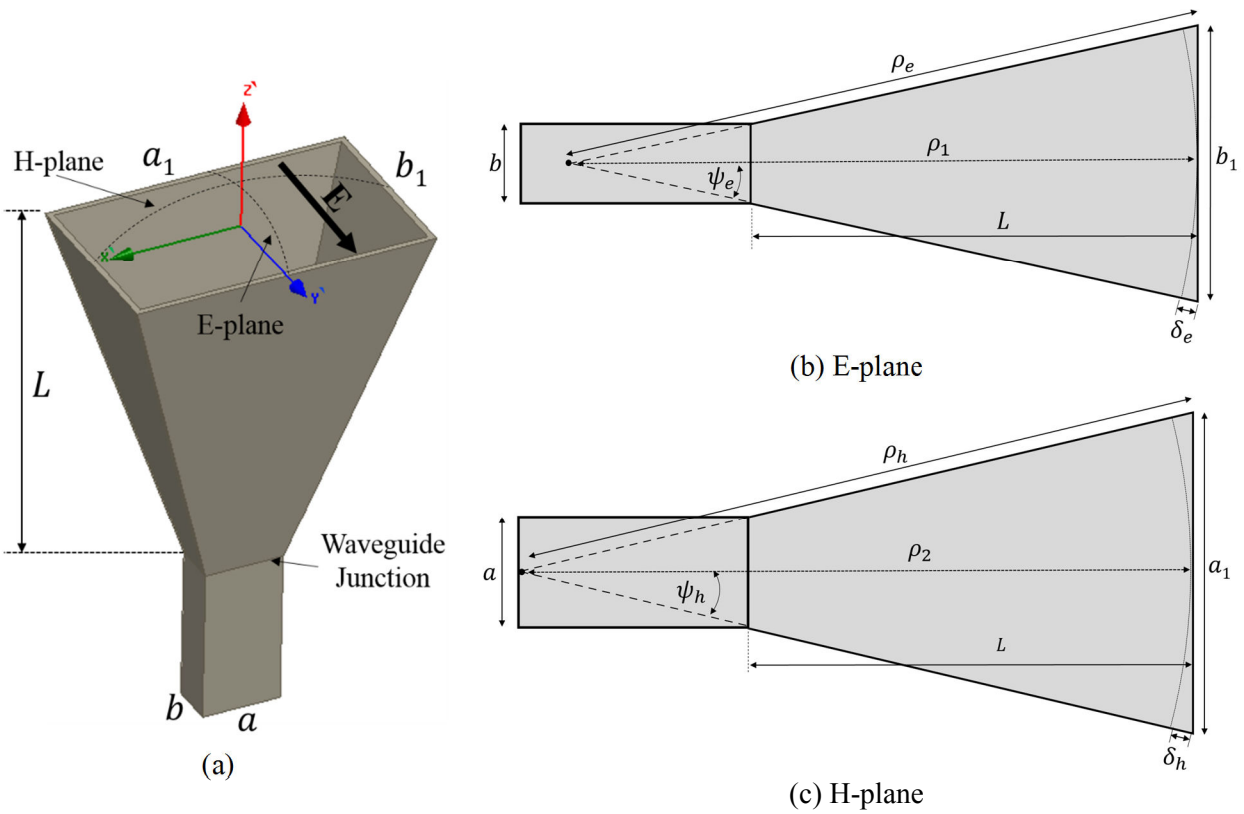

Figure 3.1. Horn antenna design parameters (a) isometric view (b) E-plane dimensions and (c) H-plane dimensions.

3.2 Analytical Derivations

Muehldorf analytically derived expressions for the PC location in square, diagonal, and rectangular horns as functions of their electrical dimensions [27]. These expressions were developed using equivalent aperture electric and magnetic currents while considering the spherical phase error δ_e and δ_h in the horn aperture. The analysis assumes a single TE_{10} waveguide mode feeding the antenna and is valid only for angles near boresight due to approximations used within the derivations. After deriving the far field patterns, Muehldorf determined the PC as the center of radii of a far field equiphase surface near boresight. It is shown that the PC can be found as the second derivative of the phase front at boresight ($\theta = 0$). While the boresight approximation and single propagating mode limit the usefulness

of the analytical expressions, they are nonetheless a valuable tool for validating empirical models used for determining the PC in standard horn antennas.

As an extension to Muehldorf's work, Teichman derived the PC in horn antennas using edge diffraction theory and included measurements for comparison [34]. Edge diffraction theory uses a superposition of the main geometrical optics field and two diffracted signals (on the two E-plane edges) which are taken as the sources of radiation from which to derive the far fields. To characterize both horn size and the frequency's influence on PC, Teichman successively shaved down the length of an X-band horn and measured over 7.5-10 GHz. Close agreement was observed for large horns ($k\rho_e$ > 50) but as the horn was trimmed to shorter lengths the measured PC location began to vary widely with respect to the theoretical results. Teichman theorized that in the case of shorter horns, higher-order modes excited within the horn may not have had sufficient length to attenuate as they would have in the longer horns.

3.3 Example Horn Simulations

A set of horns were designed in HFSS with the parameters shown in Table 3.1. The set consists of a rectangular horn, square horn, and sectoral horns of both E and H-planes. Dimensions of the rectangular horn (Horn 1) are consistent with Ka-band standard gain horns that are commercially available and the three other geometries are extensions of Horn 1. All dimensions in Table 3.1 correspond with those labeled in Figure 3.1 and are fed with WR28 rectangular waveguide. The dimensions of Table 3.1 were used to obtain the PC over frequencies of 26 – 40 GHz using Muehldorf's analytical models. As seen in Figure 3.2, the coordinate system origin is located in the center of the aperture which is consistent with Muehldorf's point of reference.

Table 3.1. Design Parameters for Example Horn Antennas.

Dimension	**Horn 1** Rectangular	**Horn 2** Square	**Horn 3** E-Sectoral	**Horn 4** H-Sectoral
a_1 [mm]	19.3	19.3	7.1	19.3
b_1 [mm]	14.0	19.3	19.3	3.6
ρ_1 [mm]	47.7	43.6	47.7	N/A
ρ_2 [mm]	56.3	56.3	N/A	56.3
ρ_e [mm]	48.2	44.6	48.2	N/A
ρ_h [mm]	57.1	57.1	N/A	57.1
ψ_e [°]	16.7	25.0	16.7	N/A
ψ_h [°]	14.1	19.5	N/A	14.1
L [mm]		35.6		
a [mm]		7.1		
b [mm]		3.6		

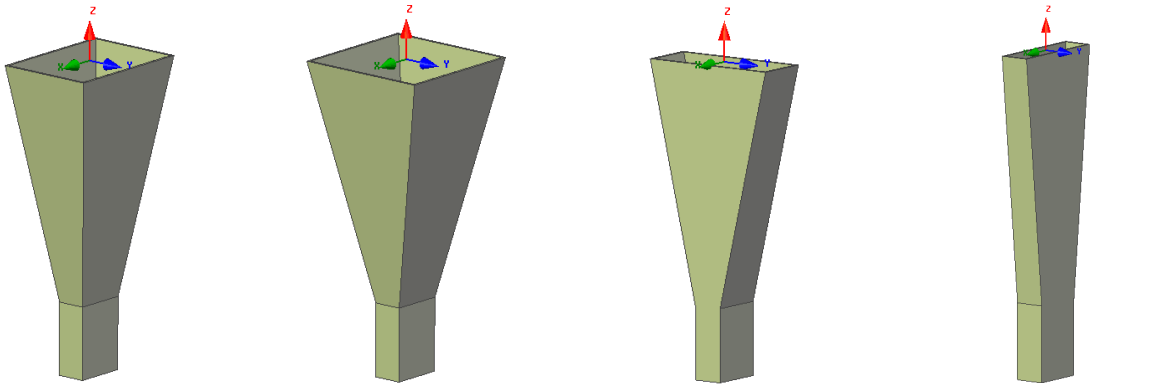

(a) Horn 1 – Rectangular (b) Horn 2 – Square (c) Horn 3 – E Sectoral (d) Horn 4 – H Sectoral

Figure 3.2. Horn example antennas 1-4 modeled in HFSS, with the coordinate system origin located in the center of the aperture.

Values of PC were computed using the LMS method over various spans in the far field and are plotted in Figure 3.3. Using the coordinate system defined in Figure 2.1, $d > 0$ corresponds to a PC inside the horn and $d < 0$ outside the horn. The PC's dependence on its definition is apparent in the plots of Figure 3.3, where computing PC over a constant 5 degree span yields results closest to Mueldorf's analytical expressions. This is expected since their derivations include a $\sin\theta \cong \theta$ approximation which is valid for only small values of θ. In general, it can be seen that the PC tends into the horn (d increases) as the span is increased. Although the E and H-plane PCs are sometimes averaged to obtain a single value [35], they will remain separate throughout this thesis.

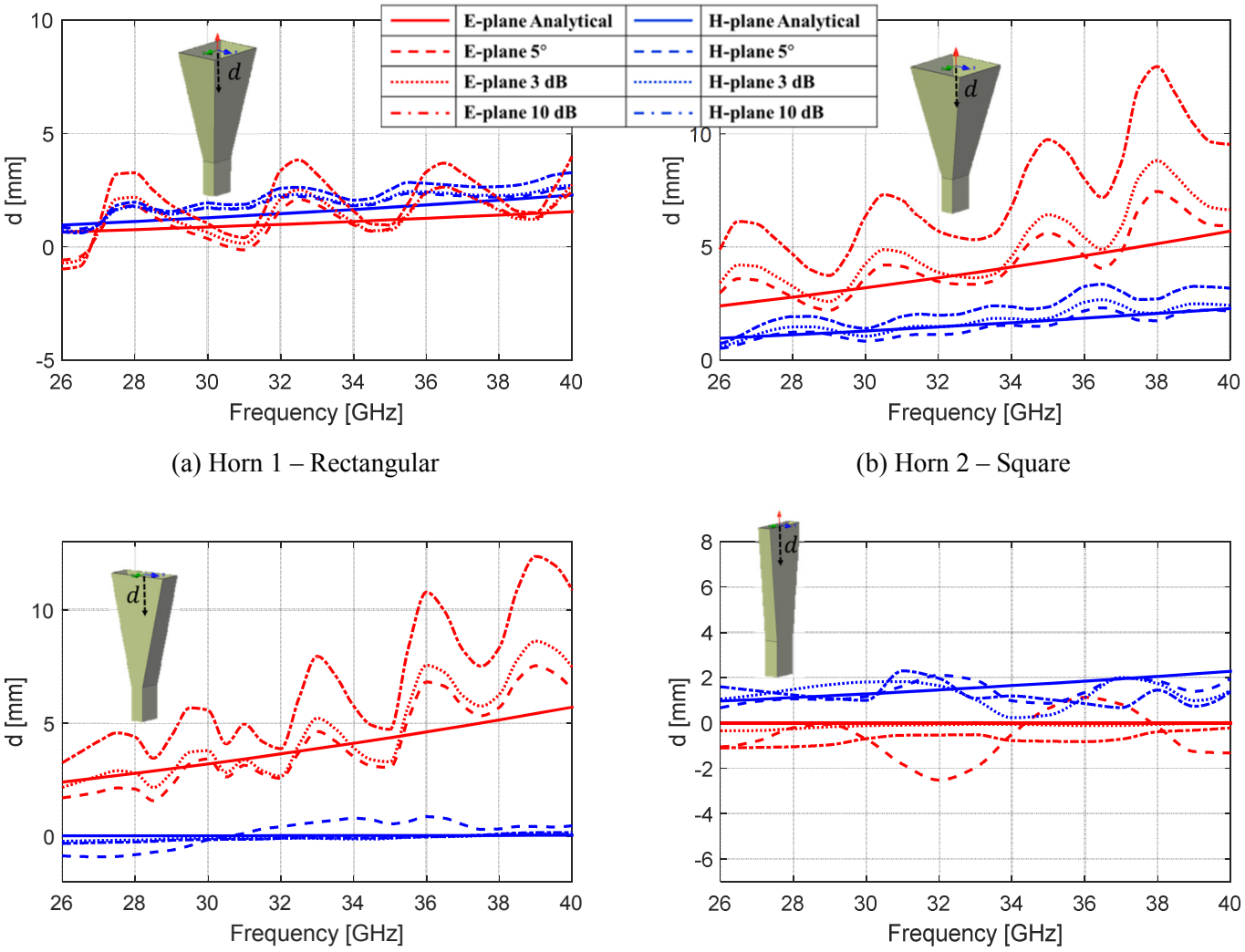

(a) Horn 1 – Rectangular

(b) Horn 2 – Square

(c) Horn 3 – E Sectoral

(d) Horn 4 – H Sectoral

Figure 3.3. E and H-plane PC location versus frequency of the modeled horn antennas given in Table 3.1 using beamwidths of 3 dB, 10 dB, and constant 5° compared to the analytical model. A value of $d > 0$ corresponds to a PC location located inside the horn relative to the aperture plane.

The aperture fields for horn 1 were acquired in method of moments (MoM) software FEKO [36] and are plotted in Figure 3.4. Though they are not an exact representation of (3.1), the general features in both amplitude and phase are present. That is, the amplitude tapers in the x direction (H-plane) and the phase changes quadratically in both x and y directions. With the scale of the phase remaining constant for all frequencies, the phase error δ_e and δ_h can be easily visualized in the right column of Figure 3.4,

which becomes less uniform as the frequency increases and corresponds with a PC located further into the horn, as was seen in Figure 3.3(a).

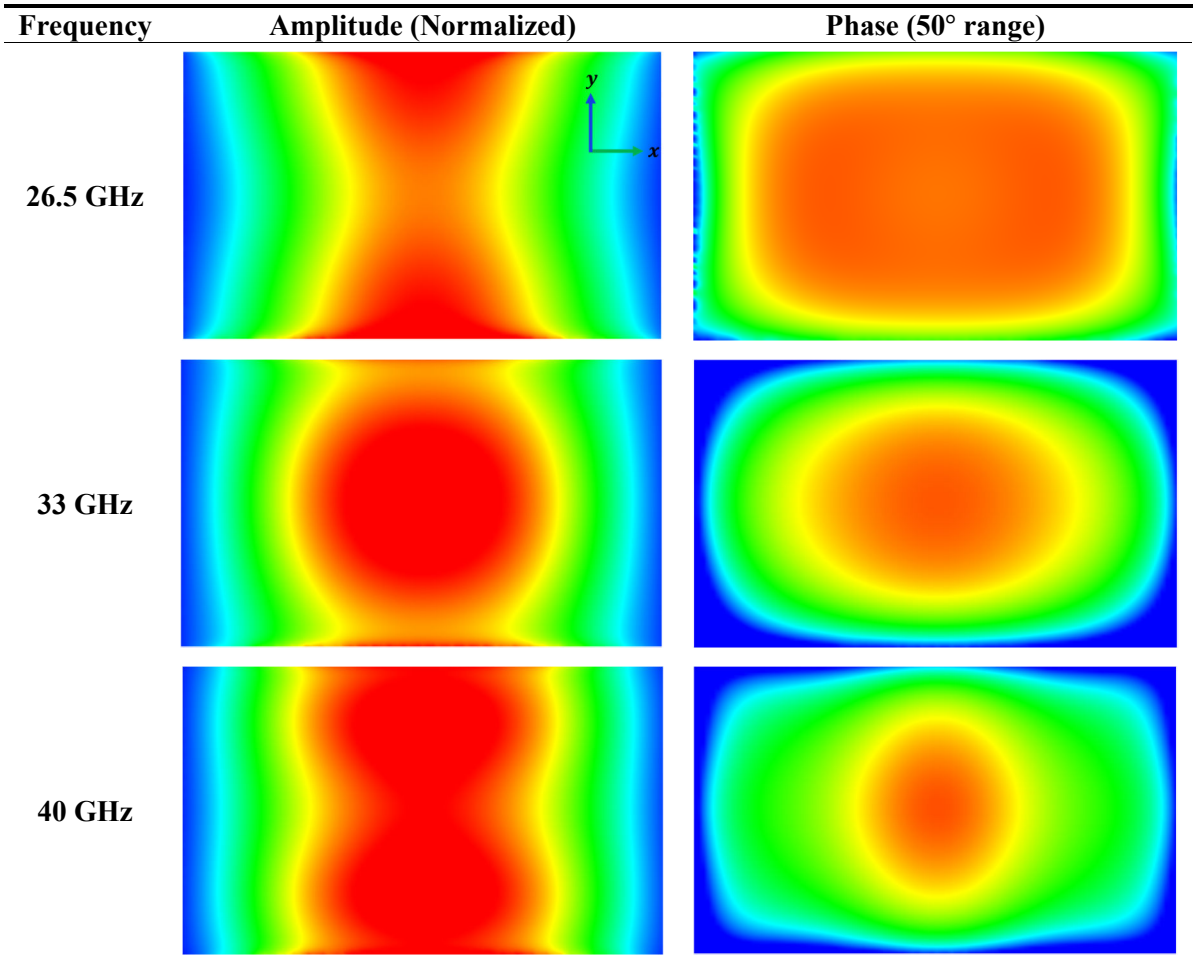

Figure 3.4. Horn 2 aperture fields, normalized amplitude (left column) and phase (50° range, right column).

The examples in this section, particularly when the horn's E-plane is flared significantly (horns 2 and 3), demonstrate the extent to which the PC can be expected to vary over a wide frequency band. Fortunately, there are horn design features that can be implemented to minimize the PC's movement with respect to frequency.

Chapter 4

Phase Stabilized Horn Design and Fabrication

4.1 Introduction

For operation with a LL having a fixed focal point, the main design goal of the feeding antenna involves stabilizing its PC, or minimizing the PC's variation in space, over frequency. This metric will be referred to as phase center variation with respect to frequency PCV(f) and should not be confused with PCV(θ, ϕ) as it refers to the PC variation over angle, typically a design concern for antennas used in ranging applications [23] [29]. It is well known that the PC of an open-ended waveguide is near the aperture center and is not sensitive to frequency since there is a uniform phase distribution across the aperture [37]. While open-ended waveguide has been used to feed a LL [11], a custom horn antenna is required here due to the wide operating bandwidth. In addition, designing a custom antenna allows for a lower VSWR and improved E/H plane symmetry.

The horn antenna is to be fed with a custom feed waveguide WRD-1845 [38], consisting of a dual-ridge cross-section (Figure 4.1) for propagation over the 18-45 GHz band. These ridges must extend into the horn's flared section to maintain a good impedance match. Several methods for stabilizing the PC will be discussed in the next section while taking into account the limitations and requirements specific to the constraints of the application.

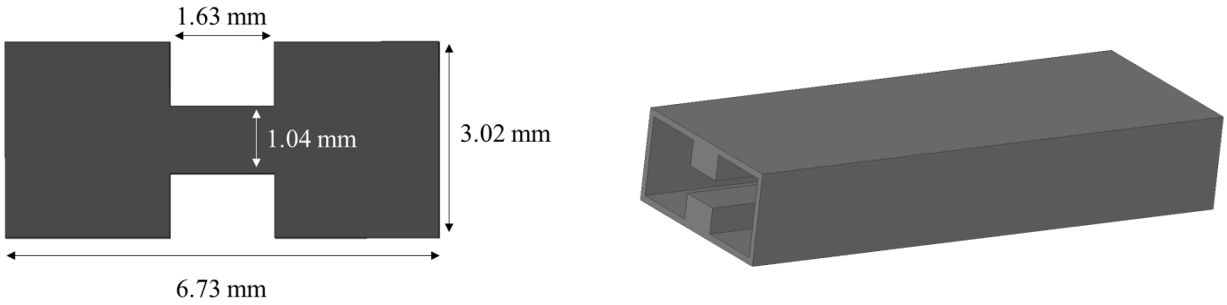

(a) (b)

Figure 4.1. (a) WRD-1845 cross section dimensions and (b) 3D model of the double-ridged waveguide.

4.2 Methods for Phase Center Stabilization

Chapter 3 discussed several tendencies of PC behavior that can be expected in standard horn antennas. Any movement in PC as a function of frequency is generally undesired for a feed antenna since it will cause defocusing at some portions of the band. Fortunately, there are several design features that can be exploited for their PC stabilization with respect to frequency.

4.2.1 Flare Angle Design

It was mentioned in section 3.1 that as a horn's flare angle ψ is decreased the PC will tend toward the aperture. Careful design of the flare angle in both E and H-plane can be a straightforward approach for achieving low PCV while maintaining a nearly identical E/H-plane PC. In Figure 3.3, the square horn's (horn 2) E-plane PC is much further into the horn than the H plane PC. The rectangular horn (horn 1), however, has an E-plane PC much closer to the aperture as a result of the smaller dimension b_1 which also reduces the flare angle ψ_e. Because the feed horn for this study requires a horn that can be modified to support dual-polarization, a square aperture will be used despite the advantages of using rectangular in terms of PCV and E/H-plane PC coincidence when transmitting / receiving a single polarization.

4.2.2 Corrugations

Corrugations in the horn sidewall are a useful feature for achieving E/H-plane beam symmetry and low cross-polarization, and for this reason they are extremely common feed antennas for reflector

antennas used in radar and communications [39]. Each corrugation can be viewed as an individual transmission line. If designed correctly, the transmission lines can be designed such that there is a negative reactance (capacitance) seen by a surface wave on the sidewall of the horn. Surfaces satisfying this requirement are often referred to as *soft surfaces* and are described in detail in [40].

A correct corrugation design will force the E-field to zero on the E-plane walls of the horn. This behavior is similar to that expected on the horn H-plane edges where the E-field component is tangential to the wall. For perfect conductors, it is well known that the tangential component of the E-field will be zero. The tapering of the E-field amplitude in both x and y, as a result, reduces the far field sidelobes and causes the E/H beams to be more symmetric [14]. In a similar manner, the E-plane PC will behave more like the H-plane PC which tends to remain closer to the aperture over frequency.

Referring to the geometry in Figure 4.2(a), maintaining a capacitive surface reactance requires (4.1) – (4.3) to be satisfied across the frequency band [14]:

$$\frac{\lambda}{4} < d_c < \frac{\lambda}{2} \tag{4.1}$$

$$w \leq \frac{\lambda}{10} \tag{4.2}$$

$$t \leq \frac{w}{10} \tag{4.3}$$

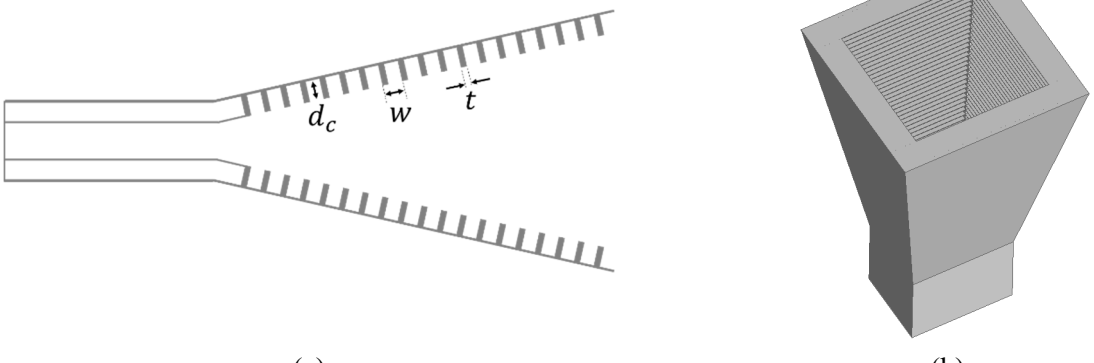

(a) (b)

Figure 4.2. (a) Corrugation design parameters and (b) HFSS corrugated square horn model.

Corrugations were implemented into all four walls of the square example antenna (horn 2) discussed in section 3.3 [Figure 4.2(b)] and the aperture fields were obtained in HFSS. The tapering of the E-field in the *y* direction of the aperture plane can clearly be seen in the right column of Figure 4.3.

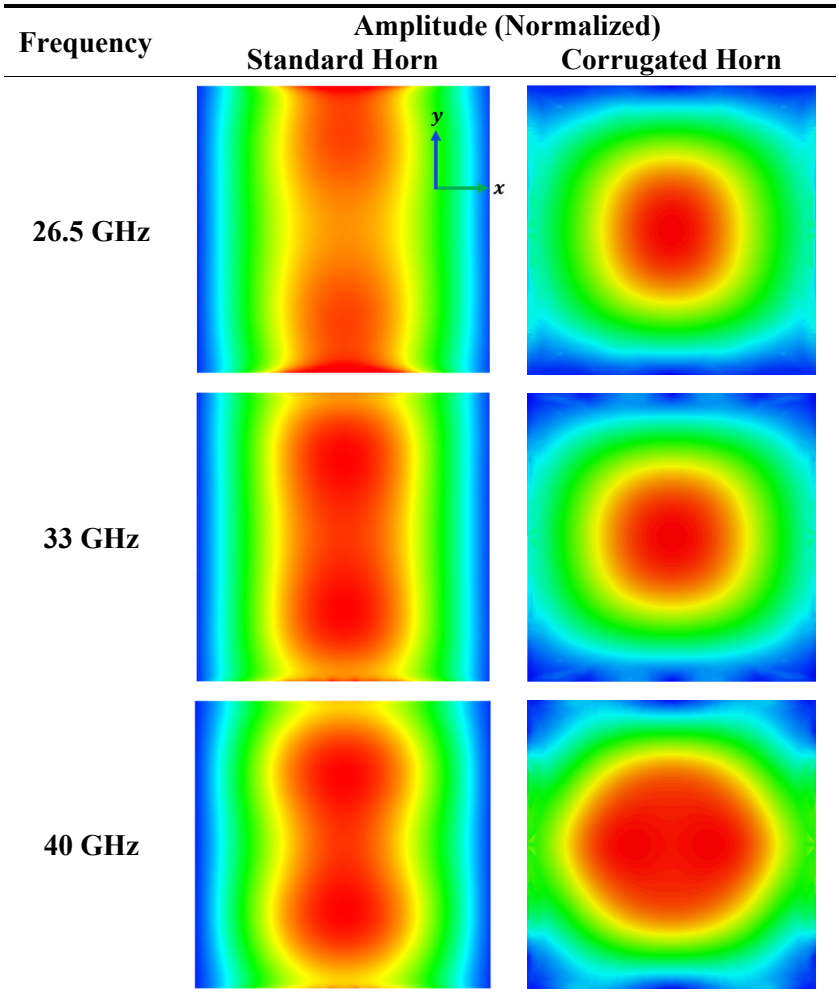

Figure 4.3. Aperture E-field intensity of the standard square horn (horn 2) vs. the corrugated horn.

The corrugated horn's impact on PC is evident in Figure 4.4, where the E-plane PCV is reduced from 6.2 mm to 1.9 mm. The E and H-plane PCs are also closer to each other than they are in the standard square horn.

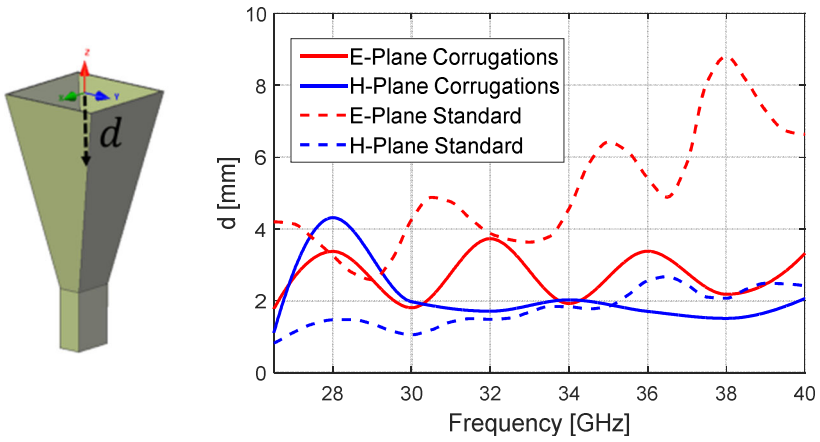

Figure 4.4. E / H plane PC location d vs. frequency of the corrugated horn (solid lines), compared to the identical horn without corrugations (dashed lines).

Although corrugations have some clear advantages, there are also exist some impracticalities that may limit their use. In this application, for example, (4.1) cannot be satisfied over the required bandwidth of 18 – 45 GHz. In addition, the increase in sidewall depth of at least d_c makes this design a challenge where space is a premium.

4.2.3 Flare Profile Design

The most basic explanation for PCV behavior of a horn antenna is due to the differing lengths of the horn axis and sidewall, ρ_1 and ρ_e [Figure 3.1(b)]. The addition of a flaring profile to the horn sidewall, however, invalidates this simple relation since higher order modes will be excited and the fields within the horn become much more complex than the single moded cylindrical wave that is often assumed when computing the aperture fields analytically [34].

Specific flaring profiles have been used for various performance features in the past. For example, exponential ridge flares have been used as a means of matching a horn's 50Ω coax transition to 377Ω (free space) over wide bandwidths [41]. A number of successive linear flares of varying flare angle may be used to excite specific modes leading to E/H-plane symmetry in the far field pattern [42]. The

$\sin^2$ profile was used on a corrugated sidewall and was found to match well to the feeding coax/waveguide transition while reducing phase error across the aperture [43]. Figure 4.5 shows some different flaring profiles that were considered in this antenna design.

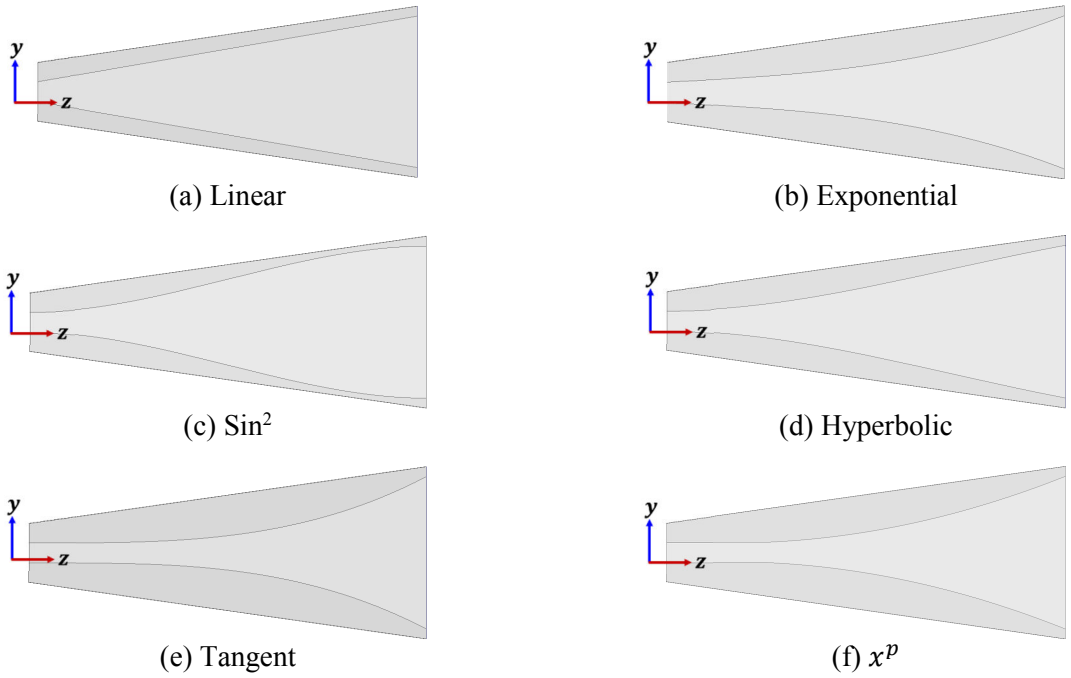

Figure 4.5. Profile types that were considered for the feed horn design.

Because the dual waveguide ridges (Figure 4.1) must be extended into the horn aperture, the profiles shown in Figure 4.5 were applied to the horn ridges themselves and it was found that both the radiation characteristics and the VSWR of the horn are very sensitive to both the profile type and the design parameters associated with it. Like in [43], the $\sin^2$ profile was found to have a beneficial effect on equalizing the aperture phase distribution and thus helps to stabilize the PC over frequency. This profile, shown in Figure 4.5(c), is given by the expression

$$y(z) = y_0 + (y_{ap} - y_0)\left[(1 - A)\frac{z}{L_T} + A\sin^2\left(\frac{\pi z}{2L_T}\right)\right] \tag{4.4}$$

where y_0 and y_{ap} are the ridge y dimensions at the beginning of the taper and at the aperture, respectively, A is a coefficient between [0-1] controlling the amount of linear taper added to the profile,

L_T is the length of the taper in the z direction, and y and z are relative to the origin shown in Figure 4.5(c). A comprehensive list of profile expressions can be found in [44].

4.3 Horn Design 1

As mentioned in the previous paragraph, careful design of the horn's ridge profile is a means of controlling the PCV. With the implementation of a $\sin^2$ profile, the design parameters a_1 and L were set to 9.8 mm and 20.3 mm, respectively, after some analysis of how these two parameters affected the VSWR relative to a matched waveport in HFSS. This left three main geometry parameters to be designed, all related to the shape of the ridge profile.

4.3.1 Parametric Study Setup

Table 4.1 lists the three design parameters to be studied, corresponding to a_p, b_p, and c_p in Figure 4.6.

Table 4.1. Parametric Sweep Dimensions.

Parameter	Description	Sweep range
a_p	Aperture ridge width	0.2 – 1.3 mm
b_p	Taper start height – above waveguide junction	0 – 10 mm
c_p	Linear taper coefficient (A)	0 – 1

The HFSS horn model is shown in Figure 4.7, which has an absorbing boundary condition (ABC) enforced on the half-sphere surrounding the horn aperture and is located no closer than $\lambda/2$ at the lowest frequency to any part of the antenna. Fields are absorbed by this boundary, which are then projected into the far field by HFSS [45]. The horn was modeled with walls of both infinite smoothness and thinness. An additional analysis of the effects of surface roughness can be found in section 5.5.2.

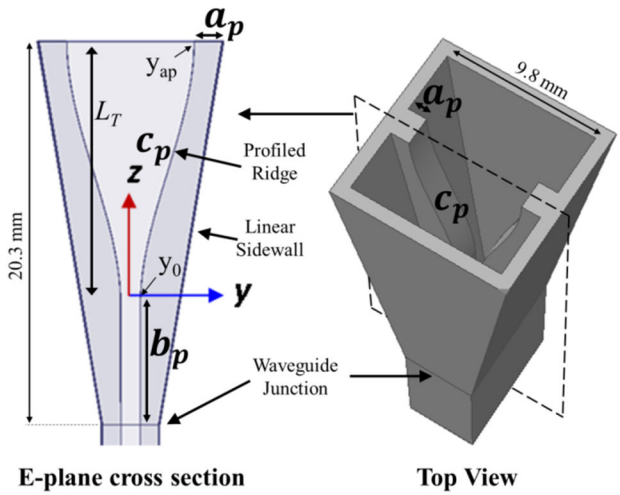

Figure 4.6. Schematic of the horn antenna, with parametric study parameters labeled $a_p - c_p$.

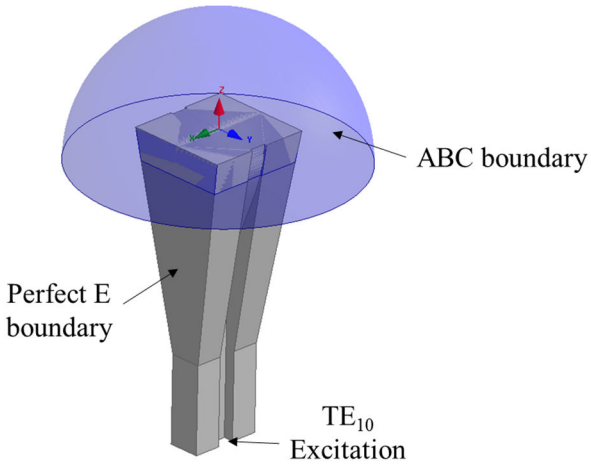

Figure 4.7. Horn design 1 as modeled in HFSS for the parametric sweep.

Although the implementation of a true optimization could save computational resources if implemented correctly, it was not attempted for this design due to the difficulty in defining a cost function involving computed PCs at various frequencies. Because HFSS does not intrinsically return the PC of an antenna, an external environment such as MATLAB would be required to interact with HFSS for full execution of the optimization. Furthermore, an optimizer would have a high probability of getting trapped in the cost

function's local minima. When computationally viable, the parametric sweep allows all data to be taken then analyzed from multiple angles to determine a suitable design while capturing all local minima of the cost function. In this exercise, seven different frequencies were sampled for each geometry and an estimated PCV was determined as the maximum deviation over the seven samples. As an example, Figure 4.8 shows the PCV and VSWR for a geometry that was part of the parametric sweep with the seven sampled frequency points labeled. Although the actual PCV can be seen to be approximately 3.3 mm, the PCV as seen at the 7 simulation points, or PCV_{est}, is 3 mm.

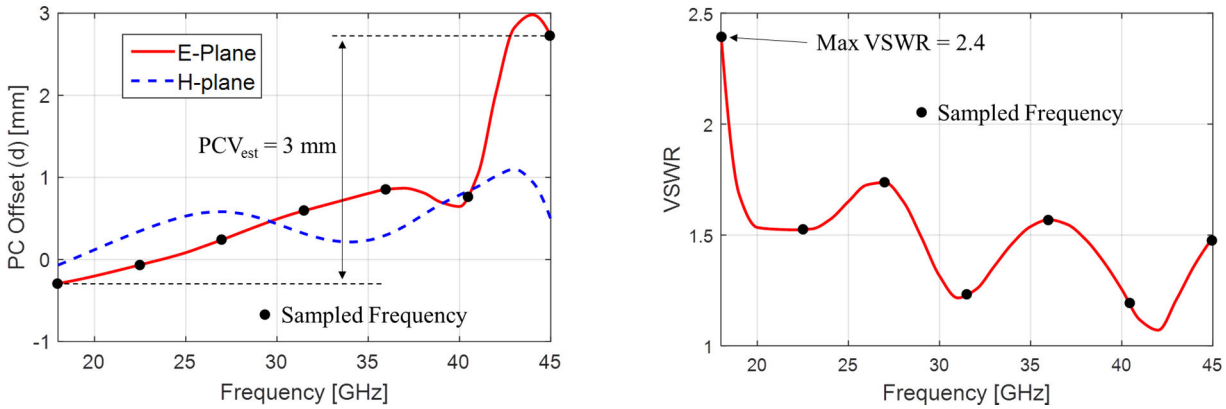

Figure 4.8. (a) PCV (b) and VSWR profiles for a single geometry of the parametric sweep, with the sampled frequency points labeled.

It is important to note that due to limited frequency sampling, the estimated PCV can only appear to be lower than the actual PCV and thus no "good" designs will be neglected because of coarse frequency sampling. While this reduces simulation time, the tradeoff is the time required to manually simulate the highest performing geometries to determine which is truly the best performing when finer frequency points are sampled.

4.3.2 Parametric Study Results

After simulating the 780 geometries in HFSS, the geometry with the lowest E-plane PCV was chosen given that multiple other required specifications were met, as summarized in Table 4.2.

Table 4.2. Horn antenna design specifications.

Specification	Value
VSWR	< 2
X-pol Isolation	> 30 dB
Peak sidelobe level	> 20 dB
Front to back ratio	> 10 dB

PCV results in terms of the swept parameters can be visualized as a heat map, where parameters a_p and b_p are varied on the x and y axes, respectively, and an individual plot is created for each value of the

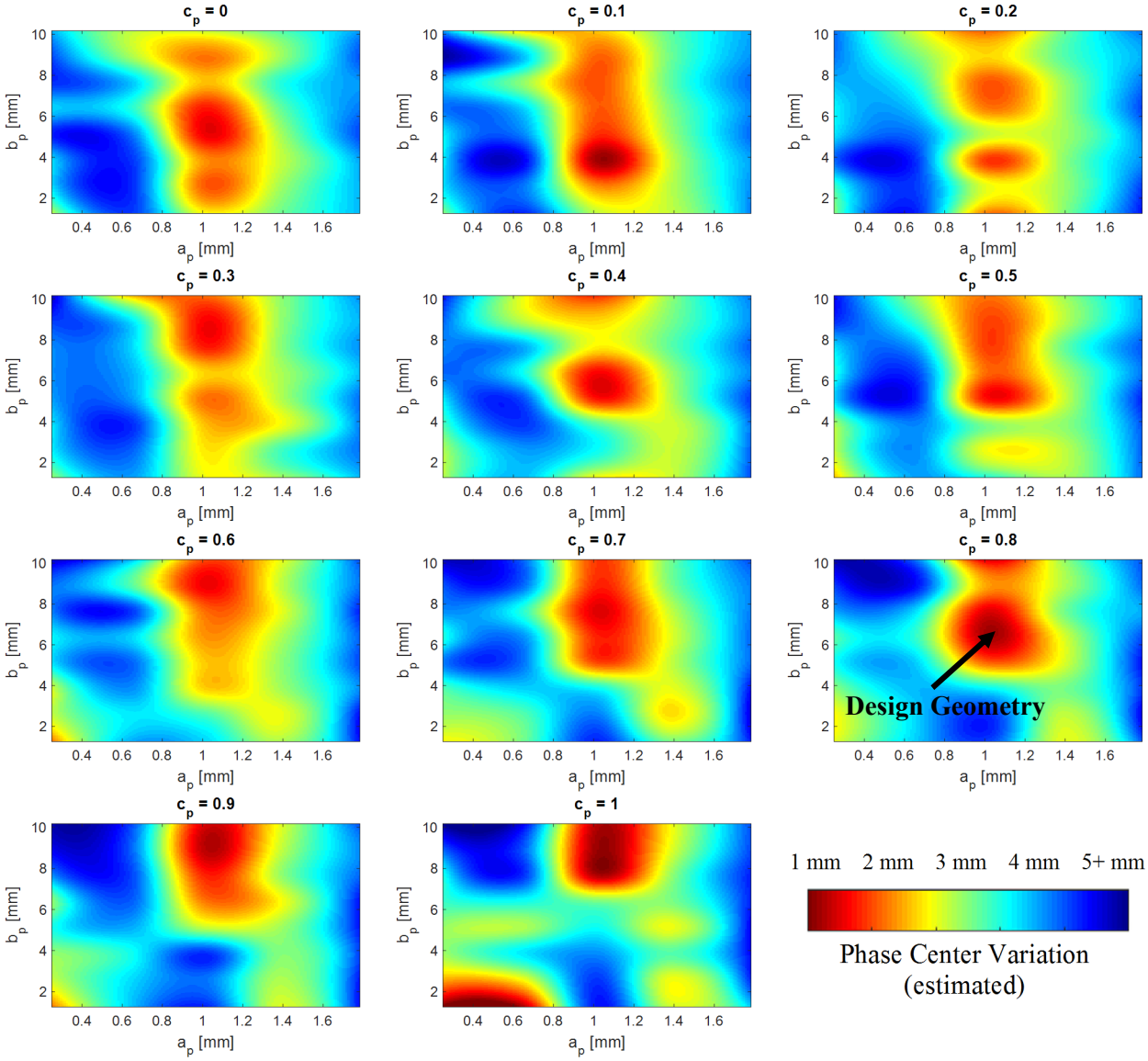

Figure 4.9. Images showing the PCV performance as a function of parameters a_p, b_p, and c_p.

third parameter, c_p (Figure 4.9). The "hot spot" in the $c_p = 0.8$ plot was chosen as the design geometry due to its PCV performance as well as the satisfaction of the requirements listed in Table 4.2. In addition to displaying the best geometric parameters in terms of PCV, viewing the results in this manner also reveals the effect that fabrication tolerances can have on the PCV of a machined or printed antenna. After running a second parametric sweep of finer parameter increments, the design in Table 4.3 was chosen.

Table 4.3. Horn 1 design dimensions (Swept parameters shaded).

Dimension	Value
a_p	1.0 mm
b_p	7.1 mm
c_p	0.79
a_1, b_1	9.8 mm
L	20.3 mm

When simulated at finer frequency points (500 MHz spacing), this geometry yielded an E-plane PCV of ~1.2 mm as computed over the 3 dB beamwidth, plotted in Figure 4.10.

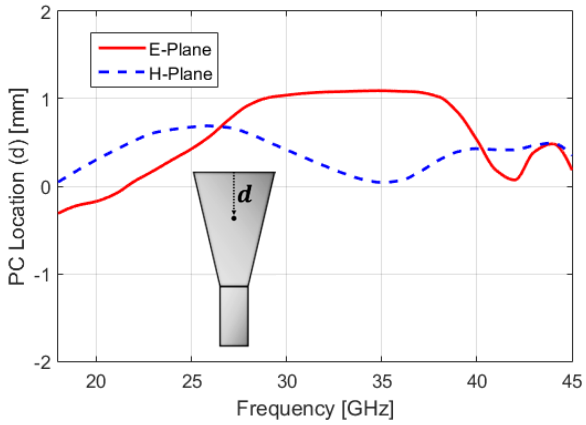

Figure 4.10. PCV of the chosen design simulated in HFSS, as computed over the 3dB beamwidth.

4.3.3 Fabrication

The horn antenna was fabricated of aluminum using reductive and additive methods: 1) CNC (Computer Numerical Control) milling and 2) DMLS (Direct Metal Laser Sintering), which is a form of metal 3D-printing. The split-block design in Figure 4.11(a) was required for machining the interior horn

features. This led to a considerable body section in order to accommodate screw holes and alignment pins used to assemble the pieces.

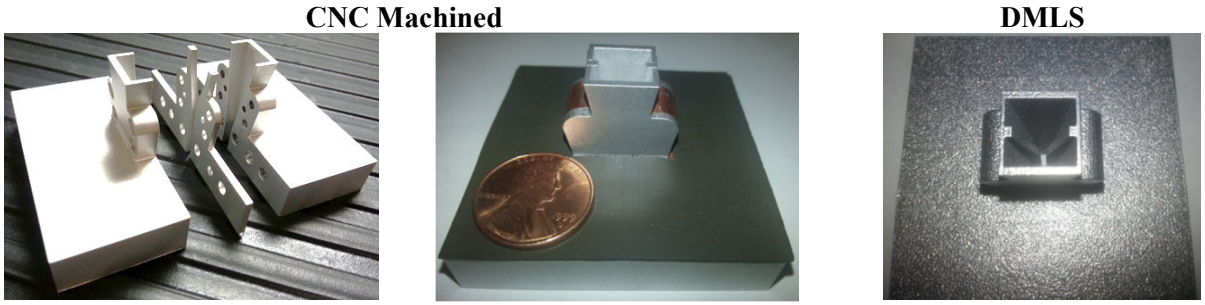

(a) (b) (c)

Figure 4.11. Prototypes of horn design 1, fabricated using CNC machining (a) disassembled, (b) assembled with adhesive absorber and (c) fabricated using DMLS.

As an additive manufacturing process, the DMLS horn can be fabricated as a solid piece but an apparent surface roughness can be seen both interior and exterior to the horn which is discussed further in section 5.5.2. Although not required in the DMLS model, the same body features were retained for direct measurement comparison between the two horns to help determine if DMLS is a viable method for fabricating horns in the 18-45 GHz frequency band.

An additional approach was considered for machining the prototype, in which EDM (Electrical Discharge Machining) would be used to machine the horn interior and CNC milling would precisely carve the ridge profiles. Due to cost and time considerations, however, a fabrication of this type was not implemented, although it would provide the advantages of both CNC and DMLS designs in that one solid piece could be constructed with smooth and precise walls and ridges.

4.3.4 Performance

The performance for both constructed horns (CNC and DMLS) will be compared in this section, as any negative effects associated with either type will influence which method is used in further designs.

Reflection coefficient measurements were taken using an Agilent Vector Network Analyzer (VNA) with a maximum frequency of 40 GHz. A custom waveguide TRL (Thru – Reflect – Line) calibration kit was used to calibrate the VNA to a reference plane at the antenna waveguide junction. Far field radiation measurements were taken in the Antenna Research Group's NSI millimeter antenna range at the University of Colorado Boulder, which employs a roll over azimuth positioner and was set up with a wideband horn antenna probe. The 10 dB beamwidth with amplitude weighting was applied in the computation of the PC. Measurements and HFSS simulations (assuming a perfectly matched waveport) are plotted in Figure 4.12.

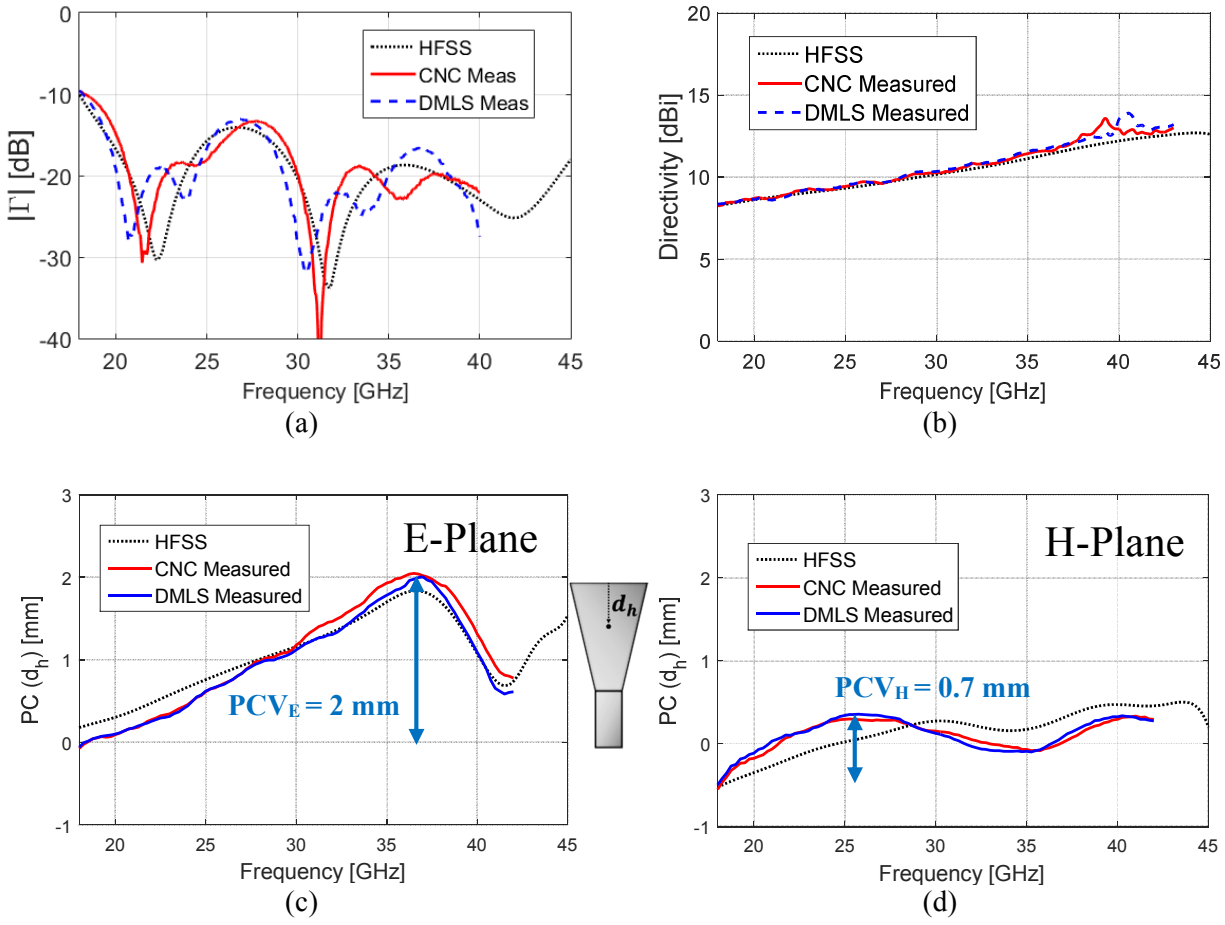

Figure 4.12. Horn 1 Simulations / Measurements: (a) Reflection coefficient (b) Directivity (c) E-Plane PC and (d) H-Plane PC computed over the 10 dB beamwidth using amplitude weighting.

PCV_E and PCV_H of 2 mm and 0.7 mm can be seen in Figure 4.12(c) and (d), respectively. Figure 4.12 (c) and (d) differ from the PCs of Figure 4.10 for several reasons: 1) the 3 dB beamwidth was used when evaluating PC in the parametric sweeps and 2) practical horn features such as a non-zero wall thickness at the aperture were not modeled in the parametric sweep simulation. Normalized radiation patterns at various frequencies are plotted below.

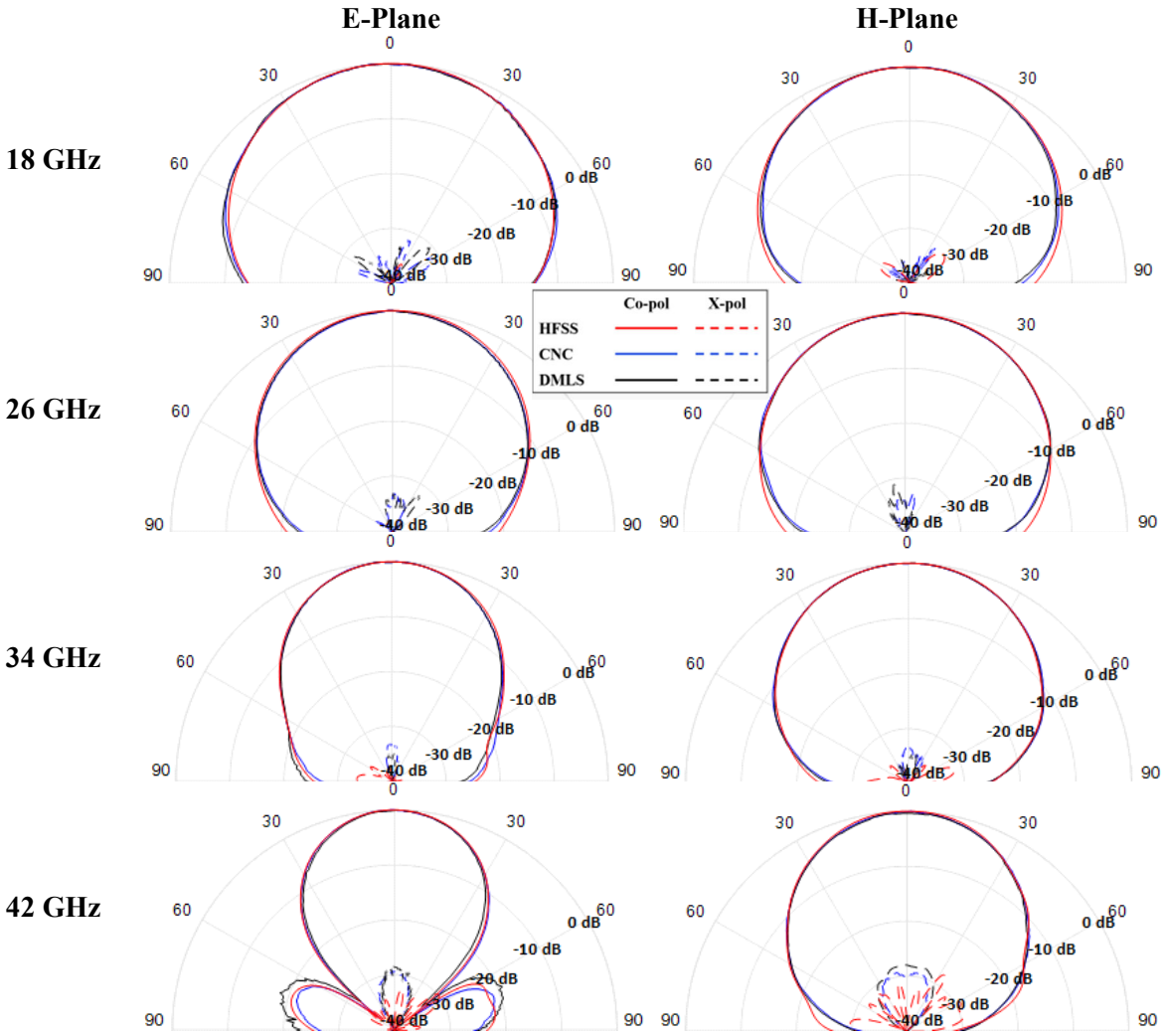

Figure 4.13. Simulated (red) and measured (blue, black) normalized radiation patterns of horn 1 at various frequencies.

Antenna range measurements are plotted up to 42 GHz, the point at which the SNR becomes too low to yield reliable data due to limited bandwidth of the up/downconverter modules. It is apparent in the

above results that neither fabrication method seems to have adverse effects on the radiation patterns, matching performance, directivity, or PCV.

4.4 Horn Design 2

A second iteration of a feed horn design was completed for the purpose of constructing an array beneath the bottom half-space of the LL. The aperture dimensions a_1 and b_1 were reduced by more than 1 mm and the flared section length of the horn L was lengthened by approximately 6 mm to allow for improved impedance matching of the antenna, particularly at the lower part of the band as compared to horn 1.

In contrast to the horn 1 parametric study discussed in 4.3.1, aluminum horn walls of 0.4 mm thickness were used in the model of horn 2, whereas a fictitious horn with zero wall thickness was used in the first iteration. In the last section, it was found that wall thickness and other practical design characteristics had an effect both on PC and reflection coefficient, making it a goal in this iteration to design the ridge profile while considering the effects of all design features. The horn 2 model is pictured in Figure 4.14a. E and H-plane symmetry planes [Figure 4.14(b)] were utilized to reduce runtime of the parametric sweep. The same ABC boundary (not shown) used for horn 1 was also used for transformation to the far fields.

(a) (b)

Figure 4.14. (a) Prototype horn 2 full model and (b) defined using E and H symmetry planes.

4.4.1 Parametric Study Results

After completing the parametric sweep, a $\sin^2$ profiled ridge design was chosen using the same method that was discussed in the previous section which will not be repeated here. The resulting dimensions are summarized in Table 4.4. Main concern was given to PCV and VSWR over the 18 – 45 GHz frequency band.

Table 4.4. Horn 2 Dimensions (Swept parameters shaded).

Dimension	Value
a_p	0.84 mm
b_p	6.86 mm
c_p	0.46
a_1, b_1	8.7 mm
L	26.8 mm

4.4.2 Fabrication

Some notable changes for the second design are summarized in Table 4.5 and the design model is pictured in Figure 4.15.

Table 4.5. Summary of Design Changes Implemented in Horn 2.

Design Change	Reason / Effects
Smaller aperture width, longer length	▪ More space efficient for LL manifold ▪ Improved VSWR at lower frequencies
Rounded aperture edges	▪ Slightly reduced PCV ▪ Improved VSWR
Filet applied to beginning of taper	▪ Improved VSWR
Thinner walls	▪ More space efficient and lightweight for LL manifold ▪ Improved PCV
Square body section	▪ Allows mounting in E or H orientation
H-plane ridges	▪ Will be required in dual-pol implementation

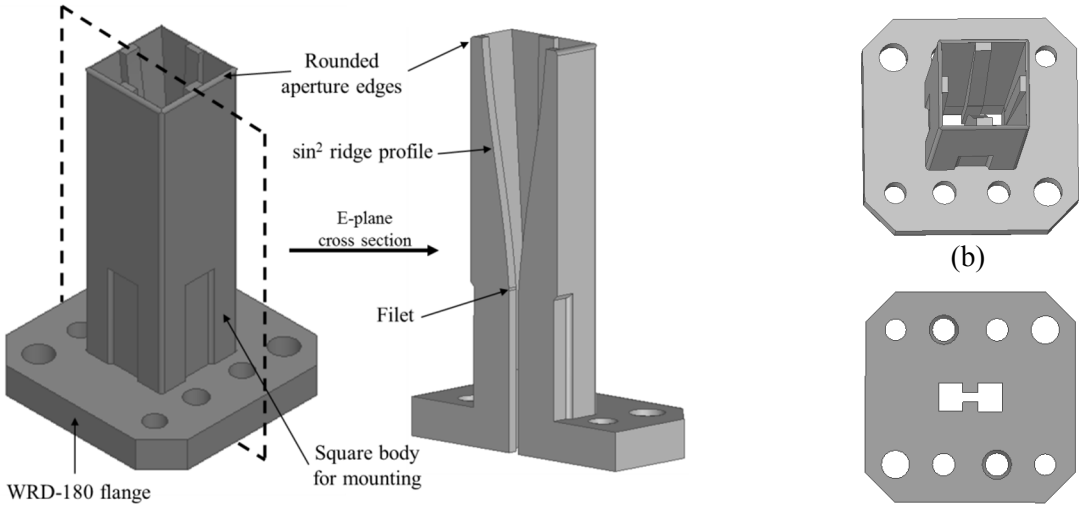

Figure 4.15. (a) Horn 2 design features (b) top view showing ridges (c) bottom view of waveguide junction.

Twelve prototypes of the horn 2 design (Figure 4.15) were fabricated using the DMLS method, taking full advantage of the ability to reduce the body size of the horn as will be necessary in order to mount multiple horns in a manifold around a LL. The wall thickness at the aperture is 0.4 mm and increases for structural integrity toward the horn throat. A square cross section directly above the flange was maintained such that the horn can be mounted in the E or H-plane orientation into the manifold discussed in the next chapter. The fabricated horn is shown in Figure 4.16.

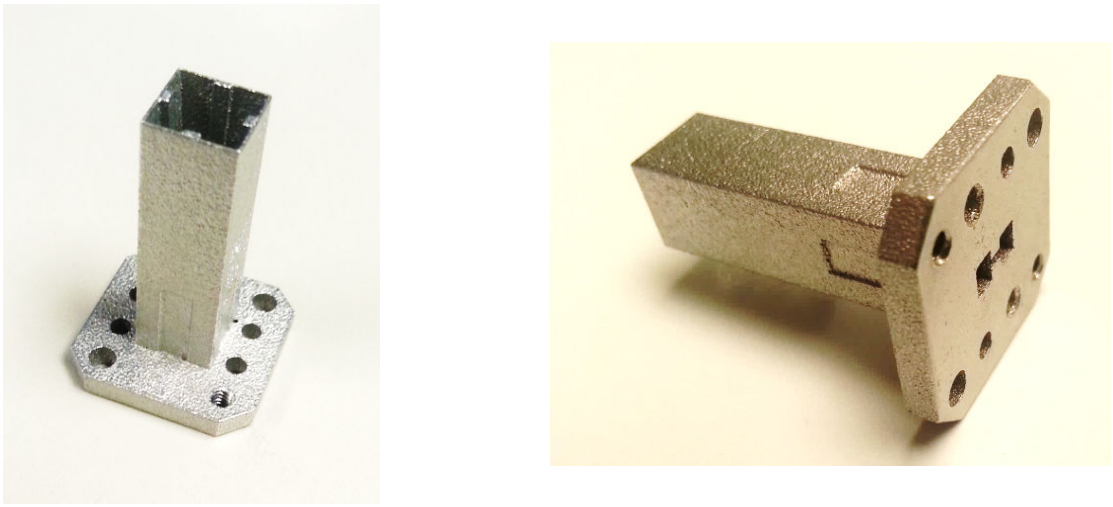

(a) (b)

Figure 4.16. Prototype horn 2 (a) isometric view (b) waveguide junction flange.

4.4.3 Performance

Of the twelve feed horns, nine were installed into the manifold discussed in the next chapter. The remaining three were used for measurements taken in this section and are designated H_1, H_2, and H_3. Reflection coefficient measurements were taken using a VNA (Vector Network Analyzer) with a maximum frequency of 40 GHz. A custom waveguide TRL (Thru – Reflect – Line) calibration kit was used to calibrate the VNA to a reference plane at the antenna waveguide junction. Measurements and HFSS simulations (assuming a matched waveport) are plotted in Figure 4.17.

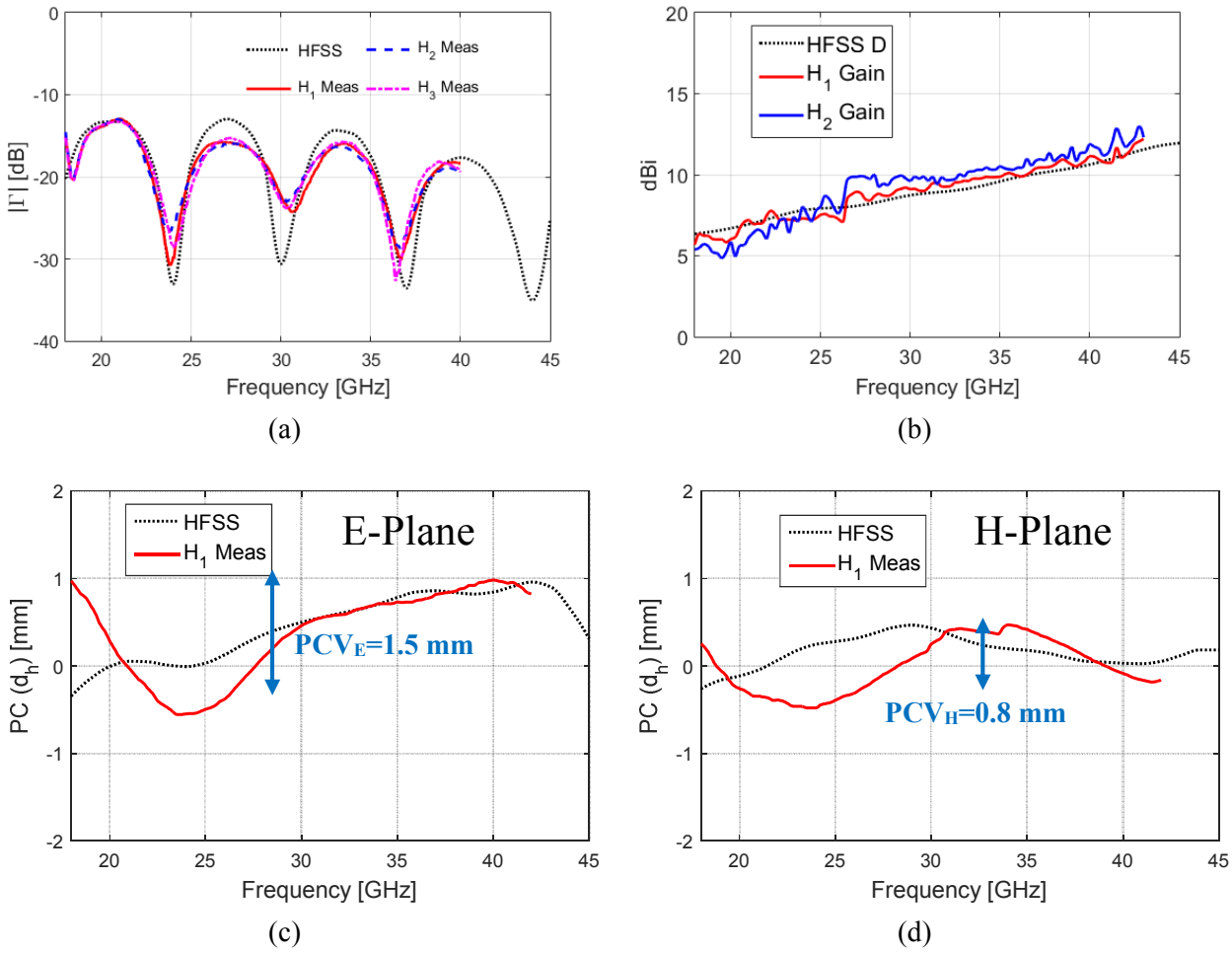

Figure 4.17. Horn 2 Simulations / Measurements: (a) Reflection coefficient (b) Directivity / Gain (c) E-Plane PC and (d) H-Plane PC. PCs were computed over the 10 dB beamwidth using amplitude weighting.

Reference gain measurements were required to compute gain of the AUT in Figure 4.17(b). The reference measurements were acquired using standard gain horns in the 18 – 26.5 GHz and 26.5 – 45 GHz bands. The inconsistent gain offset (relative to directivity) in the AUT data on either side of 26.5 GHz indicates there may be a deviation between the assumed gain and actual gain exhibited by the standard gain horns.

The PCV was measured to be 1.5 mm in the E-plane and 0.8 mm in the H-plane. While there was some slight disagreement between PC at the lower frequencies, the overall PCV expected from the simulations was observed in the measurement. At lower frequencies, the antenna pattern is more susceptible to impacts from the mounting hardware and absorber due to the wider beamwidth. For these measurements, absorber was placed 5 mm below the aperture.

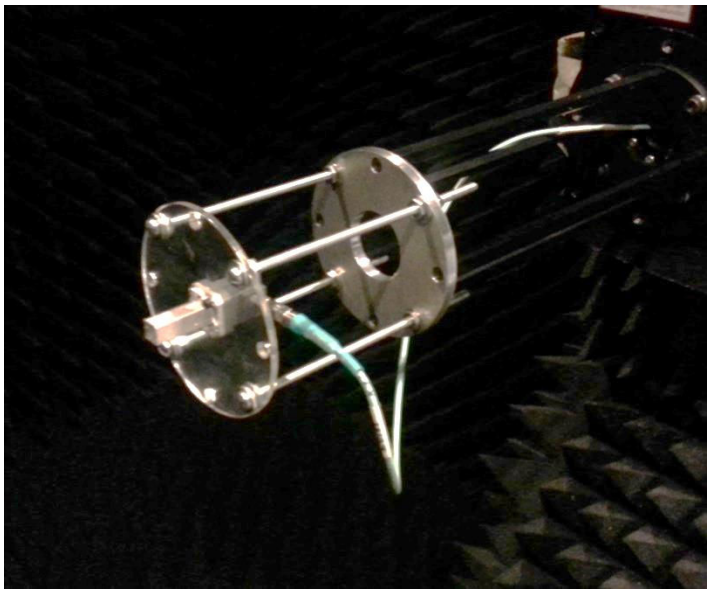

Figure 4.18. Prototype horn 2 mounted in the antenna range, before placing microwave absorber below the aperture opening.

Simulated and measured radiation patterns are plotted in Figure 4.19.

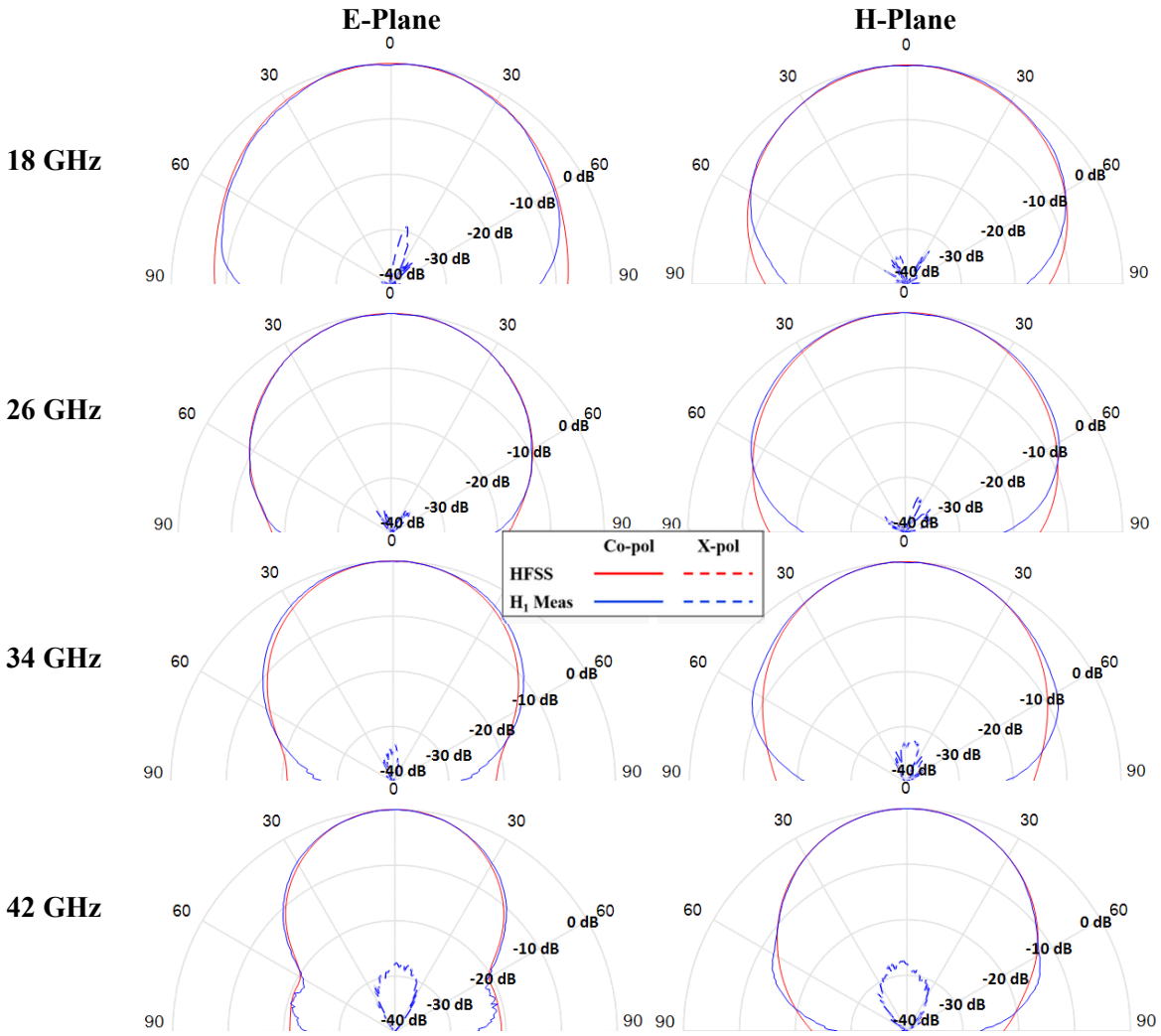

Figure 4.19. Simulated (red) and measured (blue) normalized radiation patterns of horn 2 at various frequencies.

4.5 Summary

During the design process of horn 1, some valuable insight was gained which led to a second design more suited to the application at hand. Some main observations with respect to the two horns are as follows:

- Horn 1 prototypes as manufactured using CNC and DMLS both perform similarly, despite the undesired features inherent to each method.
- The directivity and gain, as expected, is lower for horn 2 due to the smaller aperture size.

- PCV_E is lower for prototype horn 2 (1.5 mm) as a result of reducing the aperture size and conducting the parametric sweep while considering the wall thickness at the aperture of the horn.
- The mean value of PC over frequency is located closer to the aperture of horn 2.
- The maximum reflection coefficient measured for horn 2 is 3 dB lower than for horn 1.

Both designs will be mounted for measurement with the LL in the next chapter for comparison, however only horn 2 is intended to be mounted as a feed array to the LL.

Chapter 5

Luneburg Lens / Feed Horn Implementation

5.1 Introduction

Throughout the feed antenna design process, a stable LL focal point has been assumed over the bandwidth of interest. This, in turn, made a feed antenna with minimal PCV over frequency highly desirable. It will be shown in section 5.2, however, that the focal point of the two-layer nonuniform LL can vary with frequency, further complicating the relationship between feed position, feed PC, and LL focal point. In addition, reflections between the lens, feed antenna, and within the lens itself can cause additional scattering and coupling between multiple feeds placed in the vicinity of one another. This will affect system performance such as gain, sidelobe level (SLL), and reflection coefficient. Due to the very complex nature of the problem at hand, a numerical approach is most appropriate for determining the optimal placement of the feed horns with respect to the LL surface.

The LL being used in this study is a two layer lens as pictured in Figure 5.1. Using known permittivities of each layer, this lens was able to be modeled using the finite element method (FEM) solver within HFSS with losses neglected in the initial analysis. A loss analysis of the lens is discussed in section 5.5.3. The actual lens used for measurements was designed and supplied by Lun' Tech of Perols, France.

(a) (b)

Figure 5.1. (a) 2-layer LL HFSS model with transparent outer layer and (b) manufactured lens.

5.2 Luneburg Lens Simulation – Open-Ended Waveguide

The aperture of an open-ended waveguide (OE-WG) was swept in distance from the LL surface as a means of determining the lens's focal point numerically.

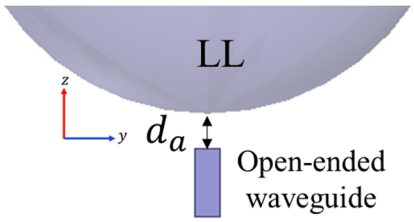

Figure 5.2. HFSS model of an open-ended waveguide feeding the LL, separated by a distance d_a.

The focal point is determined as the OE-WG aperture location that results in maximum directivity and peak sidelobe level (SLL), where SLL is positive and is relative to the maximum directivity. Figure 5.3(a) and (b) show maximum directivity and peak SLL as functions of lens / OE-WG separation (d_a) and frequency. To cover the 18 – 45 GHz bandwidth, three waveguide cross sections (WR-42, WR-28, and WR-22) were used over their respective operation bandwidths. The values in each frequency column of Figure 5.3 are normalized to 0 dB.

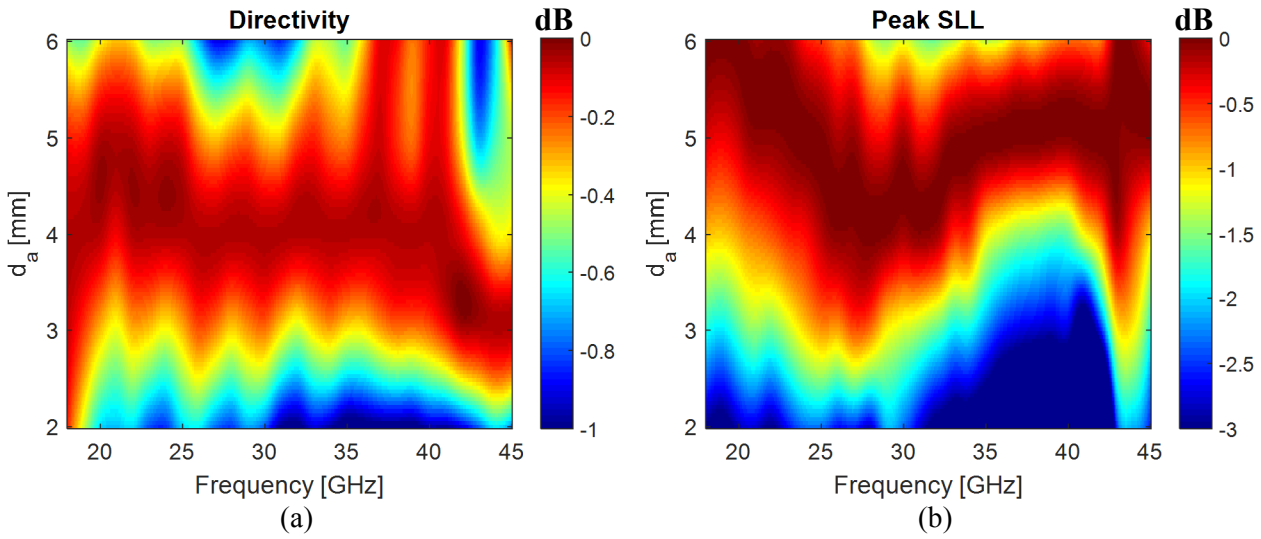

Figure 5.3. Simulated 2-layer LL performance when fed with an OE-WG, as a function of aperture distance from the surface (d_a) and frequency, (a) normalized directivity and (b) peak SLL normalized to 0 dB at each frequency.

Note that the scale is larger for SLL since it is more sensitive to waveguide separation d_a than is directivity. Although the focal point for this lens appears to be in the region between 4-5 mm, it will be defined formally as the point that maximizes performance over the frequency band as determined by χ_D, defined as

$$\chi_D(d_a) = \frac{1}{N}\sum_{f=f_1}^{f_N} |1 - D_n(f, d_a)|^2 \tag{5.1}$$

where N is the number of frequencies simulated and $D_n(f, d_d) = \frac{D(f,d_d)}{D(f)_{\max}}$ is the normalized directivity (linear form) as a function of frequency f and d_a. The distance d_a at which χ_D is minimum will reveal the optimum placement of the horn aperture according to (5.1). Similarly, χ_{SLL} can be defined in terms of peak SLL performance:

$$\chi_{SLL}(d_a) = \frac{1}{N}\sum_{f=f_1}^{f_N} |1 - SLL_n(f, d_a)|^2 \tag{5.2}$$

where again, the peak SLL is normalized at each frequency and is in linear form spanning (0 – 1). χ_D and χ_{SLL} for the OE-WG simulation are plotted in Figure 5.4.

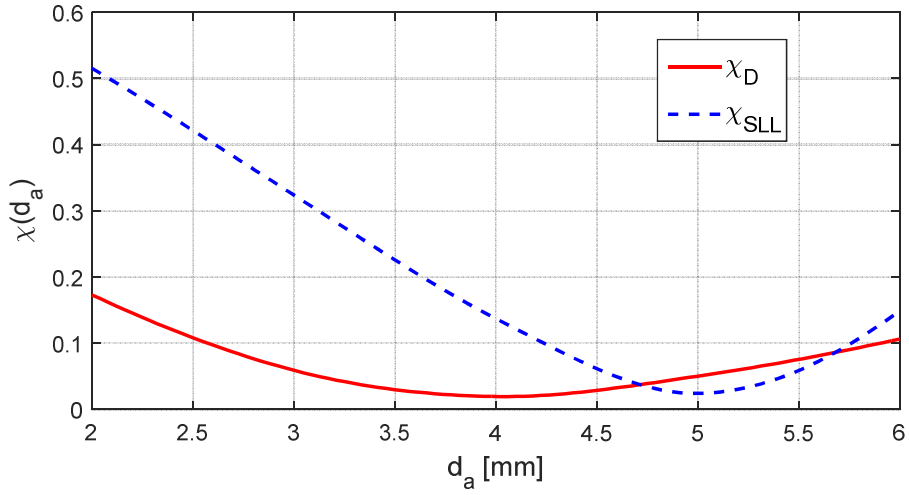

Figure 5.4. χ_D and χ_{SLL} as determined using (5.1) and (5.2) for the OE-WG / LL simulation.

The minimums of χ_D and χ_{SLL} are separated by about 1 mm. For this reason, the focal point of a non-ideal lens, like the definition of the PC of the feed antenna, is not trivial and must be determined using specific design requirements.

5.3 Luneburg Lens with Single Feed Antenna

The aperture of prototype horn 1 was positioned under the LL according to Figure 5.5 for simulation in HFSS. Neglecting effects such as reflections and coupling, at a single frequency f_i one would expect an optimum aperture location of

$$d_{a_i} = f_{p_i} - d_{PC_i} \tag{5.3}$$

where d_{a_i} is the distance between feed aperture center and lens surface, f_{p_i} is the focal point of the lens at frequency f_i, and d_{PC_i} is the computed phase center offset relative to the horn's aperture at frequency f_i.

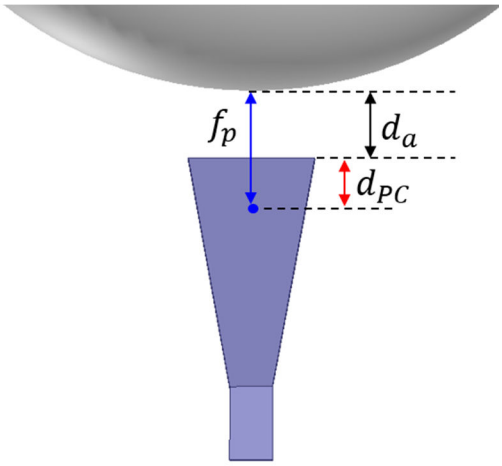

Figure 5.5. Expected optimum horn feed position with respect to its PC offset d_{PC}, the lens focal point f_p, and the LL / feed separation d_a.

5.3.1 Horn 1

Like the OE-WG simulation, the horn was swept in distance d_a from the surface of the lens in HFSS. Results are shown in Figure 5.6, with the optimum horn location determined using the metrics given in (5.1) and (5.2). Ideally, the best performance at each frequency in Figure 5.6(a) and (b) would correspond to (5.3). There exist several obstacles in determining the feed position using (5.3), however. First is that d_{PC} will vary depending on how it is computed. Unlike for a reflector antenna [26], an "appropriate" definition pertaining to the LL has yet to be developed. Second, the focal point was measured using an OE-WG, which illuminates the lens differently than the horn. Since the horn is more directive, a smaller portion of the lens will be illuminated as the frequency increases. Lastly and most importantly, the focal point and PC were both computed in separate simulations of the lens and horn, respectively. When arranging the two structures less than 1 cm from each other there is an interaction that will invalidate the simple relationship in (5.3) due to reflections, scattering, and coupling if other feed antennas are present.

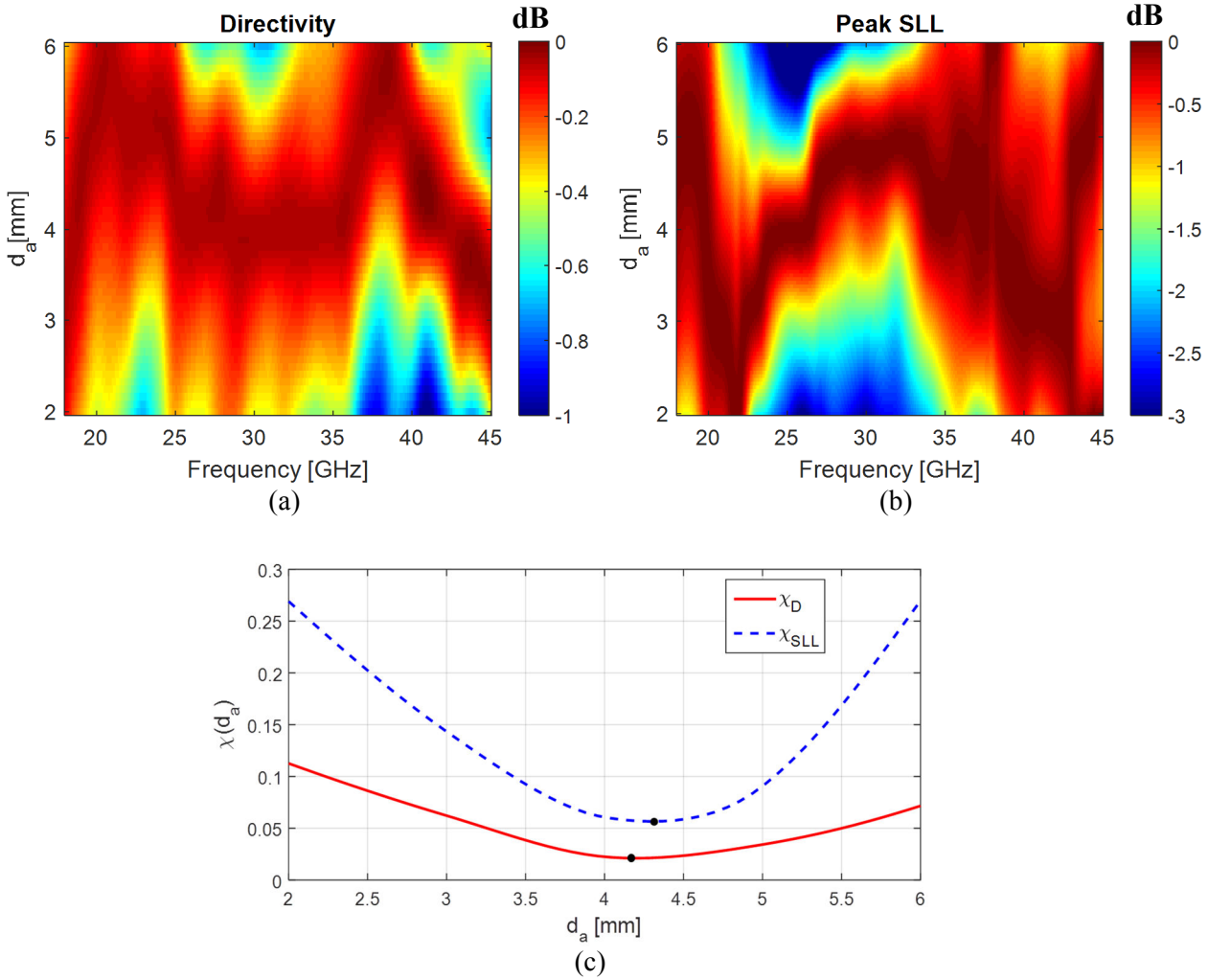

Figure 5.6. Horn 1 / LL performance vs position in terms of (a) directivity and (b) peak SLL. The focal point in terms of χ_D and χ_{SLL} is found as the minimum of the plots in (c).

The interaction between feed and LL is evident in plotting the feed VSWR as a function of d_a and frequency (Figure 5.7). Ideally, the inner and outer boundaries of the lens would be well matched and VSWR would not change with d_a, as is true with for LL with more layers (Appendix C). A clear variation, however, can be seen in the y-axis of Figure 5.7 and is at its worse at 27 GHz between 4 – 5 mm. This is not surprising since the outer layer of a 2 layer LL is not as well matched to free space as say, a 10 layer lens would be. Although the lens's contribution to VSWR at a given frequency will ultimately decrease with increasing distance d_a, there exists a periodicity in the VSWR that can be seen

in Figure 5.7 depending on the phase of the reflected fields. The feed horn by itself will have internal reflections and in some cases, the reflection from the lens may add destructively to lower the overall VSWR as measured at the feed input. Conversely, the reflections add constructively to raise the VSWR at some frequency / distance combinations.

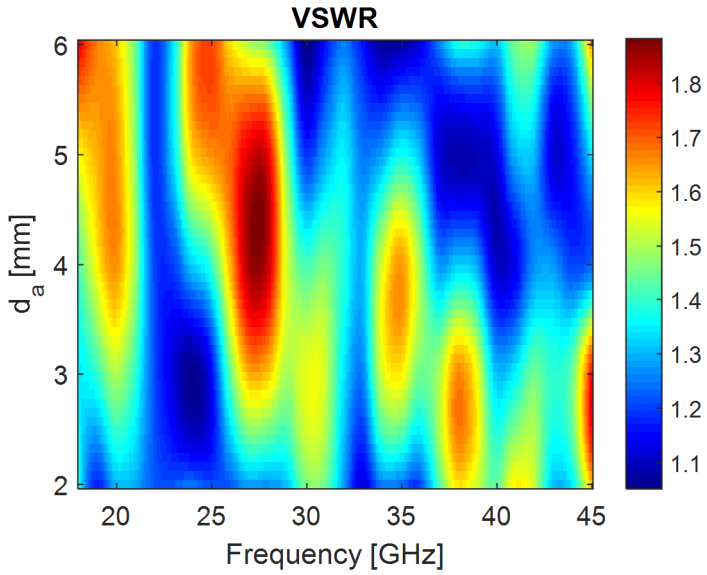

Figure 5.7. Horn 1 VSWR (simulated) versus the horn / lens separation d_a and frequency.

A bracket (Figure 5.8) was designed and fabricated with the use of 3D printing to secure the LL and allow for the mounting of the horn 1 prototype antenna a fixed distance from the LL surface. Thin shims were used to set the distance of the feed aperture to $d_a = 4.3$ mm. The bracket material consists of PLA (polylactic acid) type plastic. When simulated with and without the mounting bracket, the radiation pattern revealed no significant impact due to its presence. Further discussion of the mounting bracket can be found in Appendix B. Simulated versus measured performance is shown below.

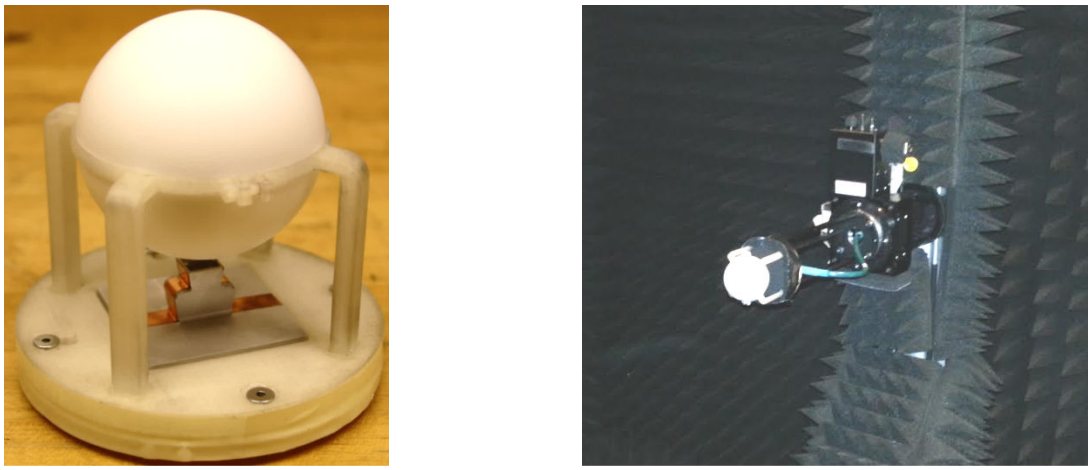

(a) (b)

Figure 5.8. CNC horn 1 mounted with LL (a) on bench and (b) installed in antenna range before wrapping the lower mount with microwave absorber.

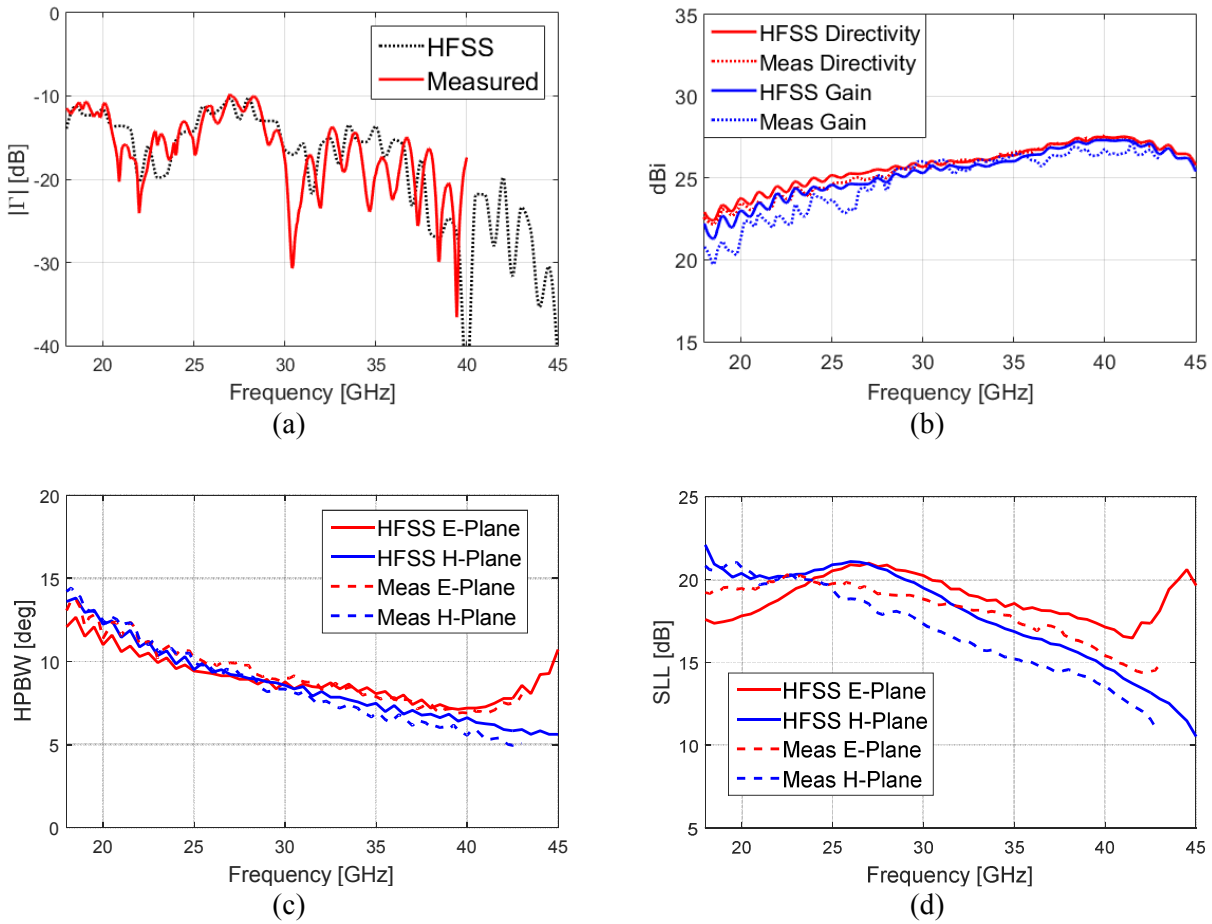

Figure 5.9. Simulations / measurements of horn 1 (CNC) mounted with the LL, (a) reflection coefficient (b) directivity / gain (c) HPBW and (d) peak SLL.

The drop-off in directivity [Figure 5.9(b)] above 40 GHz corresponds with a widening of the E-plane HPBW [Figure 5.9(c)]. Note that horn 1, when measured without the lens, does not have the same drop in directivity [Figure 4.12(b)]. This effect, as it pertains to both the lens and the feed, will be discussed later in the chapter. Measured antenna patterns at several frequencies are compared to the HFSS simulation in Figure 5.10.

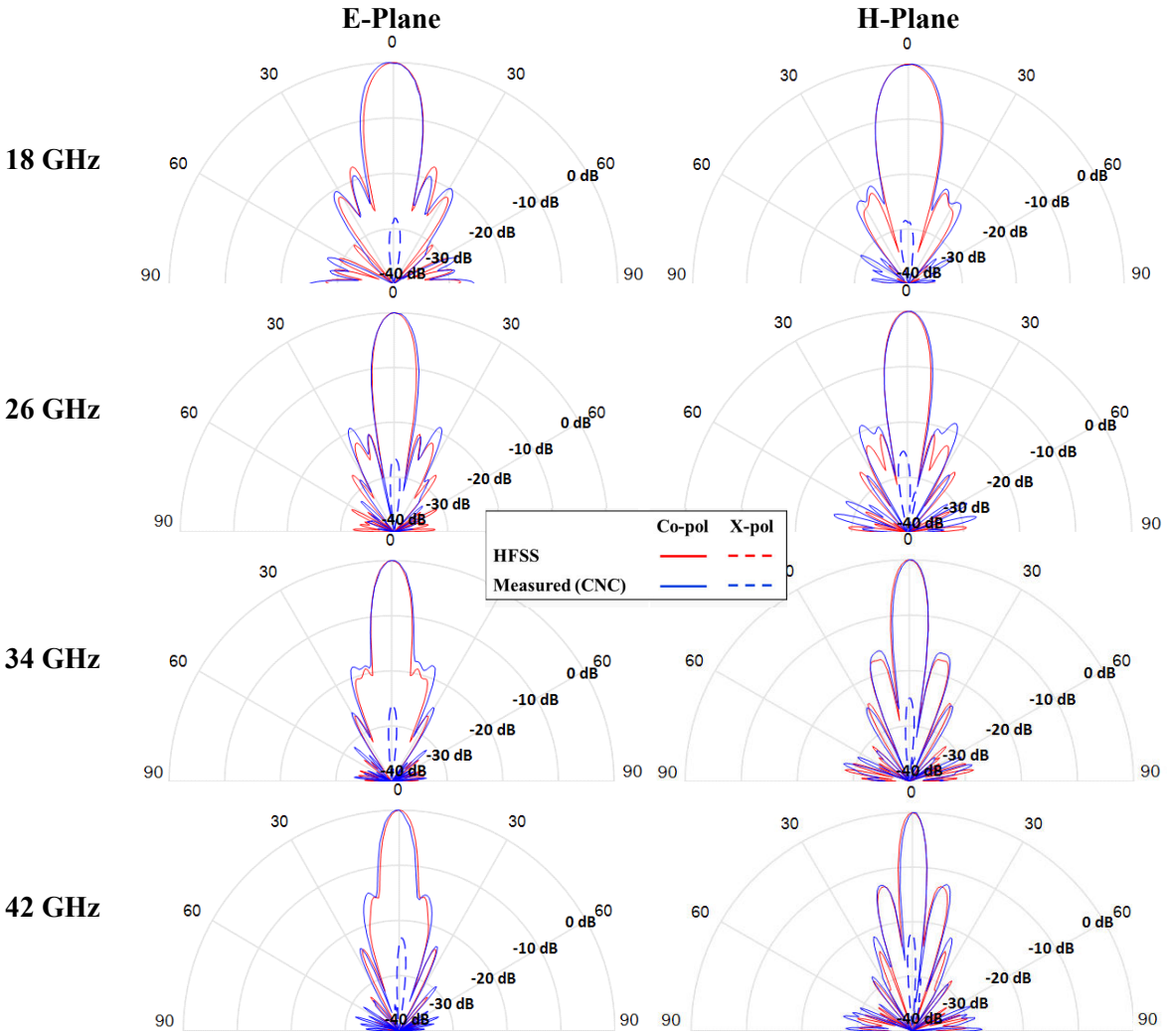

Figure 5.10. E / H-plane antenna patterns of prototype horn 1 (CNC) mounted with the LL.

In most cases, the sidelobes were exacerbated in the measurements by 1 – 2 dB but for the most part the measurements maintained the same features as the simulations.

5.3.2 Horn 2

Horn 2 was also swept in distance d_a in HFSS to determine an ideal mounting position for use in the manifold discussed in the next section. Results are plotted in Figure 5.11.

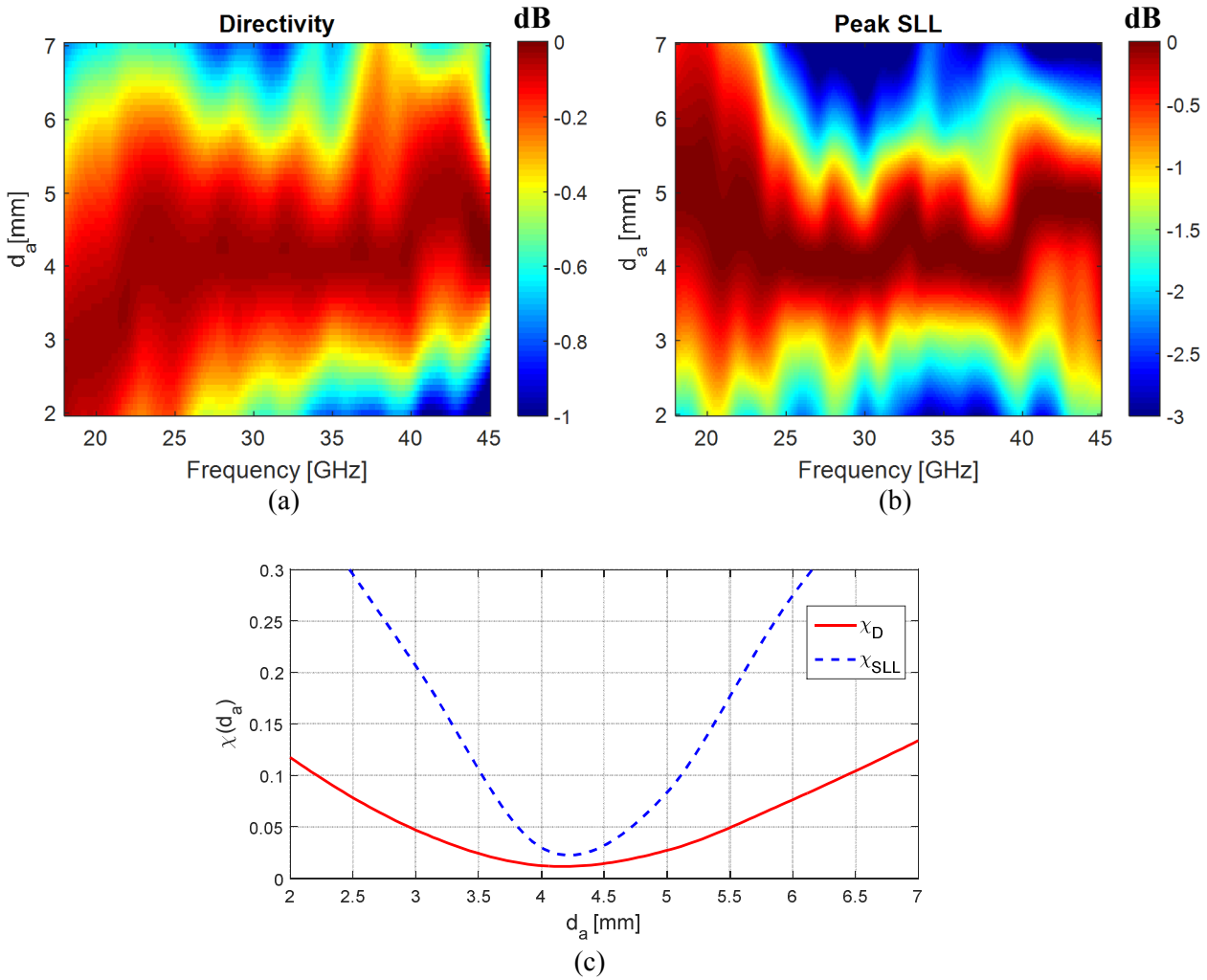

Figure 5.11. Horn 2 / LL performance vs position in terms of (a) directivity and (b) peak SLL. The focal point in terms of χ_D and χ_{SLL} is found as the minimum of the plots in (c).

Note a more overall stability in terms of both directivity and peak SLL as a function of position than for horn 1. The minima of χ_D and χ_{SLL} coincide at the same distance of $d_a = 4.2$ mm. The position's effect on VSWR is shown in Figure 5.12.

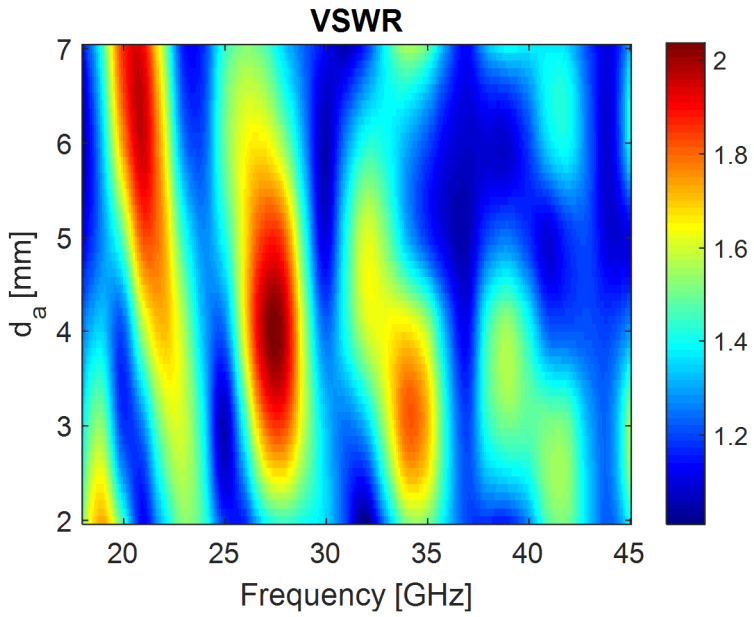

Figure 5.12. Horn 2 VSWR (simulated) versus the horn / lens separation d_a and frequency.

The "hot spots" in Figure 5.12 are similar to those seen in Figure 5.7 which indicates the behavior to be more dependent on lens characteristics than on the feeds. A new metric, χ_{RG}, can also be considered which is similar to χ_D but instead plots the realized gain which includes mismatch loss corresponding to the VSWR profile in Figure 5.12. The minimum of χ_{RG} is located at 4.28 mm which is only 0.08 mm from the minimum of χ_D.

5.4 Luneburg Lens with Multiple Feeds

A feed manifold was designed for use with prototype horn 2 enabling the assembly of two curvilinear 1x5 arrays, one along the xz plane and one along the yz plane as shown in Figure 5.13 requiring nine feeds in all. Figure 5.13(b) shows the labeling convention for the different feeds, as viewed from the bottom of the manifold where the waveguide flanges are visible.

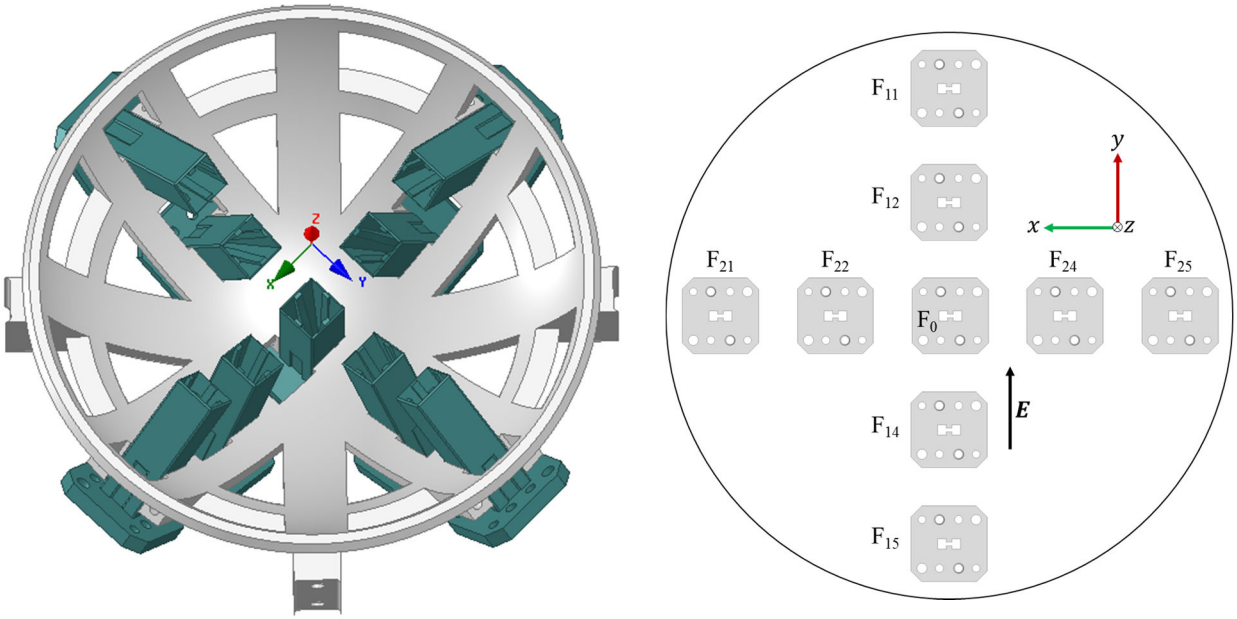

(a) (b)

Figure 5.13. (a) Feed manifold CAD model pictured without the lens or supports, (b) feed array labeling as the array ordering would appear looking from the bottom of (a).

The feed F_0 is the bottom center feed and will radiate maximally at the lens's boresight ($\theta = 0$). Throughout this chapter, the two arrays will be referred to as the E-plane array ($F_{11} - F_{15}$) and H-plane array ($F_{21} - F_{25}$) indicating that the E or H-planes of the feed horns are in the same plane for the given array. The horns in both arrays are separated by an angle θ_h (Figure 5.14).

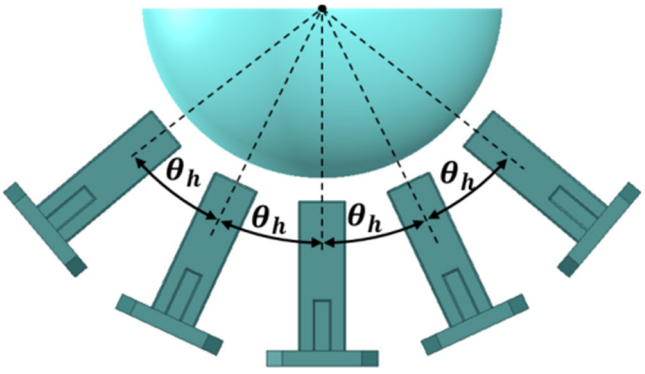

Figure 5.14. Feed separation angle θ_h.

With the directivity of the lens expected to be > 20 dBi, the five element array will not provide continuous beam coverage in the lens's far field. The prime purpose for this implementation, however, is to study the effects of coupling and demonstrate the mounting of multiple feeds in the vicinity of one another under a LL. The fully assembled manifold is pictured in Figure 5.15.

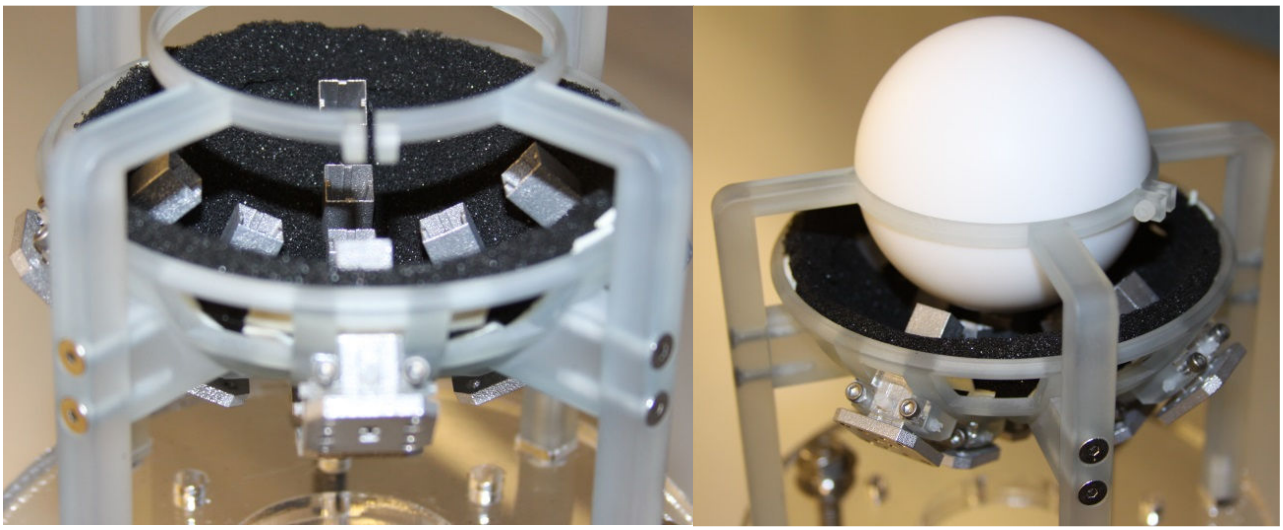

(a) (b)

Figure 5.15. Feed manifold (a) without LL (b) with LL installed.

5.4.1 S-Parameters

The feeds in the manifold are separated by $\theta_h = 25°$ in both E and H arrays. With the E and H arrays populated, S-parameter measurements were taken using an Agilent VNA up to its maximum of 40 GHz. The measurements are plotted in Figure 5.16 and are organized into reflection coefficient, E-plane element coupling, H-plane element coupling, and cross coupling between elements in the two curvilinear arrays. Redundant measurements are omitted from the plots below, e.g. the coupling between feeds F_{21} and F_{24} (S_{24_21}) is assumed to be the same as the coupling between F_{22} and F_{25} (S_{25_22}) due to symmetry and therefore only one of the measurements is plotted.

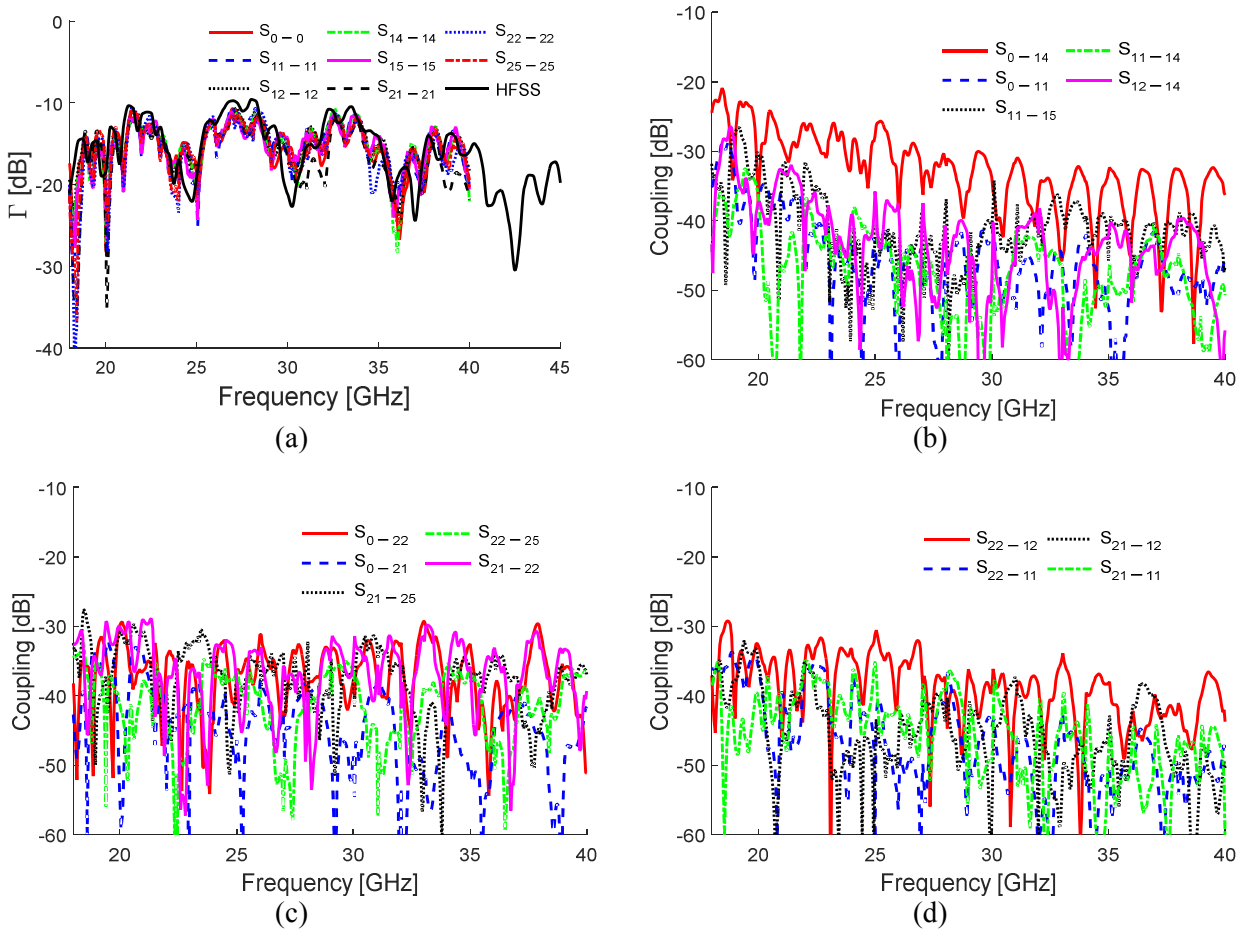

Figure 5.16. S-measurements between numerous feed element combinations: (a) Reflection coefficient (S_{11}), (b) E-array element coupling, (c) H-array element coupling, (d) cross coupling between E/H-plane elements.

The worse-case coupling is below -20 dB which occurs for feeds adjoining one another in the E-plane array at the lower frequencies. In Figure 5.17, the E-field magnitude cross sections of the E and H arrays are shown with the center element F_0 excited at 18 GHz. In the *y* direction (E-plane) of the feed's aperture, the E-field is normal to the horn edges which results in diffraction and a more spread out near field that is seen to couple into the neighboring element, resulting in the much higher coupling seen between F_0 and F_{14} whereas most other element pairs are -30 dB or less across the frequency band.

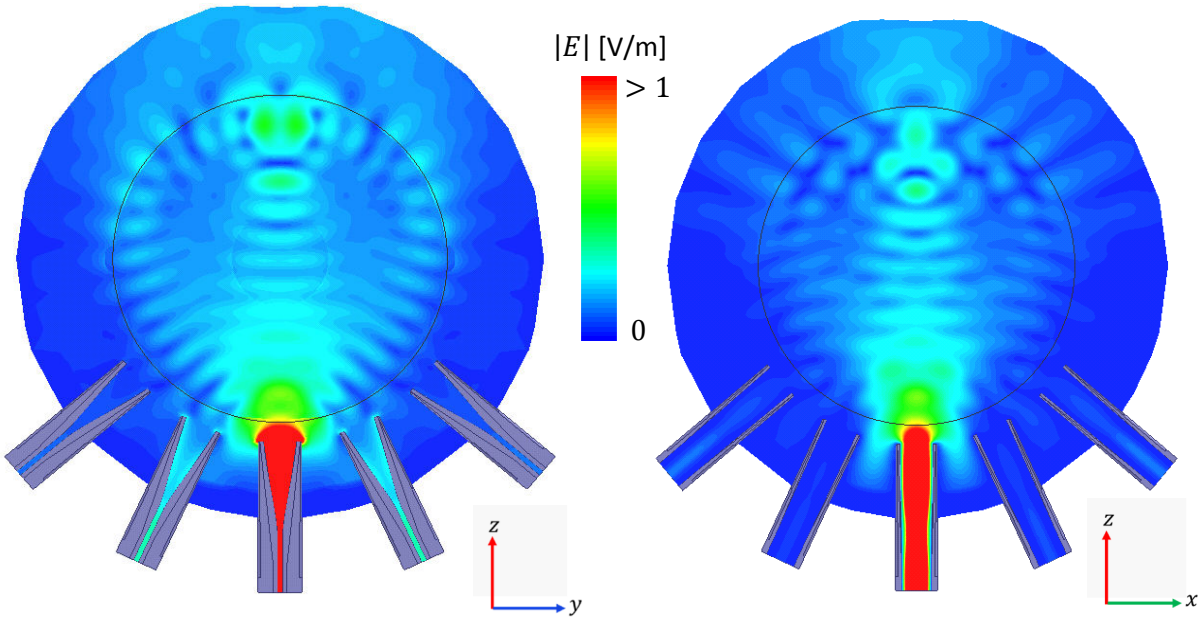

(a) (b)

Figure 5.17. E-field magnitude when fed by the center element F_0 in (a) E-array and (b) H-array cross sections at 18 GHz, normalized to the E-field intensity incident on the LL.

The two outer horns are separated by $\theta_h = 100°$ and it can be expected that S_{15_11} and S_{25_21} will increase as θ_h approaches 180°. HFSS simulations reveal coupling levels on the order of -10 dB for $\theta_h = 180°$.

5.4.2 Simulations / Measurements

In both HFSS simulations and range measurements of the feed manifold, the horns were positioned a distance d_a = 4.2 mm from the lens surface as a result of the χ_D and χ_{SLL} plots in Figure 5.11. The process of mounting the feed horns is discussed in Appendix B. Absorber was lined on the top surface of the manifold [Figure 5.15(a)] in an attempt to mitigate effects from the mounting hardware beneath the manifold surface during the initial analysis of the system. The manifold as mounted in the anechoic chamber is pictured in Figure 5.18.

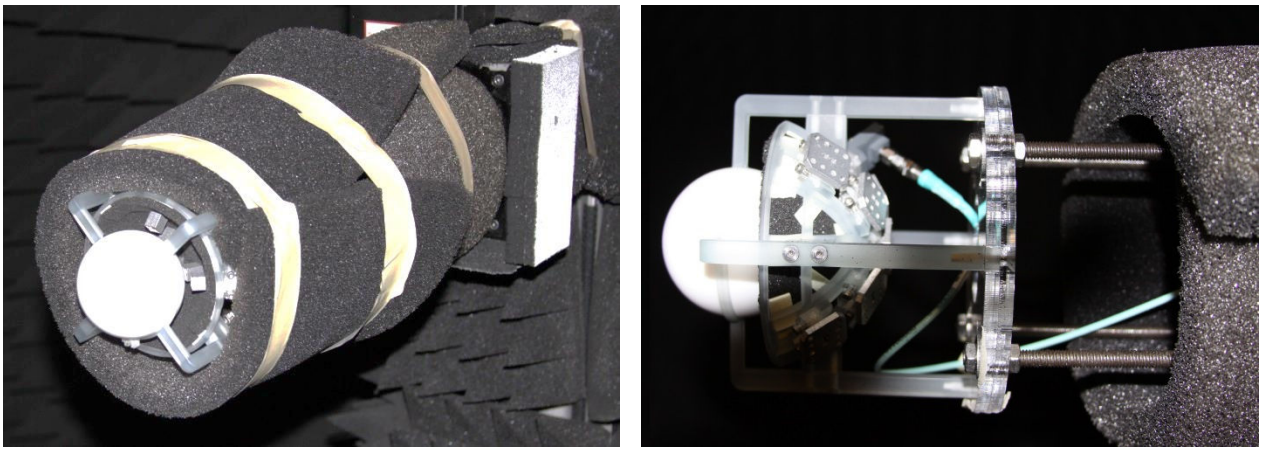

(a) (b)

Figure 5.18. Lens manifold mounted in antenna chamber (a) front view (b) side view with F_{11} connected as the AUT feed and microwave absorber removed.

In post-processing, HFSS can excite the desired number of feeds to view any combination of beams. The 36 GHz 3D polar gain pattern with all feeds excited is shown in Figure 5.19(a). Due to symmetry, only three beams were measured in the antenna range: F_0, F_{12}, and F_{11} and their individual patterns are superimposed onto each other as shown in Figure 5.19(b).

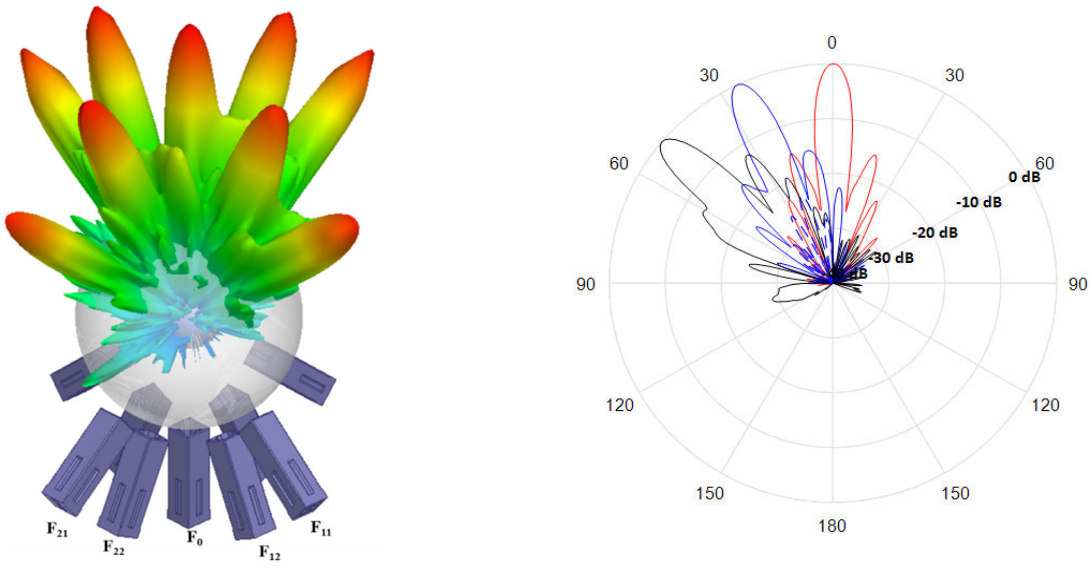

(a) (b)

Figure 5.19. (a) All feeds excited in HFSS and (b) E-plane of the three unique E-array feeds measured in the antenna range at 36 GHz.

Because the antenna range employs a roll-over-azimuth positioner for scanning the AUT, only one principal plane of the off-axis feeds (F_{11} and F_{12}) will be measured in one continuous scan and the H-plane will be plotted for F_0 only. Patterns for the three measured beams are plotted in Figure 5.20.

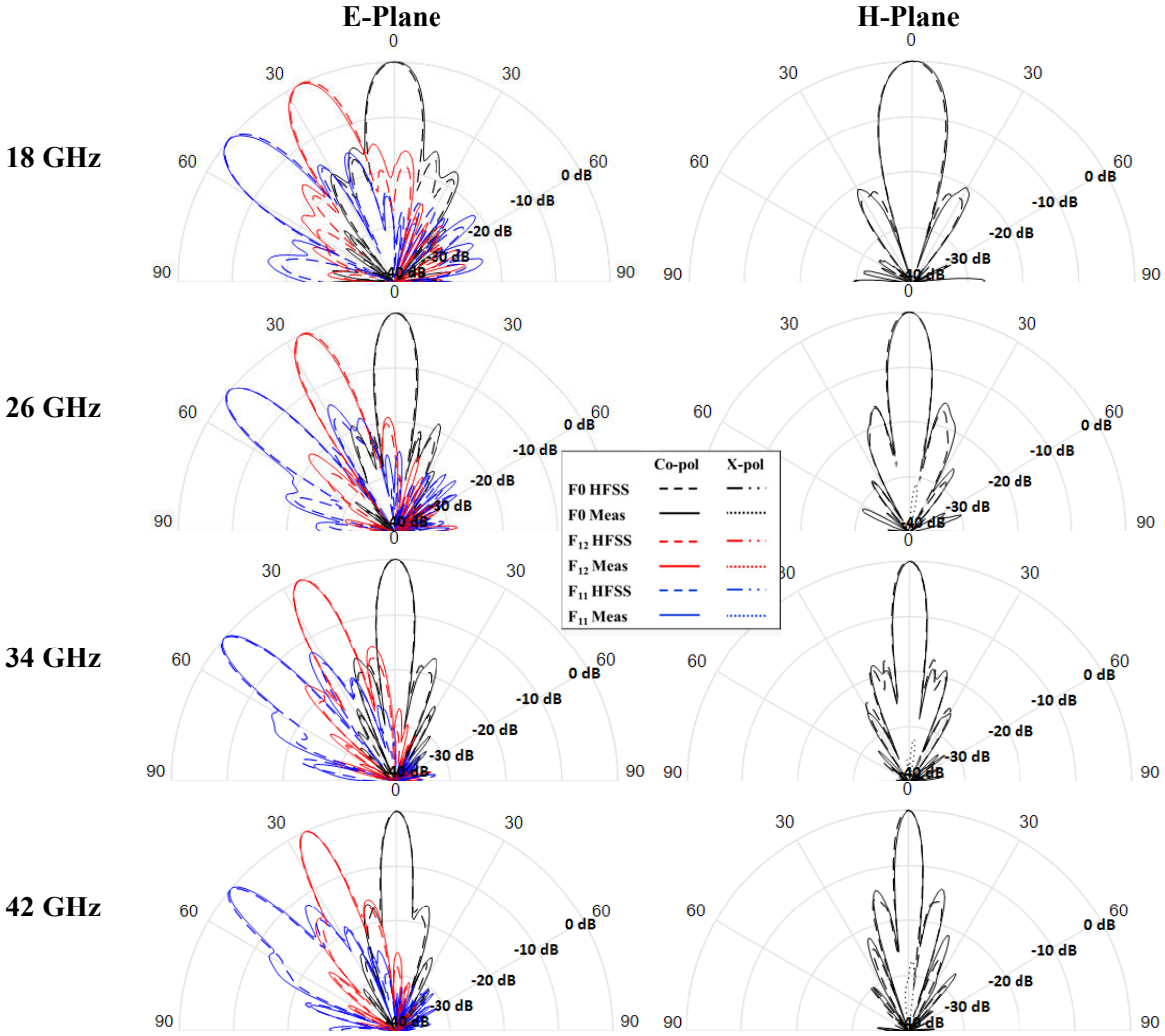

Figure 5.20. Normalized radiation patterns of F_0, F_{12}, and F_{11}.

The peak SLL and HPBW measured for F_0 are plotted in Figure 5.21.

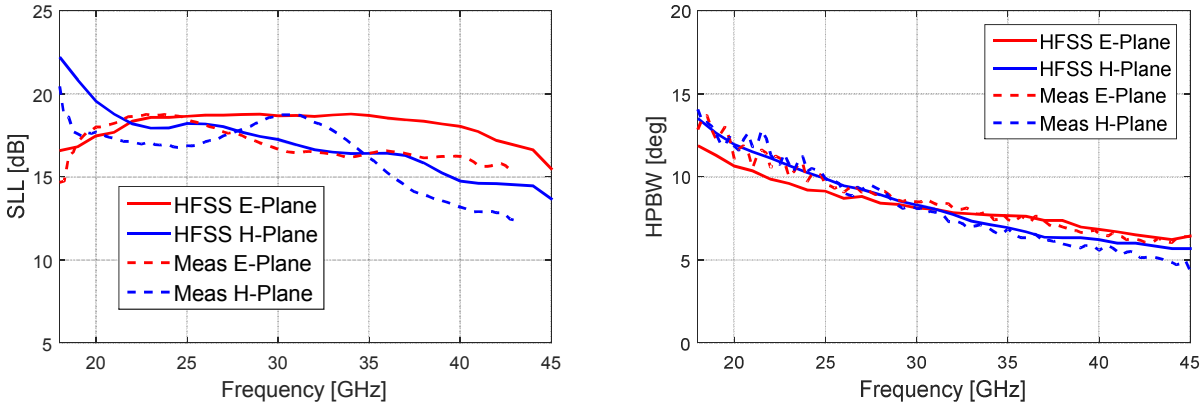

(a) (b)

Figure 5.21. F_0 Simulated and measured E / H plane (a) peak SLL and (b) HPBW.

As in the horn 1 / LL measurements, the maximum SLL occurs in the H-plane at most frequencies. The highest sidelobes that can be expected for the given configuration are located at about 14 dB when simulated, but are likely closer to 10 dB when measured up to 45 GHz. SLL measurements were only plotted to 43 GHz, above which the measurement SNR was too low to accurately measure the sidelobes.

The gain was measured and compared to HFSS simulations and is plotted in Figure 5.22(a). The dip at 39 GHz is thought to be from an external factor in the measurement, given that horn 2 exhibited no obvious losses at this frequency and it was not measured in the F_0 measurement. As an additional check, the normalized radiation patterns are plotted in Figure 5.22(b) at that frequency. The fact that the reflection coefficient was average at this frequency and the radiation patterns show no abnormalities further supports that the gain dip at 39 GHz is due to measurement effects.

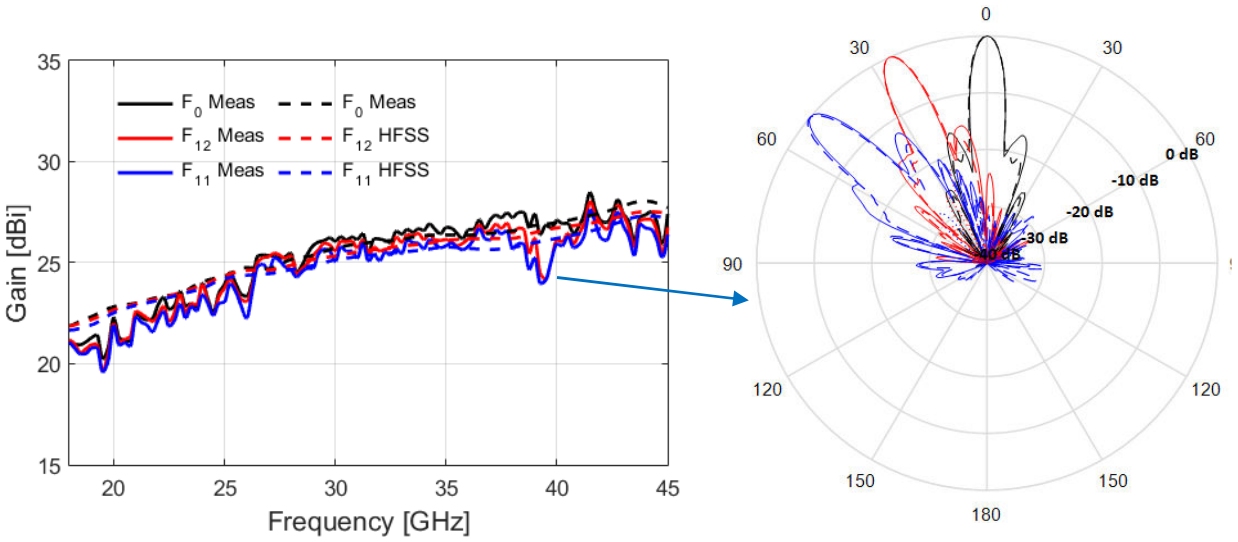

(a) (b)

Figure 5.22. (a) Gain of the three measured / simulated elements and (b) normalized E-plane radiation pattern corresponding with the dip at 39 GHz.

5.5 Analysis

5.5.1 Primary / Secondary Feed Patterns

Minimizing the PCV of the feed horn will minimize the LL's aperture phase error since the feed will be approximately focused across all frequencies. The amplitude distribution of the feed, however, will also have a direct impact on the LL radiation pattern. For this analysis, the feed's radiation will be referred to as the primary pattern and the LL's radiation the secondary pattern.

It can be noticed in the gain of the LL fed by horn 1 [Figure 5.9(b)] that the directivity peaks at about 40 GHz then drops about 1.5 dB over the next 5 GHz. Horn 2 / LL gain begins to drop at 44 GHz [Figure 5.22(a)] but is less obvious since it is near the maximum plotted frequency. It can also be seen in each configuration's corresponding HPBW plots that the E-plane HPBW begins to increase at the same frequency while the H-plane HPBW does not. This behavior is observed both in the simulations and the measurements.

For aperture antennas, the maximum directivity is related to the antenna's area A_{phys} by [14]

$$D = \frac{4\pi A_{phys} e_a}{\lambda^2} \tag{5.4}$$

where $e_a \leq 1$ is the aperture efficiency. For the LL, A_{phys} is simply the cross sectional area of the sphere. In the case of a reflector antenna, for example, an aperture efficiency of one occurs when its aperture is uniformly illuminated in terms of both amplitude and phase. The dependency on wavelength λ in the denominator of (5.4) describes an antenna's increase in directivity with frequency due to an increasing electrical size of the aperture. This is observed up to 40 GHz for horn1 / LL. At frequencies greater than 40 GHz, e_a begins decreasing with frequency by a factor greater than the increase caused by $1/\lambda^2$, causing an overall decrease in the directivity.

Two basic trends were observed in the 2-layer LL's peak sidelobe level (SLL) behavior: 1) The SLL worsened as frequency increased and 2) the feed's H-plane had worse sidelobes than in the E-plane at most frequencies. The latter effect can be explained with some analysis of the feed antenna pattern. An analysis conducted in [46] approximates the primary feed pattern as

$$P_f = \cos(\theta')^n \tag{5.5}$$

where θ' is the primary pattern angle and n describes the directivity of the feed. That is, a higher value of n corresponds with a narrower feed beamwidth incident on the LL. Assuming a feed with a pattern given in (5.5) and the geometry in Figure 5.23, the relationship between aperture plane power $P_a(r)$ and the feed's pattern is given by [47]

$$P_a(r) = \frac{\cos\left[\sin^{-1}\left(\frac{r}{f_p}\right)\right]^n}{f_p^2\sqrt{f_p^2 - r^2}}. \tag{5.6}$$

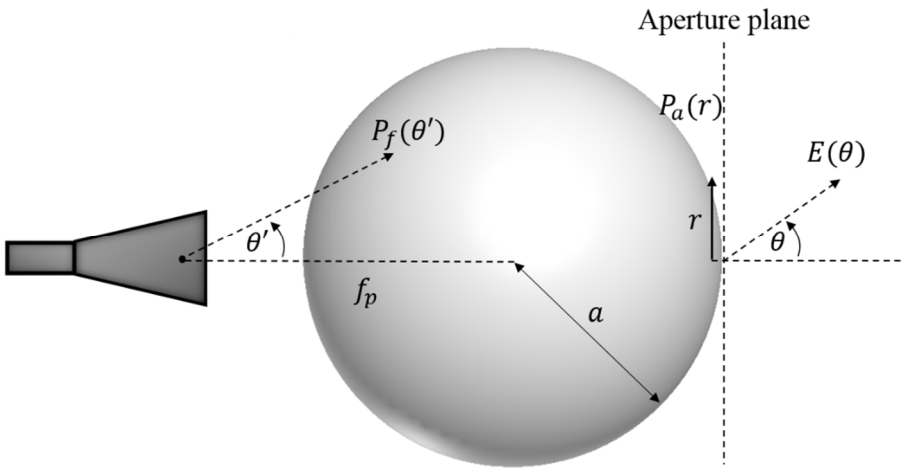

Figure 5.23. Geometry showing the LL aperture plane in relation to the primary and secondary radiation patterns.

The aperture illumination can be related to the far field by

$$E(\theta) = \int_0^1 \sqrt{P_a(r)}\, r\, J_0(k\, a \sin(\theta) r)\, dr \tag{5.7}$$

where J_0 is the zeroth order Bessel function of the first kind. Note that if the LL is uniformly illuminated, then $P_a(r)$ is constant and can be pulled out of the integral in (5.7). If $n > 1$, then the lens aperture will have a tapered power distribution and $P_a(r)$ will decrease as the normalized radius r approaches 1. The integration over the Bessel function J_0 describes where the sidelobes of the pattern will be located and is plotted in Figure 5.24. As the integration exceeds the second zero ($k\, a\, sin(\theta)\, r > 5.52$), the area under J_0 will begin to increase at off-boresight angles. A tapered $P_a(r)$, however, will mitigate the effect that the J_0 term has on the sidelobes.

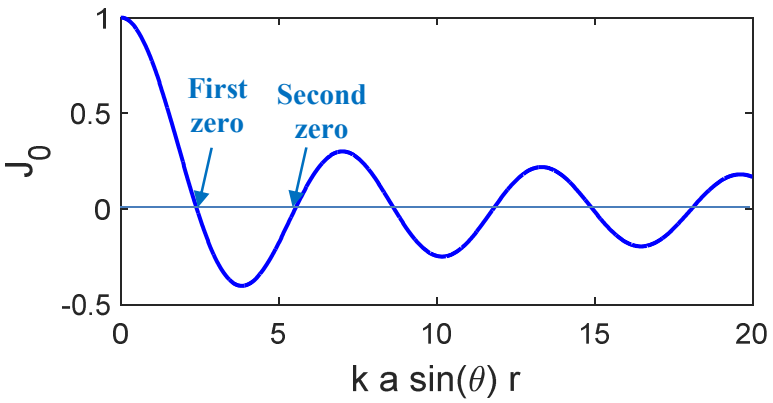

Figure 5.24. Zeroth Bessel function of the first kind.

In summary, the lens aperture plane $P_a(r)$ becomes more tapered as n increases and the primary feed directivity increases. Given the far field in (5.7), this leads to both a reduction in directivity and SLL of the secondary pattern. The feed / LL pattern relationship described does not take phase errors into account and assumes the PC to be located at the focal point. It does, however, explain the higher SLL in the H-plane, where the primary feed is wider in beamwidth for a square horn. This behavior can be seen in both the 2-layer and 10-layer lenses SLL plotted in Appendix C. Conversely, for an open-ended waveguide, the SLL is generally higher in the E-plane where the primary beamwidth is wider due to the smaller aperture dimension.

5.5.2 Horn Loss Analysis

The gain for horn 1 was simulated in HFSS using two different horn materials: 1) perfect electric conducting (PEC) material and 2) aluminum. The loss due to the finite conductivity of aluminum ($\sigma_{Al} = 3.8 \times 10^7$ S/m) was determined by comparison to the PEC horn and is plotted in Figure 5.25. Simulations were also completed with lower values of conductivity to reveal the loss's sensitivity with respect to σ.

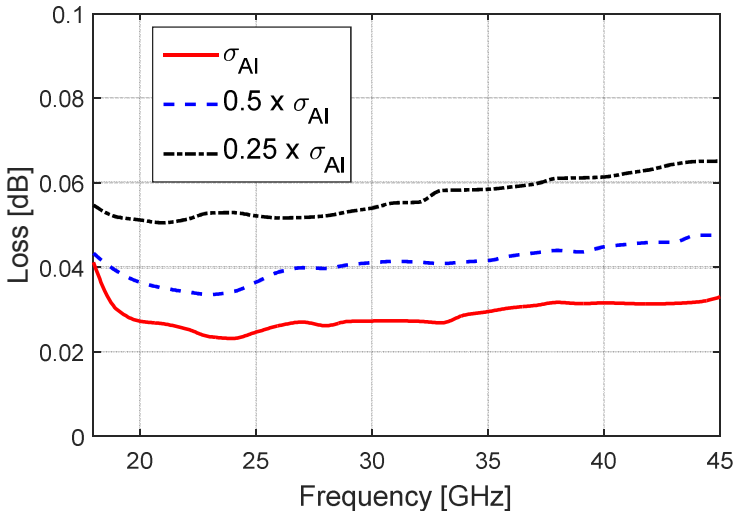

Figure 5.25. Horn 1 conductor loss due to the finite conductivity of aluminum, plotted for multiple values of σ.

The DMLS method contained a visible surface roughness, specified to be 5-15μm Ra[1]. As fields propagate through the horn, the surface roughness changes the path in which eddy currents will travel in the horn ridges and sidewalls depending on the skin depth δ relative to the roughness. Much interest has been given to the area of conductor loss over a rough surface. Morgan [48] solved this problem for square and triangular shaped grooves both parallel and transverse to the direction of current flow. Additional computations for expected conductor loss was provided and verified by rough surface modeling in HFSS [49]. For two-dimensional grooves transverse to current flow, increased conductor loss per unit length is given by

$$\frac{\alpha_c}{\alpha_{c0}} = 1 + \frac{2}{\pi}\tan^{-1}\left(1.4\left(\frac{\Delta}{\delta}\right)^2\right) \tag{5.8}$$

α_c = Attenuation constant with surface roughness

α_{c0} = Attenuation constant for smooth surface

Δ = RMS roughness value

δ = Skin depth

[1] Ra is a metric used to describe surface roughness. It is the arithmetic average of surface height deviation.

The term Δ/δ represents a normalized RMS roughness that corresponds to the groove shape. For a rectangular groove, $\Delta = h/p\sqrt{w(p-w)}$ referring to Figure 5.26.

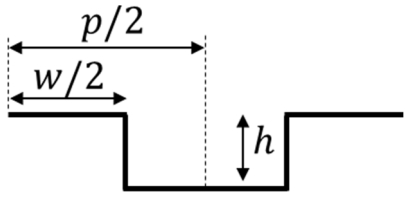

Figure 5.26. Two-dimensional rectangular groove dimensions.

Because this method for computing conductor loss assumes that the path distance can at most double due to the induced grooves, the roughness attenuation in (5.8) asymptotically approaches 2 as δ decreases at rising frequencies. As the skin depth becomes infinitely small, the eddy currents simply travel the exact outline of the surface roughness, whereas at lower frequencies the skin depth is sufficiently large such that the current can flow beneath the rough surface in a more direct path. For square grooves of varying roughness, the attenuation ratio is plotted in Figure 5.27.

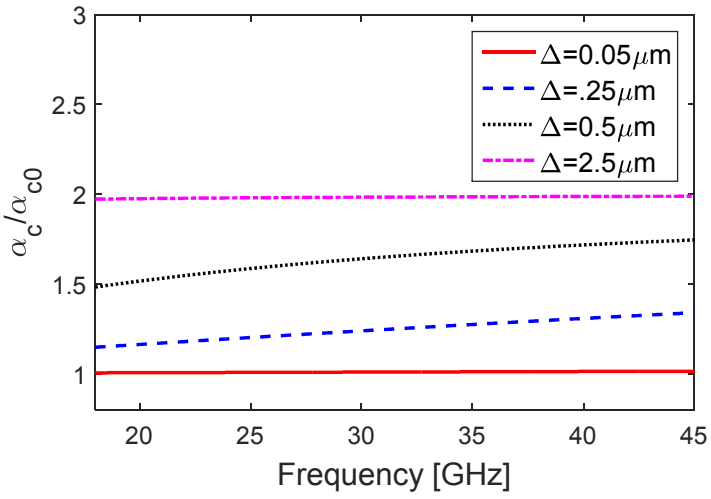

Figure 5.27. Attenuation constant ratio for various square groove roughnesses.

The skin depth for aluminum over 18-45 GHz varies from about 0.4 – 0.6 μm and it can be seen that as the roughness Δ enters this range the surface attenuation is expected to rise. Assuming a worst case Δ of 15μm, the surface roughness loss will reach the asymptotic limit of 2 across the frequency band. Even though the DMLS surface resembles a periodic structure whose behavior, based on the model, would resemble that of Figure 5.27, a safety factor of $\alpha_c/\alpha_{c0} = 4$ will be used herein since exact surface properties are unknown. In addition, a second safety factor will be used for the assumed conductivity, in which the loss computed with $\sigma = 0.5 \times \sigma_{Al}$ in Figure 5.25 yielded a maximum of about 0.05 dB. Multiplying by a surface roughness attenuation factor of 4, a maximum surface loss of 0.2 dB is expected due to the combined surface roughness and limited conductivity of the horn surface.

5.5.3 2-Layer Lens Loss Analysis

Using the loss tangents $\tan\delta_i$ of the inner and outer LL layers given in [33], the loss was computed for the 2-layer LL when fed by horn 1 in HFSS by comparison with the gain for the lossless lens. Multiples of $\tan\delta_i$ were also applied to the lens and plotted in Figure 5.28 as a means for showing the sensitivity of the material properties in terms of the loss tangent.

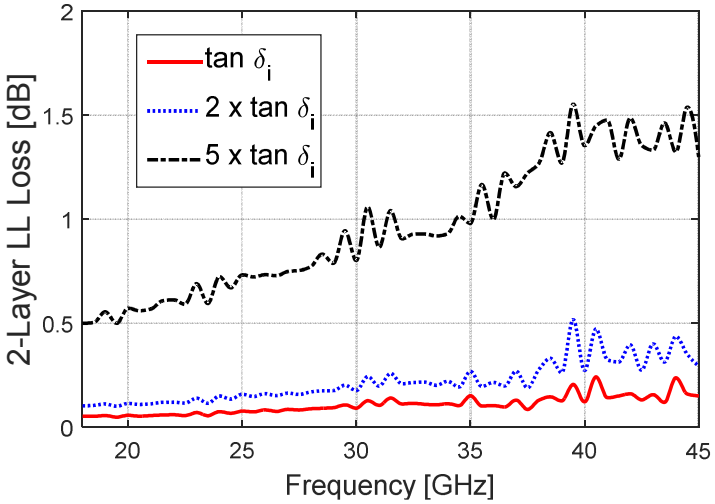

Figure 5.28. Loss of the 2-layer LL fed by horn 1, where tan δ_i is the assumed loss tangent of the LL layer materials.

For the given loss tangents of the materials, a maximum of 0.24 dB loss was observed. Doubling the loss tangents in each material results in a maximum loss of 0.52 dB. Due to uncertainties in the materials, the loss tangent's frequency dependency, and on disagreement within the literature on the material properties, a maximum of 0.52 dB loss will be assumed for the 2-layer LL, where a factor of 2 was used in the loss tangents to account for any such errors that may exist. For a high power application, the difference between 0.24 dB and 0.52 dB of loss can translate into a significant amount of heat and a more thorough study of the material properties may be needed to determine the power handling capabilities of the lens.

5.6 Summary

Both feed antennas were positioned under the LL according to metrics that were developed to optimize the system's radiation characteristics in terms of directivity and SLL over the frequency band. Each configuration was measured and results were confirmed to closely resemble the radiation patterns given in HFSS, establishing confidence in the described methods for simulating, mounting, and measuring the lens / feed system. Nine feeds of the second prototype design were implemented into two curvilinear arrays and S-parameters of the numerous feeds were measured. Although no obvious excessive losses due to the surface roughness of the DMLS aluminum fabrication method were observed, an additional analysis was completed which predicts a worst case of 0.2 dB loss, although this value could be more effectively determined (and likely reduced) if a more complete set of surface statistics were known. Similarly, a maximum LL loss of 0.52 dB has been given through simulations with the assumption that the loss tangent is at most double the values given in literature at the simulated frequencies.

Chapter 6

Conclusions

6.1 Phase Center of Horn Antennas

Chapter 2 discussed several methods for computing the PC of any antenna radiating a well-defined main lobe in the boresight direction. As a design specification that is very qualitative in nature, it is important to understand the implications of the different factors affecting the computation of PC. The beamwidth and choice of weighting function are two of the main aspects affecting its computation, but other subjective qualities may be necessary to yield results that are of interest for the given application. For example, while testing horn 2 which had a wider beamwidth than the first horn, it was realized that spillover portions (i.e. edges of the 10 dB beamwidth that do not intersect the lens) of the beam were being used in the PC computation at low frequencies. It was decided that it was more rational to limit the far field to angles of the pattern that are within the subtended angle of the lens, about 122° at the mounting distance that was used.

The simulation of four example horn antennas showed some general tendencies of the PC in horn antennas and how its definition can have a large impact in its determined location. Although at the time of the feed antenna designs it was not well-understood how important PC stabilization would be for performance of the LL, the examples nonetheless were a motivation for the design of an antenna whose PC remained as stable as possible across frequency. To avoid losing the distinction between E and H plane PCs, they were plotted separately throughout this thesis. The averaging of the two surely would

have lowered the PCV of any designed antennas and may have looked better on paper, but generalizing the PC in this sense can be deceiving in that a horn with a zero PCV could still have E and H-plane PCs far apart from one another and thus the lens aperture phase error would not be minimized. If an averaged E/H-plane PC had been used, a separate metric indicating the separation between E and H PCs would have also been included.

6.2 Design of a Luneburg Lens Feed

After exploring several PC stabilization methods, the horn interior ridges were designed with a $\sin^2$ profile and the PC was stabilized to less than 2 mm over the 18 – 45 GHz frequency range in the first design iteration, prototype horn 1. This design was fabricated with aluminum using both subtractive and additive techniques and similar performance was seen between both prototype implementations. Mounting a single feed under the LL, it was shown that models of the LL in HFSS produced accurate performance results in terms of reflection coefficient, directivity, and radiation patterns. In most cases, sidelobes were higher in the measurements by 1-2 dB. Measurements, however, are subject to finite accuracy in the feed / LL spacing, fabrication imperfections, and misalignment error therefore it should not be surprising that the modeled results appear slightly better.

A second design horn comprising a smaller aperture was designed for mounting in a LL feed manifold in its lower half-space. Both the smaller aperture and lessons learned from the parametric sweep conducted in the first iteration helped reduce the PCV to 1.5 mm in the E-plane and 0.8 mm in the H-plane while maintaining closer E/H PCs at each frequency. Although the PC measurements yielded overall less agreement with simulations for horn 2, its performance as measured with the LL supports a lower PCV as compared to horn 1. With nine feeds installed into the lens manifold, three of the feeds in the E-plane array were measured and compared with the HFSS simulation. Like in horn 1, higher sidelobes were seen in the measured radiation patterns.

6.3 Future Work

From the beginning of this project, the top priority concerning the feed antenna involved minimizing its PCV with the assumption that the LL focal point was stable. With a maximum PCV of 1.5 mm, near-maximum directivity (within 0.5 dB) was achieved across all frequencies as determined when sweeping horn 2 in distance from the lens surface in HFSS. It was seen that the sidelobe level, however, was more sensitive to the horn positioning. It may be worthwhile in the future to attempt to design a varying PC that coincides with movement of the LL focal point to further minimize the peak SLL across all frequencies. In addition, as the 2-layer LL becomes better understood it may be beneficial to prioritize other feed characteristics before stabilizing the PC, such as fine control of the feed beamwidth and thus the LL illumination and aperture efficiency.

While only nine feeds were mounted in the LL manifold, eventually 36 such feeds will be required to span the bottom hemisphere of the lens. The positioning of curvilinear arrays across a spherical surface is simple, however equally spacing 36 elements to maximize beam coverage is a much more complicated task as there is no obvious way in which to organize them. Even with their spacing optimized, the beamwidth of the LL may be too narrow to allow for continuous coverage at higher frequencies and it may be necessary to limit the directivity of the feed / LL combination if beam overlapping is desired at, for example, the 3 dB beamwidths. With each of the 36 elements requiring dual-pol operation, 36 orthomode transducers (OMTs) must also fit into the lower hemisphere of the lens. The mechanical design in itself of the end product will be very challenging.

In addition to the lens considered in this research, alternative lens options may provide improved radiation characteristics. A LL consisting of additional layers may help to reduce sidelobes while mitigating the reflections at layer boundaries. With today's 3D-printing capabilities, printing a LL with precise control of air-to-plastic ratio (and thus permittivity) may also be a conceivable method for producing a LL if internal losses can be kept to a minimum.

6.4 Original Contributions

The following original contributions of this thesis are listed below:

- Demonstrated a method for stabilizing the PC of a square horn antenna over a wide bandwidth, where corrugations were not a practical design option.
- Implemented an alternative method for computing the PC for an antenna whose PC is not located sufficiently close to the center of rotation of a roll-over-azimuth positioner. This was done iteratively to avoid using approximations that can lead to large errors at millimeter wavelengths.
- Designed a manifold consisting of two curvilinear arrays of feed horn antennas for a LL whose design focal point is 5 mm from its surface. Each feed horn can be adjusted approximately ± 2 mm relative to the lens surface and a method for setting the lens / horn spacing was demonstrated using a spacer constructed of two pieces of acrylic.
- Fabricated a small horn antenna using aluminum direct metal laser sintering and demonstrated that results similar to previously proven fabrication methods were obtainable with modest losses.

Bibliography

[1] J. L. Volakis, Antenna Engineering Handbook, New York: McGraw-Hill, 2007.

[2] R. K. Luneburg, The Mathematical Theory of Optics, Providence, RI: Brown Univ. Press, 1944.

[3] F. T. Ulaby and D. G. Long, Microwave Radar and Radiometric Remote Sensing, Ann Arbor: The Univ. of Michigan Press, 2014.

[4] P. Afanasyev, S. Matitsine, V. Sledkov, P. Lagoiski, L. Matytsine, T. DeMarco, and T. Chia, "Multi-beam Luneburg Lens Antenna for Cellular Communications," in *EuCAP*, Lisbon, 2015.

[5] J. Thorton, D. Smith, S. J. Foti, and Y. Y. Jiang, "Reduced Height Luneburg Lens Antennas for Satellite Communications-on-the-move," in *COMITE*, Pardubice, 2015.

[6] J. A. Lock, "Scattering of an Electromagnetic Plane Wave by a Luneburg Lens. I. Ray Theory," *Journal of the Optical Society of America,* vol. 25, pp. 2971-2979, 2008.

[7] J. Reinholdt, "Cylindrical Luneburg Lens Antenna for Multi-Beam Small Cell Wireless Backhaul Applications," M.Sc. Thesis, Dept. of Eng. Physics and Elec. Eng., Lulea Univ. of Tech., 2014.

[8] S. Rondineau, M. Himdi, and Jacques Sorieux, "A Sliced Spherical Luneburg Lens," *IEEE Antennas Wireless Propag. Lett.,* vol. 2, pp. 163-166, 2003.

[9] A. V. Boriskin, A. Vorobyov, and R. Sauleau, "Two-Shell Radially Symmetric Dielectric Lenses as Low-Cost Analogs of the Luneburg Lens," *IEEE Trans. Antennas Propag.,* vol. 59, no. 8, pp. 3089-3093, 2011.

[10] H. Mosallaei and Y. Rahmat-Samii, "Nonuniform Luneburg and Two-Shell Lens Antennas: Radiation Characteristics and Deisgn Optimization," *IEEE Trans. Antennas Propag.,* vol. 49, no. 1, pp. 60-69, 2001.

[11] M. Liang, X. Yu, R. Sabory-Garcia, W. Ng, M. E. Gehm, and H. Xin, "Broadband Electronically Beam Scanning Structure Using Luneburg Lens," in *MTT-S Int. Microwave Symp.*, 2013.

[12] Q. Xu and J. Thorton, "Report on Steerable Antenna Architectures and Critical RF Circuits Performance," CAPANINA, 2006.

[13] M. J. Goonan, "A novel Luneburg lens feed for multiple beam antennas," in *Antennas and Propag. Soc. Int. Symposium*, Ann Arbor, MI, 1993.

[14] C. Balanis, Antenna Theory, 3rd Ed., Hoboken, NJ: John Wiley & Sons, Inc., 2005.

[15] W. L. Barrow and L. J. Chu, "Theory of the Electromagnetic Horn," *Proc. IRE,* pp. 51-64, 1939.

[16] G. C. Southworth, "Hyper frequency wave guides - General considerations and experimental results," *Bell Syst. Tech. J.,* vol. 15, pp. 284-309, 1936.

[17] W. T. Slayton, "Design and Calibration of Microwave Antenna Gain Standards," US Naval Research Lab, Washington, DC, 1954.

[18] E. H. Braun, "Gain of Electromagnetic Horns," *Proc. IRE,* vol. 41, pp. 109-115, 1953.

[19] E. H. Braun, "Some Data for the Design of Electromagnetic Horns," *IEEE Trans. Antennas Proagat.,* Vols. AP-4, pp. 29-31, 1956.

[20] HFSS v.15.0, *ANSYS, Inc.,* 2015.

[21] *IEEE Standard for Definitions of Terms for Antennas,* New York, NY, 2013.

[22] M. J. Radway, T. P. Cencich, and D. S. Filipovic, "Phase Center Stability of Planar Spiral Antennas," in *Antenna Applications Symposium*, Monticello, IL, 2009.

[23] S. R. Best, "Distance-Measurement Error Associated with Antenna Phase-Center Displacement in Time-Reference Radio Positioning Systems," *IEEE Antennas Propagat. Mag.,* vol. 46, no. 2, pp. 13-22, 2004.

[24] T. Wei and Z. Xin, "Research on the High Precise Calibration of the GPS Receiving Antenna Phase Center," in *ISAPE*, Guangzhou, 2010.

[25] J. Friden and G. Kristensson, "Calculation of Antenna Radiation Center Using Angular Momentum," *IEEE Trans. Antennas Propag.,* vol. 61, no. 12, pp. 5923-5930, 2013.

[26] P. Kildal, "Combined E- and H-Plane Phase Centers of Antenna Feeds," *IEEE Trans. Antennas Propag.,* Vols. AP-31, no. 1, 1983.

[27] E. I. Muehldorf, "The Phase Center of Horn Antennas," *IEEE Trans. Antennas Propag.,* Vols. AP-22, pp. 753-750, 1970.

[28] Y. Y. Hu, "A Method of Determining PHase Centers and its Application to Electromagnetic Horns," *Journal of the Franklin Institute,* vol. 271, no. 1, pp. 31-39, 1961.

[29] W. Kunysz, "Antenna Phase Center Effects and Measurements in GNSS Ranging Applications," in *ANTEM-AMEREM*, Ottawa, ON, 2010.

[30] W. V. T. Rusch and P. D. Potter, Analysis of Reflector Antennas, New York: Academic Press, Inc., 1970.

[31] P. N. Betjes, "An Algorithm for Automated Phase Center Determination and its Implementation," in *AMTA*, St. Louis, 2007.

[32] W. H. Press, S. A. Teukolsky, W. T. Vetterling, B. P. Flannery, Numerical Recipes, The Art of Scientific Computing, 3rd ed., Cambridge, MA: Cambridge Univ. Press, 2007.

[33] D. M. Pozar, Microwave Engineering, 3rd Ed., John Wiley & Sons, Inc., 2005.

[34] M. Teichman, "Determination of Horn Antenna Phase Centers by Edge Diffraction Theory," *IEEE Trans. Aerosp. Elecron. Syst.,* Vols. AES-9, no. 6, pp. 875-882, 1973.

[35] C. Ehrenborg, *Investigation and Comparison Between Radiation and Phase Center for Canonical Antennas,* M.Sc. Thesis: Dept of Elec. and Info. Tech., Lund Univ. 2014..

[36] FEKO Suite 6.2, *EM Software & Systems S.A. Ltd,* 2013.

[37] K. Harima, "Accurate Gain Measurement for Millimeter-Wave Horn and Open-Ended Waveguide Antennas," in *Int. Symp. on Antennas and Prop.*, Nagoya, Japan, 2012.

[38] N. Jastram and D. S. Filipovic, "Development of Integrated High Power Passive Front-Ends for Towed Decoys," in *GOMACTech 15*, St. Louis, 2015.

[39] A. D. Olver, P. J. B. Clarricoats, A. A. Kishk, and L. Shafai, Microwave Horns and Feeds, New York: IEEE Press, 1994.

[40] P. Kildal, "Artificially soft and hard surfaces in electromagnetics and their application to antenna design," in *Microwave Conf. Proc*, Madrid, Spain, 1993.

[41] K. L. Walton and V. C. Sundberg, "Broadband Ridged Horn Design," *Microwave Journal,* vol. 7, pp. 96-101, 1964.

[42] S. B. Cohn, "Flare-Angle Changes in a Horn as a Means of Pattern Control," *Microwave Journal,* vol. 13, pp. 41-46, 1970.

[43] A. X. a. J. Olver, "Design of Profiled Corrugated Horns," *IEEE Trans. Antennas Propag.,* vol. 36, no. 7, 1988.

[44] A. H. Akgiray, "New Technologies Driving Decade-Bandwidth Radio Astronomy," Ph.D. dissertation, California Inst. of Tech., Pasadena, CA, 2013.

[45] ANSYS, "HFSS Online Help," 2012.

[46] J. Thorton, "Properties of Spherical Lens Antennas for High Altitude Platform Communications," in *EMPS/ASMS*, Noordwijk, 2004.

[47] S. P. Morgan, "General Solution to the Luneburg Lens Problem," *Journal of Applied Physics,* vol. 29, no. 9, pp. 1358-1368, 1958.

[48] S. P. Morgan, Jr., "Effect of Surface Roughess on Eddy Current Losses at Microwave Frequencies," Bell Telephone Laboratories, Murray Hill, NJ, 1948.

[49] M. V. Lukic and D. S. Filipovic, "Modeling of 3-D Surface Roughness Effects with Application to u-Coaxial Lines," *IEEE Trans. Microw. Theory Techn.,* vol. 55, no. 3, pp. 518-525, 2007.

[50] P. A. Beeckman, "Analysis of phase errors in antenna-measurements applications to phase-pattern

corrections and phase-centre determination," *IRE Proceedings,* vol. 132, no. 6, pp. 391-394, 1985.

[51] P. I. Deffenbaugh, R. C. Rumpf, and K. H. Church, "Broadband Microwave Frequency Characterization of 3D Printed Materials," *IEEE Trans. Compon. Packag. Manuf. Technol.,* vol. 3, no. 12, pp. 2147-2155, 2013.

[52] Z. Sipus, D. Bojanjac, and T. Komljenovic, "Electromagnetic Modeling of Spherically Stratified Lenses Illuminated by Arbitrary Sources," *IEEE Trans. Antennas Propag.,* vol. 63, no. 4, pp. 1837-1843, 2015.

Appendix A

Phase Center Measurements

When using a CEM (computational electromagnetic) simulation tool to obtain the far field phase of a horn antenna, phase symmetry about the z-axis is easily maintained to within 0.5 degrees when using reasonable solution settings. Because HFSS projects the far field to $r \to \infty$, the approximation given in (2.4) remains very accurate and any of the PC extraction methods discussed in Chapter 2 will yield practically the same values for the PC offset d. When taking measured data, however, care must be taken to consider the effects of the finite far field distance in which the measurements are taking place.

A.1 Rotational Scanning Error

In the ideal case, the antenna under test (AUT) is mounted with its PC located on the axis containing the center of rotation ($d = 0$), corresponding to Figure A.1. In some cases, however, the size of the AUT or other mounting limitations may require an antenna to be located a distance from the center of rotation. Referring to Figure A.1, it is evident that the farther the AUT is from the center of rotation, the greater distance it will physically move in the antenna range as it scans in θ.

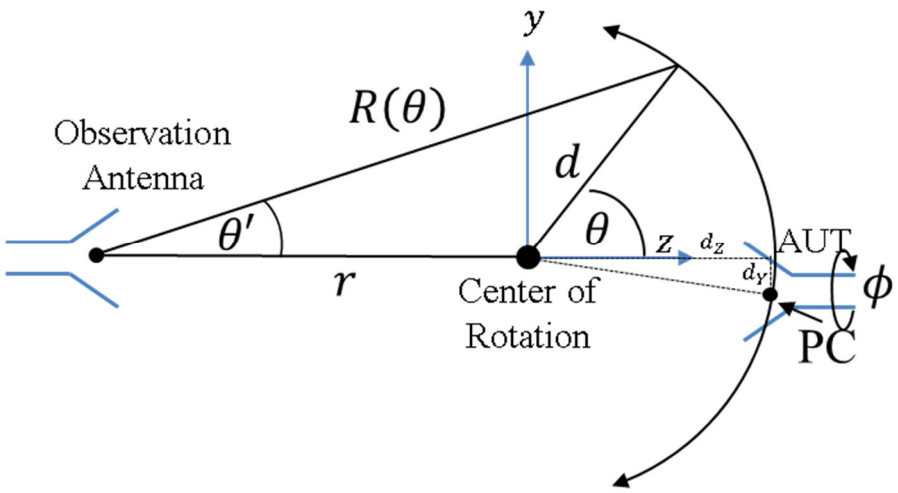

Figure A.1. Antenna range setup geometry, where d_Y and d_Z refer to the PC position when the AUT is positioned at $\theta = 0$.

While this simple fact is often disregarded when taking more common amplitude-based measurements, it can have a significant impact in the PC computation due to the rotational phase error incurred when scanning the AUT in θ [50]. During the first set of measurements completed with horn 1, the aperture of the AUT was mounted a distance of 13.5 cm from the center of rotation, i.e. d~13.5 cm. In this case, it was discovered that unlike CEM simulations, the method used to extract the PC can have a significant impact on the values obtained. In the antenna range geometry shown in Figure A.1, the wideband observation antenna was set up such that $r = 2.2$ m and d/r~0.06. Evaluating the true value of $R(\theta)$ using the law of cosines:

$$R(\theta) = \sqrt{r^2 + d^2 + 2rd\cos(\theta)}. \tag{A.1}$$

The approximation for $d \ll r$ is

$$\hat{R}(\theta) \cong r + d\cos(\theta). \tag{A.2}$$

With respect to the horn 1 measurement setup, the deviation between (A.1) and (A.2) is

$$\Delta R = \left| R(\theta) - \hat{R}(\theta) \right| \tag{A.3}$$

and is plotted in Figure A.2.

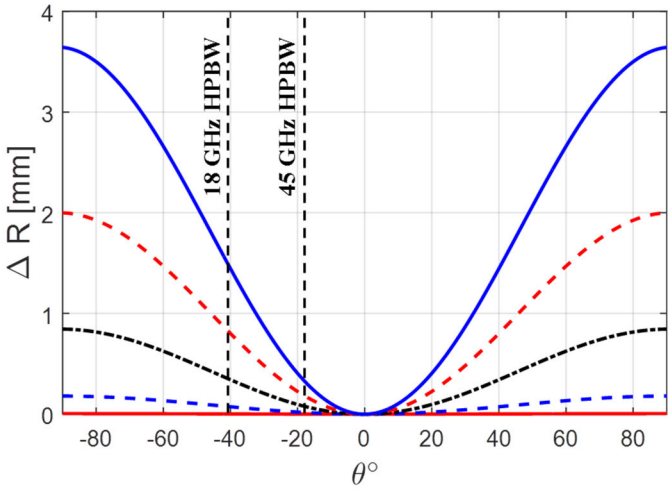

Figure A.2. Distance error given in (A.3).

When $d = 13.5$ cm, this corresponds with a 31° phase error at 18 GHz and 18° phase error at 45 GHz at each respective 3 dB beamwidth, causing about a 7 mm offset in PC computation, a significant distance at millimeter wavelengths. In this case, the phase error is greater at the low frequency simply because the beamwidth is wider despite the longer wavelength and lower wavenumber.

In order to prevent rotational phase error from corrupting PC measurements, the PC of the AUT should be mounted as close to the center of rotation as possible. If this cannot be done due to mounting restrictions, then a method such as the one given in section 2.4 should be implemented which considers the distance r in an iterative PC computation. The rotational phase error's effect on the PC measurement is shown in Figure A.3, where it can be seen that solving for PC using the iterative method resolves the offset.

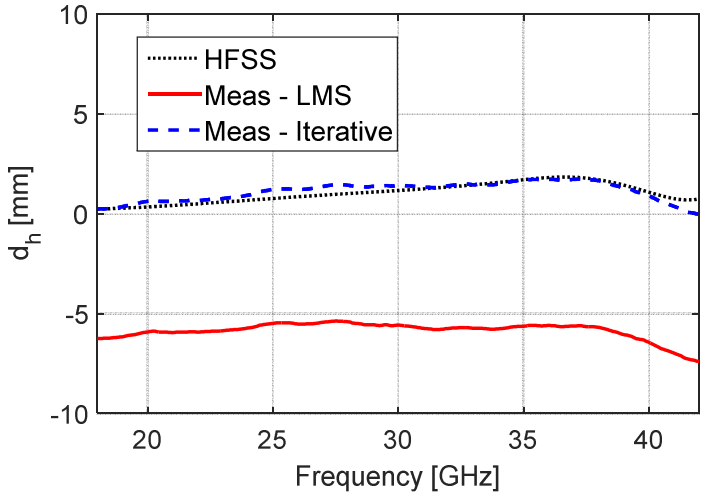

Figure A.3. E-plane PC measurement of horn 1 mounted 13.5 cm from the center of rotation, computed using the least mean squares error (red solid) which is susceptible to the rotational phase error versus the iterative method (blue dashed) which corrects for the error.

While r generally can only be approximated since its true measurement is relative to the observation antenna's PC which can also vary with frequency and scan angle θ', r determined to within 1 cm was easily obtained which will determine the PC to within 0.3 mm for the given mounting setup of $d = 13.5$ cm. However, as d increases the computation becomes more sensitive to the measurement of r, therefore it is always good practice to minimize d when mounting the AUT regardless of the method used.

Appendix B

Lens / Feed Mounting

The LL was constructed using a solid core and outer shell of different indices of refraction. Because of a very thin layer of glue adhering the two halves of the outer shell, a small indent of less than 0.5 mm circles the lens equator. A small ring was placed around the lens bracket to grip the lens in the indent. This was advantageous in that if the lens were a perfect sphere without an indent, the bracket would likely have needed to be wider to ensure the lens did not slip out during measurements. Both the indent and mating ring are pictured in Figure B.1.

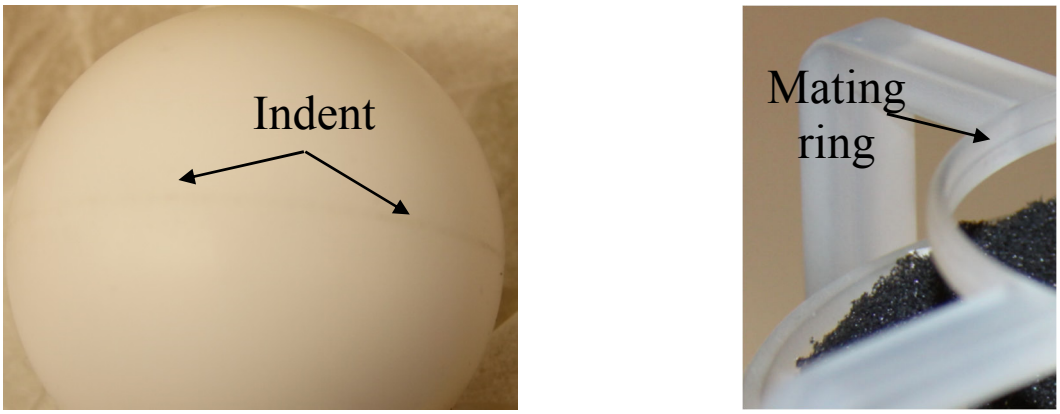

(a) (b)

Figure B.1. (a) Indent on the equator of the LL and (b) mating ring designed onto the lens bracket.

B.1 Materials

The material of the 3D-printed mounting bracket and manifold was chosen mainly for its electrical properties. Somos Watershed 11122 was used which has a dielectric constant of 2.6 and loss

tangent of 0.027 at the highest measured frequency of 11 GHz in [51]. Mechanically, a polypropylene or true ABS plastic would be more durable but the available types had higher loss tangents.

Before printing the horn 1 single feed mount bracket, an HFSS simulation was run with and without the bracket as shown in Figure B.2. The bracket was assumed to be ABS-like with $\epsilon_r = 3$ and the two screws were modeled as nylon with $\epsilon_r = 4$.

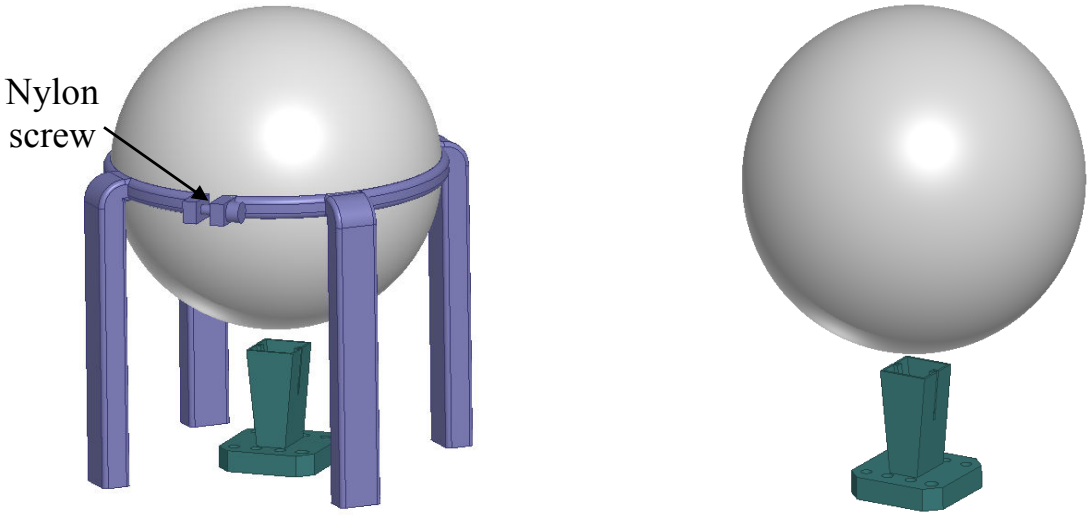

(a) (b)

Figure B.2. Horn 1 (alternate exterior design) simulated (a) with bracket in place and (b) without bracket.

Normalized radiation patterns are plotted in Figure B.3 for comparison of sidelobe performance with and without the lens mounting bracket. As expected, the mounting brackets have no discernable impact on the 45 GHz antenna pattern since both the feed and lens beamwidths are narrow at the high frequency. At 18 GHz, however, the fields are more spread and there is more interaction with the bracket. The 18 GHz E-plane far sidelobes (> 45 °) are seen to be higher by 2-4 dB, while the first and second H-plane sidelobes are raised by about 1 dB.

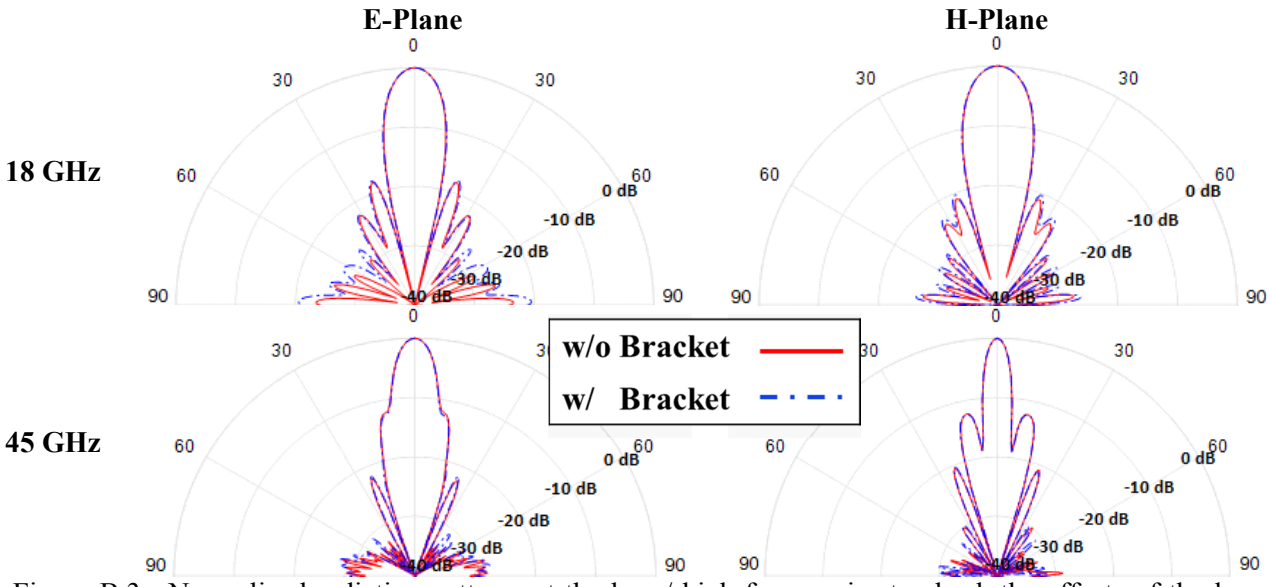

Figure B.3. Normalized radiation patterns at the low / high frequencies to check the effects of the lens mounting bracket.

B.2 Feed Horn Positioning

The feed horns were designed to slide up and down in their mounting brackets by ± 2 mm, allowing for accurate placement of the feeds with respect to the lens surface even in the presence of small fabrication errors. One difficult task when populating the feed array was spacing the hollow horn apertures to the curved spherical surface of the lens. To accomplish this to a reasonable level of accuracy, a fixed spacer was created for the desired aperture to lens surface distance. A small piece of acrylic was cut such that it fit over on the horn aperture, with additional pieces on three of the sides to keep it from sliding off. A nylon screw was then threaded and glued into the top and filed down until the desired distance was obtained as measured using a digital caliper [Figure B.4(a)]. The horn position could then be set and tightened with the spacer in place [Figure B.4(b)]. Once the horn was secured using the nylon set screws, the spacer was then slid out.

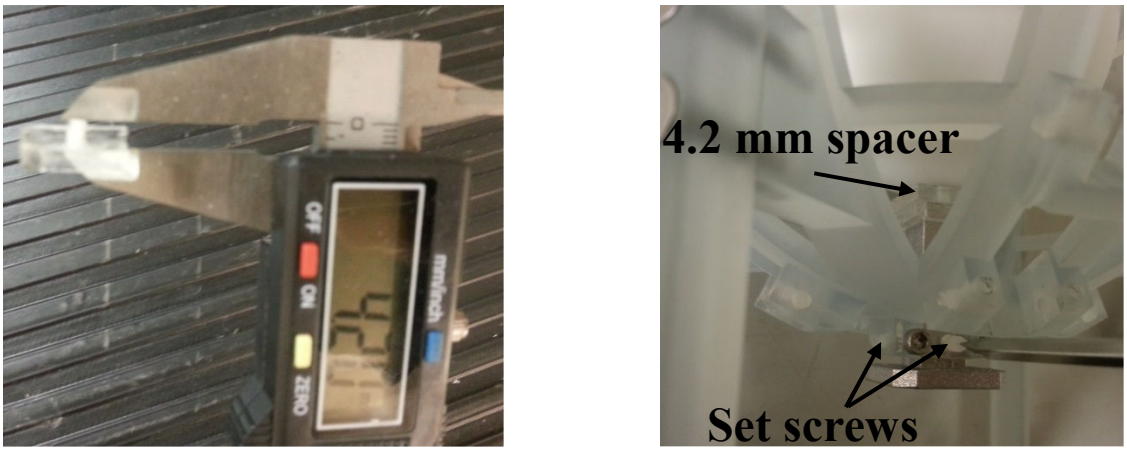

(a) (b)

Figure B.4. (a) Measurement of the horn/lens spacer and (b) alignment of the F_0 feed antenna.

To populate the array, it is required to install the feed elements starting with the center element (F_0) and work outward in order to be able to access the three set screws for each element.

Appendix C

10-Layer LL Simulation

A 10-layer LL was modeled in HFSS as a means for comparing performance of the 2-layer LL (Figure C.1). The 10-layer LL is a much closer approximation to an ideal uniform LL than is the 2-layer and their direct comparison can help to recognize certain effects caused by the 2-layer construction type.

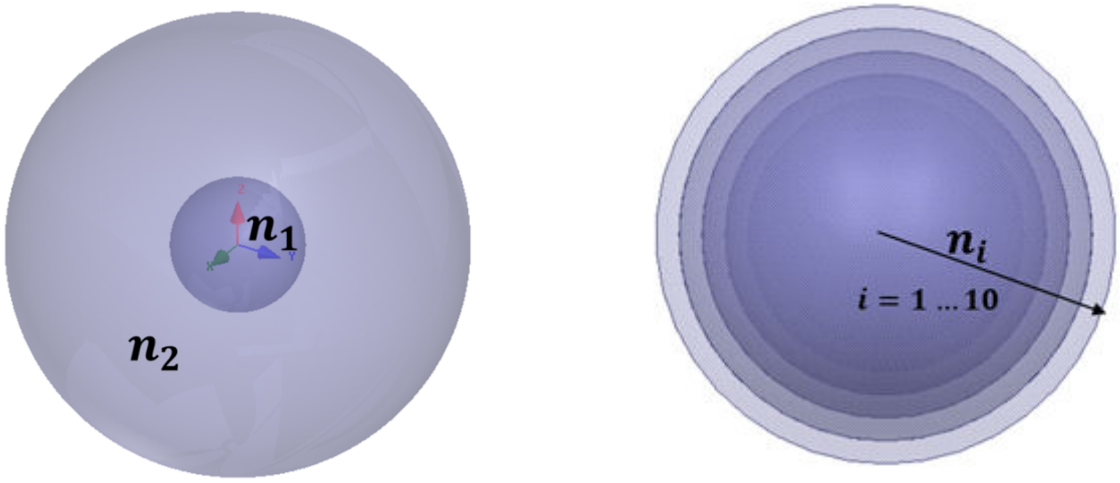

(a) (b)

Figure C.1. Models of the (a) 2-layer LL and (b) 10-layer LLs.

C.1 E-Fields – Horn 1

The following plots show the E-fields resulting from the 2 and 10-layer LLs excited with horn 1 at various frequencies. The E-fields are plotted in log scale (Figure C.2), normalized to the E-field intensity at the feed aperture.

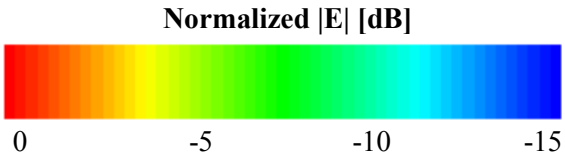

Figure C.2. Scale used in Table C.1 through Table C.6.

Table C.1. Horn 1 / LL fields at 18 GHz.

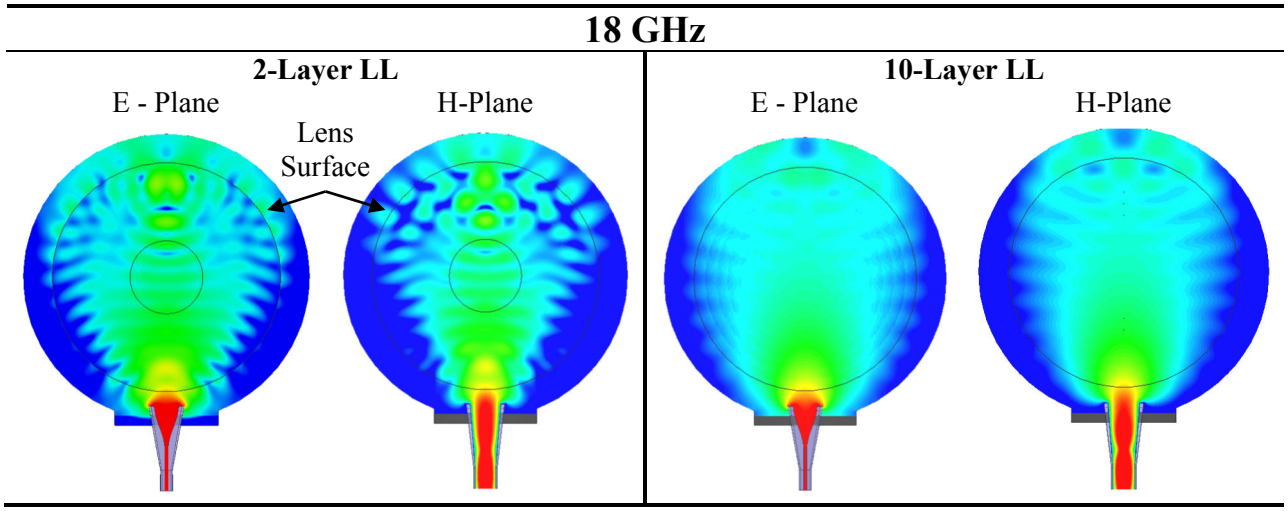

Table C.2. Horn 1 / LL fields at 23 GHz.

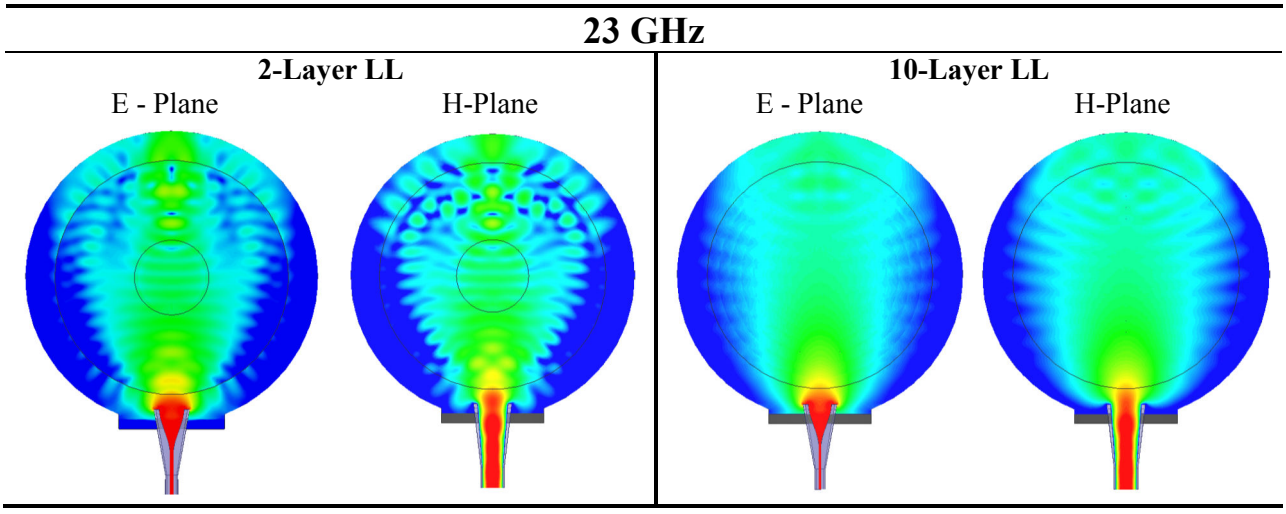

Table C.3. Horn 1 / LL fields at 27 GHz.

27 GHz			
2-Layer LL		**10-Layer LL**	
E - Plane	H-Plane	E - Plane	H-Plane
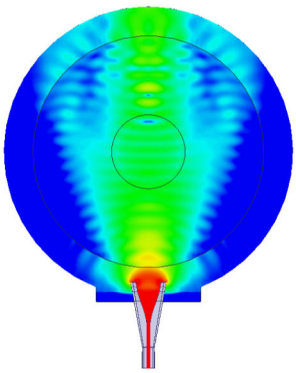	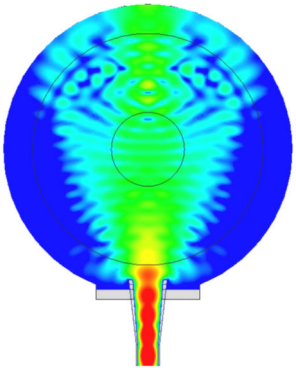	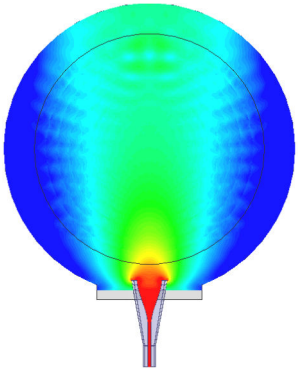	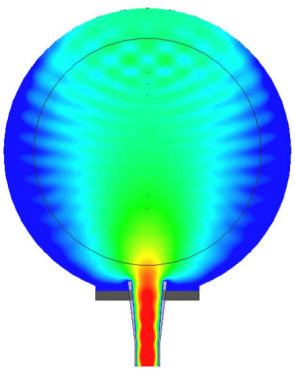

Table C.4. Horn 1 / LL fields at 33 GHz.

33 GHz			
2-Layer LL		**10-Layer LL**	
E - Plane	H-Plane	E - Plane	H-Plane
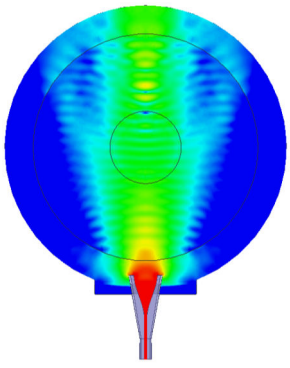	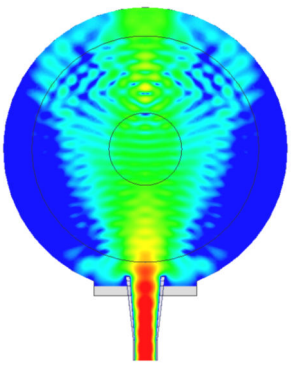	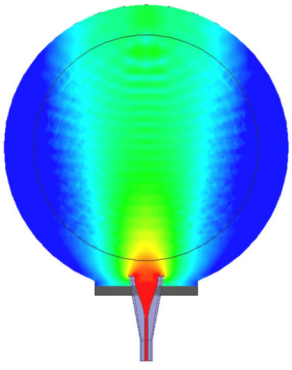	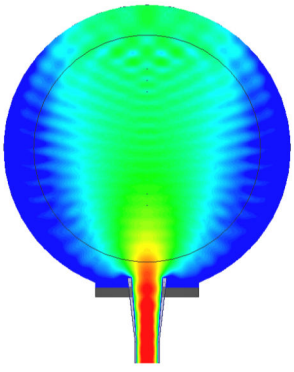

Table C.5. Horn 1 / LL fields at 40 GHz.

40 GHz			
2-Layer LL		**10-Layer LL**	
E - Plane	H-Plane	E - Plane	H-Plane
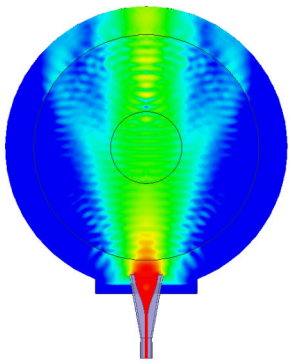	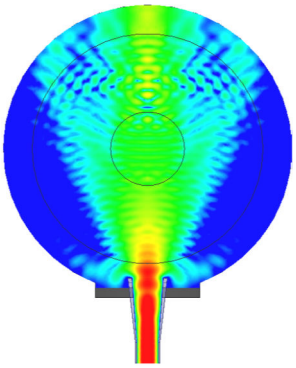	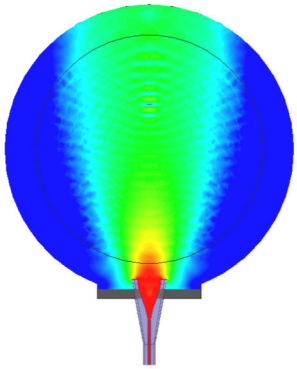	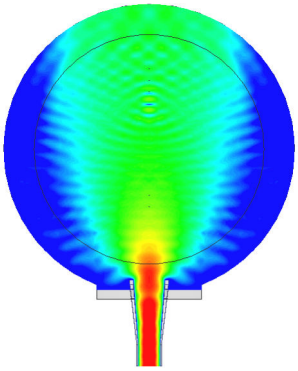

Table C.6. Horn 1 / LL fields at 45 GHz.

45 GHz			
2-Layer LL		**10-Layer LL**	
E - Plane	H-Plane	E - Plane	H-Plane
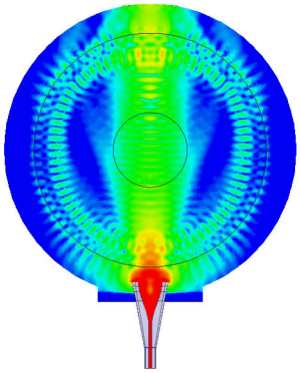	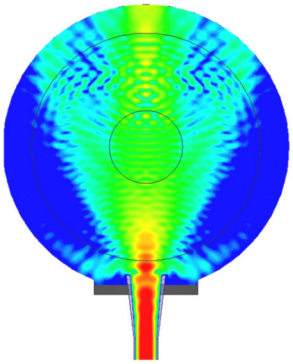	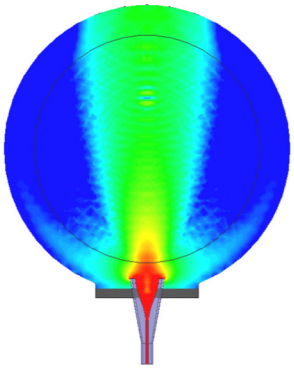	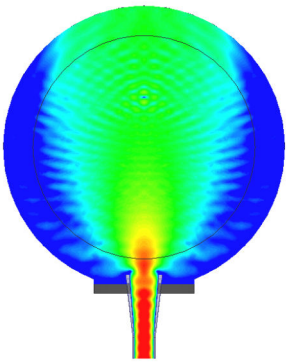

A decreasing illumination area with frequency is apparent in both lenses due to the increasing directivity of the feed antenna, particularly in the E-plane. The 2-layer LL also appears to have an extra mode excited close to its surface at 45 GHz and it was not clear as to whether this was causing a drop in the directivity. The directivities of both 2 and 10-layer lenses are plotted in Figure C.3(a), where it can be seen that the 10-layer lens has the same drop-off above 40 GHz, supporting the fact that this effect is

solely due to the feed's influence on the aperture efficiency. Note that there are also no ripples present in the 10-layer LL directivity plot.

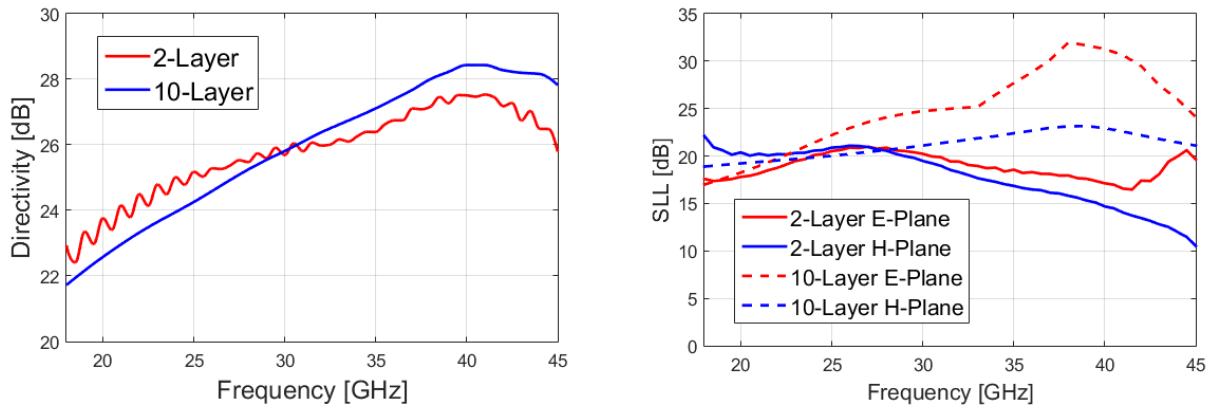

Figure C.3. (a) Directivity and (b) SLL comparison between the 2 and 10-layer LLs as fed by horn 1.

C.2 Reflection Coefficient – Horn 1

Both simulations and measurements of the 2-layer LL reflection coefficient contained ripples, as seen in the 2-layer trace of Figure C.4.

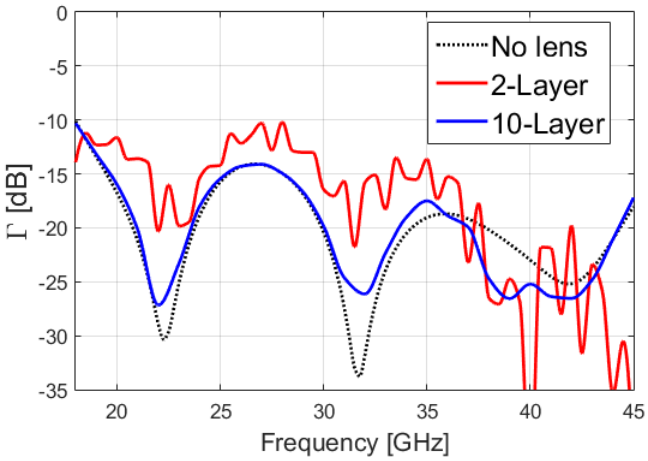

Figure C.4. Reflection coefficient of horn 1 with and without the 2 and 10-layer LLs.

When the 10-layer lens was placed in front of horn 1, the improved matching behavior to free space and between each layer resulted in a reflection coefficient plot very similar to that of the horn by itself. The ripples were also eradicated with the 10-layer LL as was seen in the directivity.